R. & M. No. 3585

R. & M. No. 3585

MINISTRY OF TECHNOLOGY

AERONAUTICAL RESEARCH COUNCIL
REPORTS AND MEMORANDA

The Performance of Some Axi-Symmetric Isentropic Centrebody Intakes Designed for Mach Numbers of 2·48 and 3·27

By E. L. GOLDSMITH and G. V. F. SMITH
Aero/T Dept. RAE Bedford

LONDON: HER MAJESTY'S STATIONERY OFFICE
1969
PRICE £1 16s. 6d. NET

The Performance of Some Axi-Symmetric Isentropic Centrebody Intakes Designed for Mach Numbers of 2·48 and 3·27

By E. L. GOLDSMITH and G. V. F. SMITH
Aero/T Dept. RAE Bedford

Reports and Memoranda No. 3585*
July, 1966

Summary

An experimental investigation of the pressure recovery and drag characteristics of two series of isentropic centrebody intakes (designed for Mach numbers of 2·48 and 3·27 respectively) has been made at zero incidence and over the Mach number range from 2·14 to 3·27. At the design Mach numbers experimental results have been compared with calculated values of drag at full mass flow and estimates of shock pressure recovery. Approximate methods have been devised to predict the variation of full mass flow and drag with Mach number at below design values.

The correlation of experimental pressure recovery with intake geometry for conical centrebody intakes published in an earlier paper has been revised and generalised. It can now be used for all axi-symmetric centrebody designs utilising external compression and internal contraction up to the maximum permissible for 'starting' (without variable geometry).

CONTENTS

* Replaces RAE Technical Report No. TR 66 209 (A.R.C.28 808).

CONTENTS

---

1. *Introduction*

The pressure recovery from the two shock system of a conical centrebody type intake can be improved upon by reshaping the centrebody to produce a multi-shock or ultimately an isentropic external compression before the final normal shock. Such an intake must necessarily have a longer centrebody and deflect the externally compressed air further away from the axis to achieve its greater compression efficiency. Thus compared with the conical centrebody intake its losses other than shock losses may be greater, its liability to flow instability and its proportionate decrease in pressure recovery with angle of incidence will be worse and its external drag may be higher. However at Mach numbers from 3 to 4 the potential gains in pressure recovery are such that if the external drag can be kept at a reasonable level, considerable improvements in performance (as compared with conical centrebody intakes) are possible.

The work reported here has been done to explore this potential with isentropic centrebody intakes designed for $M = 2{\cdot}48$ and 3·27 with the prime object of reducing drag to a minimum consistent with maintaining a pressure recovery which is appreciably higher than that obtainable with a conical centrebody. This recovery will be somewhat lower than the highest that it is possible to attain with this type of intake but nevertheless a higher thrust minus drag may result.

2. *Design of Models*

2.1 *General*

With an isentropic centrebody the characteristics are usually focussed at a point and the cowl has to be positioned with respect to this point in a flow field where large changes in flow direction and Mach number can occur for very small axial or radial changes of the cowl lip position. The problem is further complicated by the presence of the boundary layer on the centrebody which can cause appreciable distortions of the theoretical flow field.

Part of a characteristics network for a typical isentropic centrebody is shown in Fig. 2. High pressure recoveries can be obtained by positioning the cowl at (a) where the mean entry Mach number is approximately 1·24. However because of the large flow deflections, both pre-entry and cowl drags will be high. Placing the cowl further forward where the flow deflection is smaller and the Mach number

higher as at (b) will reduce the drag considerably but will also adversely affect pressure recovery. With a higher mean entry Mach number it is now possible to contract the duct internally to some extent.* For conical centrebody intakes, this has been shown to have a beneficial effect[1] on pressure recovery. Thus by adopting a moderate amount of isentropic compression it may be possible to attain higher thrust minus drag than with either a low drag conical centrebody intake or with a high recovery isentropic centrebody intake.

2.2. *Models designed for* $M = 2{\cdot}48$

The tests performed at this Mach number were of a preliminary nature and were aimed to demonstrate that the ideas enunciated above did lead to some overall advantage.

Cowl shape and lip position relative to the characteristics focus point for an isentropic centrebody design that was tested and reported on in Ref. 2 are shown in Fig. 2. Cowl shapes SD2 and SD6 (which had been combined with 30° conical centrebodies in Refs. 2 and 3) were used with their lips positioned as shown in Fig. 2. In both cases the isentropic centrebody profiles were continued right up to the entry plane so that Mach numbers at the cowl lip and on the centrebody surface were 1·67 and 1·30 respectively for SD2 and 1·93 and 1·47 for SD6. Centrebody and cowl co-ordinates (including the original SD4 design of Ref. 2) are shown in Fig. 3.

2.3. *Models designed for* $M = 3{\cdot}27$

Positions of the cowl lip relative to the focus point that have been chosen as a basis for cowl designs, are shown in Fig. 4. As can be seen eight positions were tried at this Mach number and in addition the centrebody was moved axially (relative to the cowl) for some configurations so altering the cowl lip away from its design position in the compression flow field. Again in each case the isentropic profile has been continued up to the entry plane so that the Mach number across the entry plane varies considerably. Variation of this entry-plane Mach number is indicated in diagrams that are presented with the pressure recovery results in Figs. 14 to 21. Maximum permissible contraction of the duct downstream of the entry plane for 'starting' has been incorporated on all centrebody profiles in their design positions. These contractions are based on the arithmetic mean entry Mach number.

Centrebody and cowl co-ordinates are shown in Figs. 5(a to c).

One centrebody (Isentropic 3·27/E (s)) was made with perforations in the surface near the entry plane (Fig. 5(b)). These holes lead to a central bleed duct which communicates with the free stream *via* hollow connecting struts similar to arrangements tested in Ref. 3.

3. *Apparatus and Test Procedure*

Tests were done in the R.A.E. No. 4 ($5\frac{1}{2}$ in. × $5\frac{1}{2}$ in.) supersonic wind tunnel during 1957. The majority of the tests were ones which combined the measurement of both drag and pressure recovery. Axial force was measured on the complete model by mounting it on a strain gauge balance as shown in Fig. 6. Total pressure of the air flowing through the model was measured at the exit station (Fig. 1) and also the base pressure by means of the pitot-tube rakes shown in Figs. 6 and 7. Flow through the model was varied by changing the exit 'plug' (Fig. 1) at the rear of the model. External drag (i.e. cowl plus pre-entry drag) was obtained (the same procedure as in Ref. 4 where more details are given) by subtracting internal, base, and external skin-friction drags, and the pressure force on the end of the balance sting, from the total axial force measured on the balance. A turbulent flat plate skin-friction coefficient C_f was used for the appropriate free stream Mach number and Reynolds number ($0{\cdot}6 \times 10^6$ at $M = 2{\cdot}14$ to $0{\cdot}35 \times 10^6$ at $M = 3{\cdot}27$) to evaluate external skin-friction drag.

In addition, for the $M = 2{\cdot}48$ tests only, pressure recovery was measured in a separate test at the 'f' station (Fig. 1) using the pitot rakes, support, conical exit throttle etc. shown in Ref. 3. The difference between the recovery at stations 'f' and 'ex' was not thought to be significant when using pressure recovery results in the final correlation presented in Figs. 41 to 50.

---

* Up to the maximum for 'self starting' i.e. contracting the duct until the flow behind a normal shock at the inlet plane accelerates just to sonic velocity.

4. *Discussion of Results*

4.1. $M_d = 2{\cdot}48$

As can be seen from Fig. 2 the length and shape of the pre-entry streamline and the shape of the cowl leads to a high drag for the original design of Ref. 2. An exceptionally high drag was in fact measured because the intake operated with a detached shock at the cowl lip under all conditions of flow through.

The lower drag versions designed with cowls SD2 and SD6 had attached cowl lip shocks and the appreciable reductions in drag together with the accompanying fairly small reductions in pressure recovery compared to the original design are well illustrated in Fig. 8. Also shown in this figure are results quoted from Ref. 5 for two $\theta_c = 30°$ conical centrebody designs using the same two cowl shapes SD2 and SD6. As can be seen gains in pressure recovery of 0·07–0·08 for practically the same drag have been measured for the SD6 cowl shape.

Detail results for pressure recovery and drag variation with mass flow at the three test Mach numbers for the isentropic 2·48-SD6 and SD2 configurations are shown in Figs. 9 to 11.

4.2. $M_d = 3{\cdot}27$

4.2.1. *General.* The $M_d = 2{\cdot}48$ results having proved encouraging it was decided that the main investigation should be at a higher Mach number where it might be much more difficult to obtain both low drag and high recovery. At $M = 3{\cdot}27$ investigations of conical centrebody performance[3] had shown that maximum recoveries of about 0·48 could be combined with low external drag. Hence the primary objective was to demonstrate appreciably higher recoveries than this for the same drag as well as considerably higher pressure recovery with increased drag which nevertheless could be a better compromise on a thrust minus drag basis.

4.2.2. *Boundary-later transition.* Schlieren photographs of one of the centrebodies with and without a transition strip (two thicknesses of Sellotape) are shown in Fig. 12. In Fig. 13 the approximate position of the shock intersection point is shown in relation to the theoretical characteristics focus point. The actual shock intersection may not be a point but a region as analysed in Ref. 6. The point to note however is the large influence of the separation region occurring on the centrebody in the absence of a transition strip, on the position of this shock intersection region. Even the influence of the transition strip itself and the resulting thickened boundary layer leads to a significant displacement of the shock intersection point outside the theoretical characteristics focus point. In view of this result all testing at $M = 3{\cdot}27$ was done with a transition strip on the centrebody.

4.2.3. *Drag and mass flow at* $M_\infty = 3{\cdot}27$. Drag coefficients at full mass flow at $M = 3{\cdot}27$ have been compared with calculated results for each configuration. Pre-entry drag has been calculated by dividing the pre-entry streamline into a number of straight line segments and deriving the pressure coefficients associated with each segment from the characteristics diagram. Cowl drag was computed by two different methods i.e. by quasi-cylinder linear theory and by two dimensional shock-expansion theory. In both cases the pre-entry flow has been taken into account but as Table 1 shows, in the case of linear theory, the difference between allowing for or ignoring the pre-entry flow is small.

TABLE 1

Configuration		$C_{D_{cowl_0}}$	
	Linear theory (no pre-entry flow)	*Linear theory (with pre-entry flow)*	*2 dimensional shock-expansion theory*
Isen. 3·27/O-SD17	0·0250	0·0261	0·0459
O-SD15	0·0164	0·0179	0·0252
E-SD18	0·0305	0·0305	0·0560
E-SD27	0·0404	0·0404	0·0909

For cowls with high initial slopes and small projected area it is probable that two-dimensional shock-expansion theory will give the most realistic results. Maximum mass flows have been estimated from pre-entry streamline shapes derived from the characteristics diagram.

Comparison between measured and calculated drags at full flow are shown in Figs, 14, 15, 16 and 19. As can be seen in Fig. 14 the agreement between calculated and measured values for both drag and maximum mass flow is quite good provided the maximum internal contraction limit is not exceeded. The maximum mass flow tends to be 3 or 4 per cent below the theoretical value even when this limit is not exceeded and as can be seen from the schlieren photographs this is due to additional deflection in the pre-entry flow caused by the boundary layer on the centrebody. This tendency appears to be rapidly exaggerated as more external compression is attempted as in the designs of Figs. 15, 16 and 17 and the boundary layer on the centrebody thickens or 'bridges' part of the profile. These effects are shown quite clearly in the schlieren photographs. Both the low Reynolds number of the tests (approximately $0{\cdot}35 \times 10^6$ based on cowl lip diameter) and the means of fixing transition lead to artificially thick turbulent boundary layers which aggravate this situation.

In the design of Fig. 17 the shock structure limit of Ref. 7 has been exceeded and this is probably the cause of the detached shock at the cowl lip.

4.2.4. *Pressure recovery results at* $M = 3{\cdot}27$. It has been shown with conical centrebody intakes that the effect of contracting the duct internally (up to the maximum allowable for 'starting') on pressure recovery can be quite large particularly if the centrebody surface Mach number at the entry plane is greater than 1·3[1]. Further, for a given contraction ratio the effect of flow turning on the pressure recovery can be characterized by the internal angle of the cowl at the cowl lip (this is discussed further in Section 5). These two parameters have not been the subject of a systematic investigation in the present experiments but the same trends of pressure recovery variation have been observed, as is shown in Fig. 18.

For conical centrebody intakes, provided the conical shock remains outside the cowl lip and the maximum allowable contraction ratio is not exceeded, withdrawal of the centrebody with respect to the cowl (i.e. increase of θ_l) usually results in increased recovery. This is because the increase in mean entry Mach number is generally small and for most normal cowl shapes the internal contraction of the duct is increased. The same trend in results (as θ_l increases) is not generally observed for the isentropic centrebody intakes shown in Figs. 19 and 20. In these cases the beneficial effects of increased internal contraction are being counterbalanced by fairly large increases in mean entry Mach number which lead to increased losses from the final normal shock.

The large decrease in maximum flow and pressure recovery and corresponding increase in drag due to excessive internal contraction is well illustrated in Fig. 20 (b) for Isentropic 3·27/S. Effects of changing cowl shape are shown in Figs. 21 and 22 and do not change pressure recovery appreciably. These changes involve both internal contraction and cowl undersurface slope.

4.2.5. *Summary of pressure recovery and drag at* $M = 3{\cdot}27$. The results show that compared with conical centrebody intake values it is possible to get a substantial increase in pressure recovery (from 0·48 to 0·55) for the same level of external drag, $C_{D_{ext_0}} \simeq 0{\cdot}03$. Efforts to raise this recovery substantially without radically affecting the drag were not so successful however as is illustrated in Fig. 23.

4.2.6. *Effect of boundary-layer suction at* $M = 3{\cdot}27$. For configuration E the effect of sucking boundary layer away through some flush holes in the centrebody surface appears to be small (Fig. 24). As this is a configuration where the cowl lip has been placed at the focus point of the characteristics system and the diffusion has been continued down to $M = 1{\cdot}4$ so that boundary-layer effects on the centrebody should be large, it is probable that the control was not operating effectively and much more work is required in this area.

4.3. *Drag and Pressure Recovery Results at* $M = 2{\cdot}9$, 2·48 and 2·14

4.3.1. *General.* Pressure recovery and drag *versus* mass-flow curves for Mach numbers of 2·9, 2·48 and 2·14 are shown in Figs. 25 to 33 for configurations which gave the most promising results at design Mach number. Summary plots of maximum mass flow, drag and pressure recovery at maximum flow *versus* Mach number are shown in Figs. 34 to 36. The penalty for adopting internal contraction (to

increase pressure recovery at design Mach number) in decreasing maximum flow and correspondingly increasing drag at Mach numbers below design is well illustrated in Figs. 25 and 28 (comparing 3·27/J-SD6A and 3·27/O-SD15). The schlieren photographs (Figs. 25, 28 and 31) show that the shock at the cowl entry only becomes detached at $M = 2{\cdot}14$ for 3·27/J-SD6A whereas it is detached at Mach numbers below 2·90 for 3·27/O-SD15.

It should be noted that 3·27/J-SD6A is the only configuration that has an attached cowl lip shock at both $M = 2{\cdot}9$ and 2·48. As can be seen from Fig. 36 the drag at full flow varies very little between these two Mach numbers. This would seem to indicate that the increased pre-entry drag is being roughly cancelled by a decreased cowl drag due to the changed pre-entry flow in front of the cowl. Below $M = 2{\cdot}48$ the drag rises rapidly due to increasing shock detachment at the cowl lip.

4.3.2. *Estimation of maximum mass flow* $(A_\infty/A_{en})_{max}$ *and external drag at maximum flow* $C_{D_{ext_0}}$. An accurate estimation of $(A_\infty/A_{en})_{max}$ and $C_{D_{ext_0}}$ at Mach numbers below design could be made (assuming no shock detachment at the cowl lip) by constructing a characteristics network for the appropriate Mach number. An approximate method has been devised (*see* Appendix A) however which could be useful for quick estimates. Comparisons of estimated and measured values for $(A_\infty/A_{en})_{max}$ for the range of test Mach numbers are shown in Fig. 37. The agreement (except for 3·27/E for which the external compression is taken down below the 'shock structure' limitation) is quite good.

The drag estimates (*see* Appendix B) shown compared with measured values in Fig. 37 do not agree so well as the maximum flow values. This is probably due to the assumptions concerning the rate of movement of the detached cowl lip shock with spillage (in the cases with excessive internal contraction) which do not agree well with measurements taken from schlieren photographs. As shown in Fig. 39 drag values calculated using measured shock positions in front of the entry plane agree more closely with experimentally determined values.

4.3.3. *Estimation of pressure recovery.* In Fig. 40 the measured pressure recovery is shown compared with the calculated shock recovery (using the approximate construction of Appendix A) for the 3·27/J-SD6A configuration. These curves should (and do) tend to converge at the lower Mach numbers because the internal contraction is getting closer to the maximum allowable for 'starting' (it slightly exceeds it at $M = 2{\cdot}14$) which as has been seen tends to reduce appreciably the losses other than shock losses.

General pressure recovery estimation is dealt with more fully in Section 5.

5. *A General Correlation of Pressure Recovery Results for Centrebody Intakes*

The pressure recovery of centrebody intakes is affected by the shock losses, the mean Mach number and the boundary-layer thickness at the entry plane, the internal contraction ratio, the rate of turning of the airflow at or just downstream of the entry plane, the area distribution and the total wetted area of the subsonic diffuser. In Ref. 1 a general correlation of the majority of published pressure recovery results for conical centrebody intakes was achieved by plotting $P_f/P_\infty \cos \eta_i$ *versus* A_∞/A_t. This takes into account the effect of internal contraction A_t/A_i and flow turning (characterised by the use of η_i the initial angle of the cowl undersurface) but does not take subsonic diffuser variations and Reynolds number or roughness effects into account.

The same method of approach can be taken a stage further so as to be appropriate to multi-shock and isentropic compression surfaces by plotting

$$\frac{\Delta P_f}{P_\infty}\{1 - \sin(\delta_s - \eta_i)\} \textit{ versus } \frac{A_\infty/A_t}{(A_\infty/A_t)_{max}}$$

where

$\dfrac{\Delta P_f}{P_\infty}$ = shock recovery (assuming a final normal shock at $M = M_i$) minus measured pressure recovery i.e. losses other than shock losses

δ_s = inclination to the horizontal of the centrebody surface at the entry plane

η_i = initial angle of the cowl undersurface

$\dfrac{A_\infty}{A_t}$ = actual total contraction ratio

$$= \frac{(A_\infty/A_{en})_{max\,(measured)}}{A_i/A_{en} \times A_t/A_i}$$

$\left(\dfrac{A_\infty}{A_t}\right)_{max}$ = maximum theoretical value for the total contraction ratio

$$= \frac{(A_\infty/A_{en})_{max\,(theoretical)}}{(A_i/A_{en})_{\substack{\text{Theoretical}\\ \text{corresponding to}\\ \text{the design } M_i}} \times (A_t/A_i)_{\substack{\text{max for}\\ \text{'starting'}\\ \text{corresponding to } M_i}}}$$

This provides a correlation expressing the losses other than shock losses in terms of the geometric quantities and flow conditions at the entry plane for a series of values of mean entry plane Mach number M_i.

As with the previous correlation the degree of success achieved by the use of such simple parameters (which obviously have many limitations) is judged simply by the results shown in Figs. 41–50. In general a slightly better collapse of the results is achieved than was obtained for the conical centrebody results of Ref. 1. This is probably due to explicit use of the mean entry Mach number and to the use of a slightly different parameter to express flow turning $(1 - \sin(\delta_s - \eta_i))$ rather than $\cos \eta_i$. Even so this parameter cannot be regarded as wholly satisfactory as of course it is possible to have different rates of flow turning with geometries for which the values of $(A_\infty/A_t)/(A_\infty/A_t)_{max}$ and $\{1 - \sin(\delta_s - \eta_i)\}$ are identical. A study of this situation has in fact been done in Ref. 9 but the results are somewhat inconclusive and cannot be regarded as a general result. However they do indicate that any extra effect not indicated by our parameters is probably fairly small.

As before one obvious limitation of this correlation is the absence of any parameters dealing with the extent and shape of the subsonic diffuser and the Reynolds number of the tests. These effects are probably well illustrated by the differences between the majority of published British and American test results for similar configurations. In general American subsonic diffusers are longer and have lower initial rates of diffusion than British diffusers and the American test Reynolds numbers are higher. Thus the slope of the curves of $(\Delta P_f/P_\infty)\{1 - \sin(\delta_s - \eta_i)\}$ *versus* $(A_\infty/A_t)/(A_\infty/A_t)_{max}$ for similar mean entry Mach numbers are different. The American results for no internal contraction give a value of $(\Delta P/P_\infty)\{1 - \sin(\delta_s - \eta_i)\}$ of approximately 0·033 for all values of M_i (Fig. 45) whereas the British results give a value of about 0·05 for all values of $M_i > 1{\cdot}35$, but this decreases to 0·025 as M_i decreases below 1·35. This is consistent with the generally observed result that when the terminal normal shock separates the compression surface boundary layer, the effect of a slow initial area variation in the subsonic diffuser is beneficial but has the opposite effect (due to higher mean velocity and hence higher skin-friction in the duct) when there is no separation. Thus the generally higher initial rates of diffusion of the British diffuser geometries lead to the results just observed.

Results for isentropic and multi-shock intakes are not numerous but those available fit in well with the single cone shock results. There does not appear to be any consistent effect of the greater boundary-layer thickness at the duct entry plane (due to the larger wetted area and the effect of the larger adverse pressure gradient) compared with the conical centrebody case.

It must be remembered that the results plotted are only applicable to attached or nearly attached shock configurations. Thus they are not applicable for predicting pressure recovery where the configuration has excessive internal contraction or where the external compression exceeds the 'shock structure' limit of Ref. 7.

Example of Application of Correlation Curves

An isentropic centrebody intake designed for $M = 3{\cdot}45$ with the characteristics focussed at the cowl lip at this Mach number. From Ref. 7, M_i corresponding to the 'shock structure' limit = 1·83.

Shock pressure recovery = 0·798.

From Fig. 46 $(\Delta P_f/P_\infty)\{1 - \sin(\delta_s - \eta_i)\} = 0{\cdot}017$ for maximum internal contraction.

Thus the design having minimum drag at the design Mach number will have an internal cowl angle such that the internal cowl lip shock is just attached.

$$\text{i.e. as } M_i = 1{\cdot}83 \text{ and } \delta_s = 36{\cdot}2$$

$$\eta_i = 16{\cdot}5°$$

Thus

$$\frac{\Delta P_f}{P_\infty} = \frac{0{\cdot}017}{1 - \sin(36{\cdot}2 - 16{\cdot}5)} = 0{\cdot}026$$

or

$$\frac{P_f}{P_\infty} = 0{\cdot}772$$

For no internal contraction:

$$\frac{\Delta P_f}{P_\infty}\{1 - \sin(\delta_s - \eta_i)\} = 0{\cdot}048$$

therefore

$$\frac{P_f}{P_\infty} = 0{\cdot}726$$

6. *Conclusions*

Isentropic centrebody intakes can be designed with limited amounts of external compression both at $M = 2{\cdot}48$ and $3{\cdot}27$ so that their external drags are the same as equivalent conical centrebody designs. These designs then have pressure recoveries that are some 0·05–0·08 higher than the conical centrebody intakes and their drag, maximum mass flow and pressure recovery can all be fairly well predicted by simple means.

Isentropic centrebody intakes with rather more external compression than those referred to above give higher drags, lower maximum mass flows and lower pressure recoveries than are predicted theoretically by simple means. The boundary layer on the centrebody would appear to be responsible for these discrepancies and better agreement would probably be obtained if the Reynolds numbers were substantially increased above the present values of approximately $0{\cdot}6 \times 10^6$ ($M = 2{\cdot}14$) to $0{\cdot}35 \times 10^6$ ($M = 3{\cdot}27$).

External compression to entry Mach numbers below the 'shock structure' limit of Ref. 7 results in detached shock waves at the cowl entry and hence to high drags.

Approximate methods for calculating the maximum mass flow and drag at maximum flow at below design Mach number have been suggested that appear to give reasonable agreement with measured values.

A correlation of a large amount of the published information for the pressure recovery of axi-symmetric centrebody intakes has been made. This is similar to the correlation suggested for conical centrebody intakes suggested in Ref. 1 but extends its applicability and appears to give results which could prove useful in the prediction of the performance of any design.

APPENDIX A

Estimation of $(A_\infty/A_{en})_{max}$ *at Mach Numbers below Design*

As shown in Fig. 51 the isentropic centrebody surface has been approximated by an 'equivalent' multi-shock body and the shock wave shapes and streamline patterns behind these shocks have been

determined by an approximate construction. The method of construction used for the curved shocks was suggested in Ref. 10. There remains the determination of the 'equivalent' multi-shock centrebody i.e. δ_1, δ_2, δ_3—etc. The choice of δ_1 is arbitrary but as shown in Table 1A the influence on the final answer in a selected case does not appear to be very great. δ_2, δ_3 etc., are chosen so that the increases in entropy through the shocks emanating from δ_1, δ_2, δ_3 etc. are all approximately equal. In practice the angles δ_2, δ_3 etc. have been decided on the strength of the first segment of the shock wave. This is made somewhat clearer in the following Section which explains the full procedure.

A.1. *Details of the Construction used for Determining* $(A_\infty/A_{en})_{max}$ *(Fig. 51)*

(a) It is assumed that there is a linear variation of Mach number and flow direction with ray angle θ between the values just behind the initial cone shock and the values at the first cone surface.

(b) A constant flow deflection equal to the deflection at the surface (i.e. δ_1, δ_2 etc.) is assumed for each of the subsequent shocks.

(c) δ_1 is chosen arbitrarily and the position of the first kink is determined by the intersection of this line (inclined at $\delta_1 + \theta_c$ to the horizontal and lying tangential to the actual isentropic centrebody profile) with the extension of the initial cone surface.

(d) Cone surface conditions are known and hence for the surface deflection δ_1 the wave angle θ_{ω_1} is known and the shock wave is assumed to be inclined at this angle from the surface until it intersects with the first ray θ_1 where θ_1 is say $\theta_c + 3°$.

(e) At this intersection point the flow is assumed to have a new Mach number and direction (as given by (a) above) and thus the second portion of the shock is constructed having an inclination θ_{ω_2} between the rays θ_1 and θ_2 where $\theta_2 = \theta_1 + 3°$.

(f) The above procedure is repeated until enough of the wave shape has been determined. The straight streamlines (which will slightly converge) are then drawn from the intersection points.

(g) δ_2 is chosen so that the static pressure rise (which is proportional to the entropy gain) is the same for the first element of the third shock as it was for the first element of the second shock. The kink point is again found as the intersection of the line inclined to the horizontal at $(\theta_c + \delta_1 + \delta_2)$ lying tangential to the original isentropic profile with the line inclined at $(\theta_c + \delta_1)$ to the horizontal.

(h) The construction of the third shock is exactly as for the second, the shock being assumed straight between successive streamlines.

(i) Finally the dividing streamline is traced back from the cowl lip to the second shock. The ray defining the intersection of the dividing streamline with this shock is then determined (θ') and the ratio A_∞/A' is obtained from the conical flow data of Ref. 11 where θ' replaces θ_i and A' replaced A_i.

(j) As A' and A_{en} can be found from the diagram, A_∞/A_{en} is determined.

This applies only to intakes whose internal contraction is equal to or less than the maximum for 'starting'. Where this internal contraction limitation is exceeded, choking at the internal throat will impose an additional limit on the maximum mass flow through the intake. The additional calculation for this case is detailed below.

A.2. *Calculation of* $(A_\infty/A_{en})_{max}$ *when the Internal Contraction is Above the Maximum for 'Starting'*

Knowing $(A_\infty/A_{en})_{max}$ from Section 2 above, we can calculate A_i^*/A_i from:

$$\frac{A_i^*}{A_i} = \frac{(A_\infty/A_{en})_{max} \times A_\infty^*/A_\infty}{P_i/P_\infty \times A_i/A_{en}}$$

where 'i' denotes condition at the entry annulus and P_i/P_∞ is assumed to be the total head loss through the initial cone shock only.

From supersonic flow tables the value of M_i the mean inlet Mach number corresponding to A_i^*/A_i can be obtained and hence assuming a normal shock at the entry at this Mach number the new restricted $(A_\infty/A_{en})_{max}$ due to choking at the throat A_t is found from:

$$\left(\frac{A_\infty}{A_{en}}\right)_{max} = \frac{P_i'/P_i \times P_i/P_\infty \times A_t/A_{en}}{A_\infty^*/A_\infty}$$

where P_i'/P_i is the total head loss across a normal shock at $M = M_i$. This does not take into account the fact that the shock will be detached from the entry lip and will occur at a mean Mach number higher than M_i and thus probably the method will tend to overestimate $(A_\infty/A_{en})_{max}$.

TABLE 1A

Configuration	M_∞	δ_1	$\left(\frac{A_\infty}{A_{en}}\right)_{max}$
Isen. 3·27/E	2·90	12	0·7126
		10	0·7337
		8	0·7412
	2·14	10	0·4852
		7	0·4829
		5	0·4876

APPENDIX B

Estimation of $C_{D_{ext_0}}$ at Mach Numbers Below Design

The maximum permissible internal contraction is not exceeded for the whole Mach number range 3·27 to 2·14 for the configuration Isen. 3·27/N-SD24 ($\theta_l = 23·6$) and for the configuration Isen. 3·27/J-SD6A for the Mach number range 3·27 to 2·48. Hence for these configurations the shock at the cowl lip should be attached. In all other instances of estimating the external drag at full mass flow the cowl lip shock will be detached due to excessive internal contraction.

B.1. *Attached Shock at the Cowl Lip*

In this case the drag, as is usual, is the sum of the pre-entry and the cowl drags which, for our approximation to the flow pattern in front of the intake will be (*see* Fig. 52)

$$C_{D_{ext_0}} = \frac{1}{q_\infty A_{max}}\left\{\int_A^B (p - p_\infty)\,dA + (p_1 - p_\infty)(A_C - A_B) + (p_2 - p_\infty)(A_D - A_C) + (p_3 - p_\infty)(A_E - A_D) + (p_4 - p_\infty)(A_F - A_E) + (p_5 - p_\infty)(A_G - A_E)\right\}.$$

As for mass flow, the pre-entry drag for the portion AB of the streamline $\int_A^B \frac{(p - p_\infty)\,dA}{q_\infty A_{max}}$ is obtained from Ref. 11 where θ' replaces θ_l and $C_{D_{pre_0}}$ so derived is based on A_B and hence has to be multiplied by A_B/A_{max}.

Two dimensional flow is assumed over the cowl DG to obtain the pressures p_3, p_4 and p_5.

B.2. *Detached Shock at the Cowl Lip*

The method adopted for dealing with the case when the cowl lip shock is detached due to excessive internal contraction is the same as described in Appendix V of Ref. 5. A linear movement of the shock is assumed with mass flow, from the attached position at full mass flow $(A_\infty/A_{en})_{max}$ calculated assuming that there is no internal contraction to a position at zero mass flow calculated (by the method of Ref. 12) treating the intake as a closed 'bluff' body.

The pre-entry drag (Fig. 53) is now given by

$$C_{D\text{pre}_0} = \frac{1}{q_\infty A_{\max}}\left\{\int_A^B (p - p_\infty)\,dA + (p_1 - p_\infty)(A_C - A_B) + (p_3 - p_\infty)(A_{D_1} - A_C) + \int_{D_1}^D (p - p_\infty)\,dA\right\}$$

$\int_A^B (p - p_\infty)\,dA$ is evaluated in the same manner as suggested above in 1.

The portion $\int_{D_1}^D (p - p_\infty)\,dA$ cannot be evaluated as the static pressure varies in some unknown fashion from the pressure behind the assumed normal shock (at $M = M_3$) to the stagnation pressure at the cowl lip D.

Thus the same method used for conical centrebody intakes is adopted and it is assumed that an underestimate of $C_{D\text{pre}_0}$ given by taking:

$$\int_{D_1}^D (p - p_\infty)\,dA = (p_4 - p_\infty)(A_D - A_{D_1})$$

is counterbalanced by an overestimate of the cowl drag given by calculating this exactly as in the preceding Section (i.e. two dimensional flow is assumed and the effect of the shock detachment on the underside of the cowl lip is ignored), as is known the effect of subsonic pre-spillage is to decrease the cowl drag from the value at full mass flow.

LIST OF SYMBOLS

A	Cross-sectional area
$C_{D_{\text{cowl}}}$	Cowl drag coefficient
$C_{D_{\text{ext}}}$	External drag coefficient
$C_{D_{\text{pre}}}$	Pre-entry drag coefficient
C_f	Skin-friction drag coefficient
M	Mach number
p	Static pressure
P	Total pressure
q	Dynamic pressure $\frac{1}{2}\rho V^2$
r	Radial co-ordinate
x	Axial co-ordinate
$\frac{\Delta P_f}{P_\infty}$	Losses other than shock losses (residual loss)
δ	Change in inclination of centrebody surface
δ_s	Inclination of centrebody surface to horizontal at entry plane
θ	Angle to horizontal of a line passing through tip of the centrebody
η	Angle to horizontal of cowl undersurface
λ	Angle of flow to the horizontal

$()_f$ At the constant area measuring section

$()_i$ At the duct inlet

$()_l$ At the cowl lip

$()_s$ At the centrebody surface

$()_t$ At the duct minimum area section

$()_\omega$ Immediately behind a shock wave

$()_\infty$ In the free stream

$()_{en}$ At the duct entry

$()_{ex}$ At the duct exit

$()_{F.M.F.}$, $()_0$ At full mass flow

$()_{max}$ Maximum value

REFERENCES

No.	*Author(s)*	*Title, etc.*
1	E. L. Goldsmith	The effect of internal contraction initial rate of subsonic diffusion and cowl and centrebody shape on the pressure recovery of a conical centrebody intake at supersonic speeds. A.R.C. R & M 3204. November 1956.
2	E. L. Goldsmith, C. F. Griggs and L. E. Fraenkel	The performance of some centrebody diffuser at supersonic speeds. R.A.E. Tech. Report Aero 2372, (A.R.C. 13540). June 1950.
3	E. L. Goldsmith	The pressure recovery and drag of conical centrebody intakes designed for a Mach number of 3·27. R.A.E. Tech. Note Aero 2513. June 1957 A.R.C. 19929.
4	L. E. Fraenkel	The external drag of some pitot type intakes at supersonic speeds. Part I. R.A.E. Tech. Report Aero 2380, (ARC 13537). June 1950.
5	E. L. Goldsmith and C. F. Griggs	The estimation of shock pressure recovery and external drag of conical centrebody intakes at supersonic speeds. A.R.C. R & M 3035. November 1953.
6	J. F. Connors and R. R. Woollett	Characteristics of flow about axially symmetric isentropic spikes for nose inlets at Mach number 3·85. NACA/TIB/4340.
7	J. F. Connors and R. C. Meyer	Design criteria for axi-symmetric and two dimensional supersonic inlets and exits. NACA Tech. Note 3589.
8	H. R. Hunczak	Pressure recovery and mass flow performance of four annular nose inlets operating in Mach number region of 3·1 and Reynolds number range of approximately $0{\cdot}45 \times 10^6$ to $2{\cdot}20 \times 10^6$. NACA/TIB/4152.
9	J. F. Connors, .. G. A. Wise and J. C. Lovell	Investigation of translating—double-cone axi-symmetric inlets with cowl projected areas 40 and 20 per cent of maximum at Mach numbers from 3·0 to 2·0. NACA/TIL/5524.
10	W. E. Moeckel, J. F. Connors and A. H. Schroeder	Investigation of shock diffusers at Mach number 1·85. II—Projecting double shock cones NACA/TIB/1193.
11	L. E. Fraenkel	Some curves for use in calculations of the performance of conical centrebody intakes at supersonic speeds and at full mass flow. A.R.C. CP 108. December 1951.
12	W. E. Moeckel..	Approximate method for predicting form and location of detached shock waves ahead of plane or axially symmetric bodies. NACA Tech. Note 1921.
13	T. Nussdorfer, .. F. Wilcox and E. Perchonok	Investigation at zero angle of attack of a 16-inch ramjet engine in 8 by 6 ft supersonic wind tunnel. NACA/TIB/3155.

No.	Author(s)	Title, etc.
14	J. F. Connors and R. R. Woollett	Performance characteristics of several types of axially symmetric nose inlets at Mach number 3·85. NACA/TIB/3485.
15	A. Beke and J. L. Allen	Force and pressure recovery characteristics of a conical type nose inlet operating at Mach numbers of 1·6 to 2·0 and at angles of attack to 9°. NACA/TIB/3487.
16	G. C. Gorton	Investigation of translating-spike supersonic inlet as means of mass flow control at Mach numbers of 1·5, 1·8 and 2·0. NACA/TIB/3934.
17	G. C. Gorton	Investigation at supersonic speeds of a translating-spike inlet employing a steep-lip cowl. NACA/TIB/4438.
18	G. C. Gorton and M. Dryer	Comparison of supersonic speeds of translating-spike inlets having blunt and sharp-lip cowls. NACA/TIB/4541.
19	J. F. Connors and R. C. Meyer	Performance characteristics of axi-symmetric two-cone and isentropic nose inlets at Mach number 1·90. NACA/TIB/4804.
20		Bimonthly progress reports on the development of ramjet components. October to November 1950, P.36418.
21		Bimonthly progress reports on the development of ramjet components. April to May 1951, P.36429.

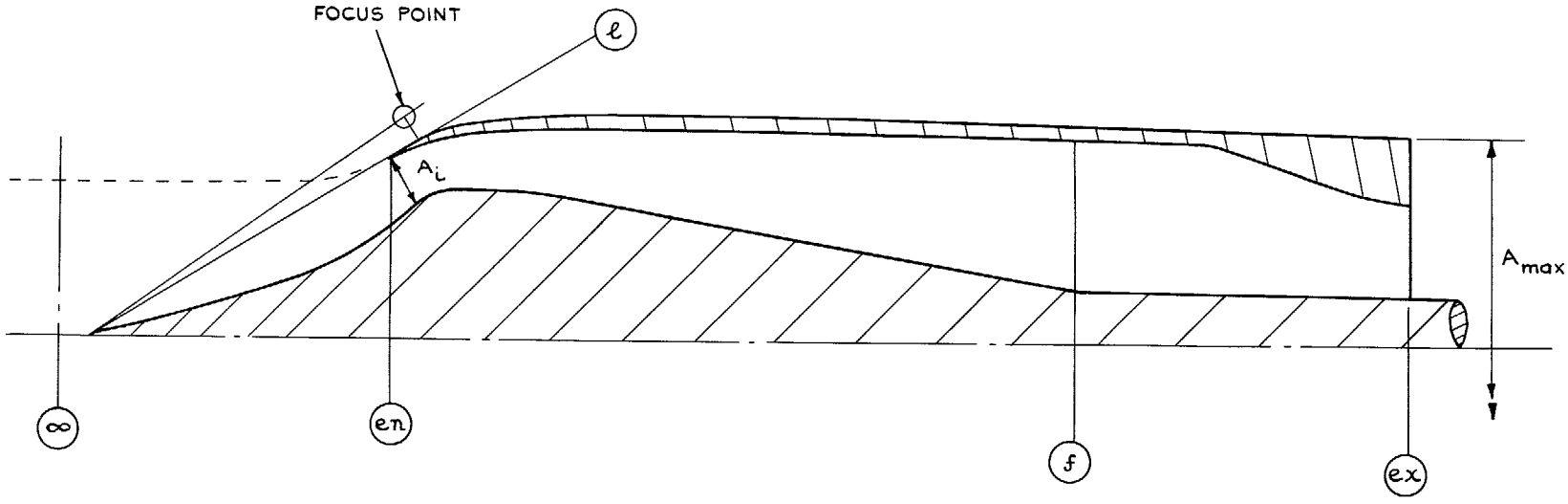

FIG. 1. Suffix notation.

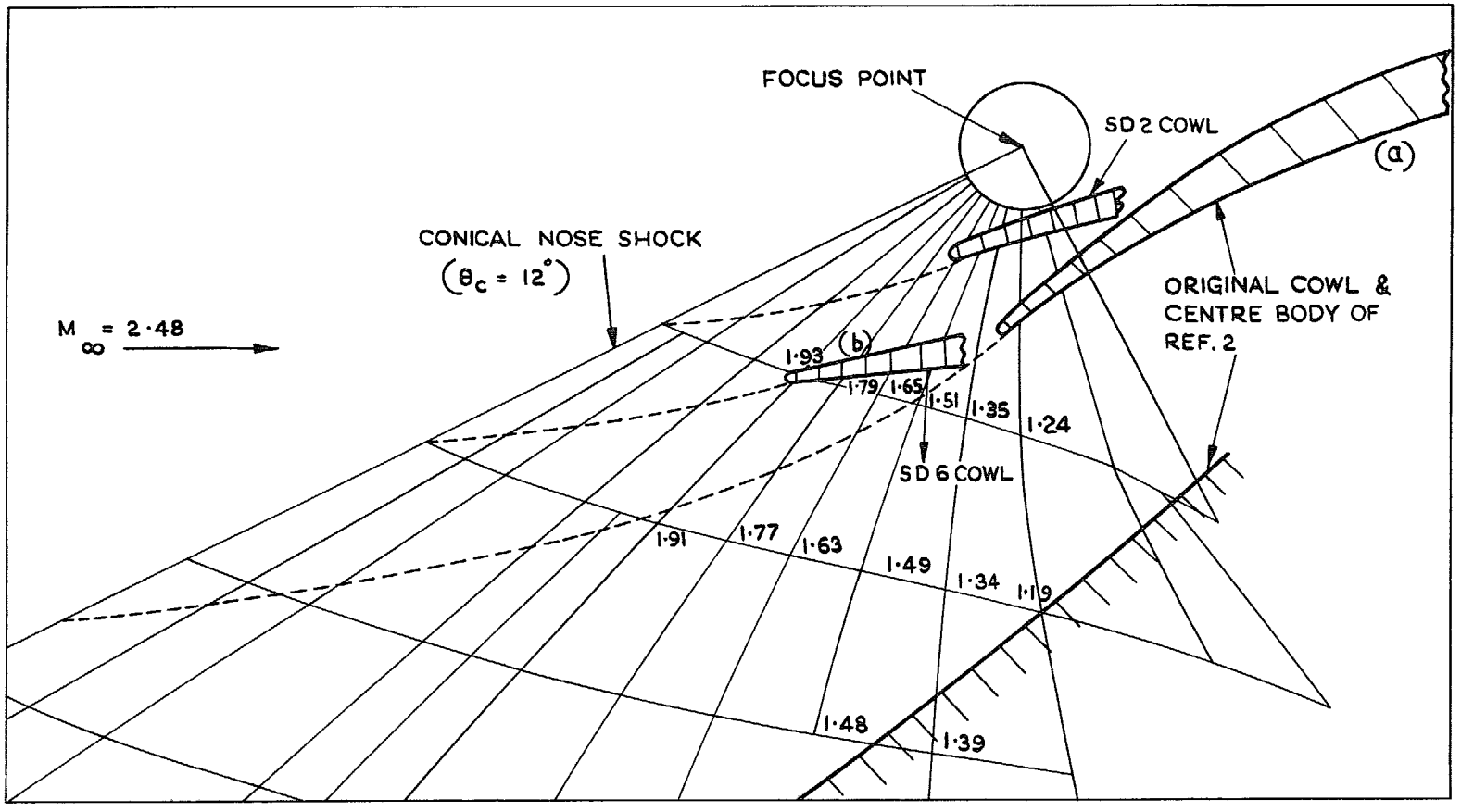

FIG. 2. Characteristics net in the region of the focus point for $M_\infty = 2{\cdot}48$.

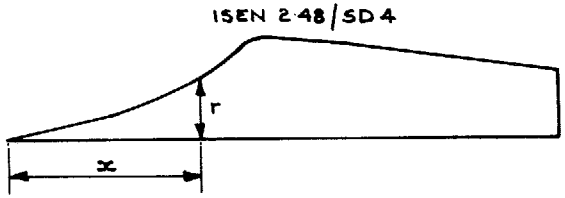

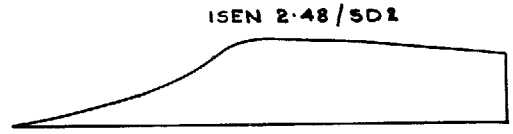

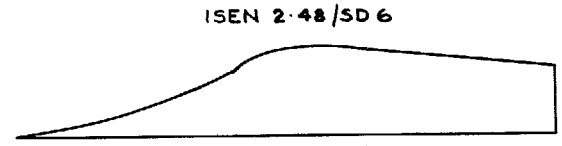

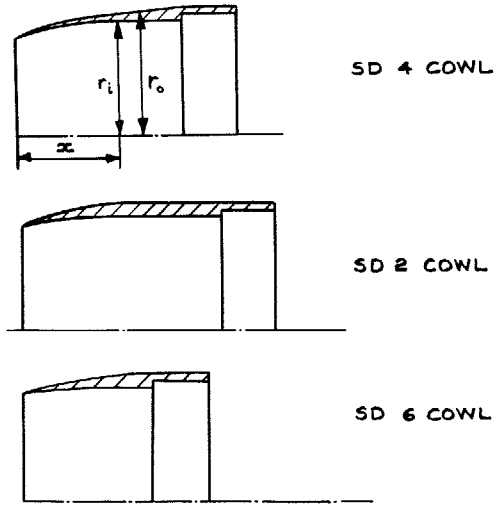

x	RADr	x	RADr	x	RADr	x	RADr	x	RADr	x	RADr
0·0025	0·0025	0·40	0·068	0·90	0·187	1·40	0·356	1·90	0·645	2·40	0·877
0·05	0·004	0·50	0·089	1·00	0·217	1·50	0·401	2·00	0·739	2·50	0·874
0·10	0·009	0·60	0·110	1·10	0·248	1·60	0·449	2·10	0·817	2·60	0·870
0·20	0·026	0·70	0·132	1·26	0·281	1·70	0·501	2·20	0·865	2·70	0·866
0·30	0·047	0·80	0·157	1·30	0·316	1·80	0·561	2·30	0·881		

x	RADr	x	RADr	x	RADr	x	RADr	x	RADr	x	RADr
0	0	0·70	0·145	1·40	0·374	2·10	0·732	2·80	0·744	3·50	0·694
0·10	0·019	0·80	0·171	1·50	0·423	2·20	0·744	2·90	0·738	3·60	0·680
0·20	0·038	0·90	0·201	1·60	0·474	2·30	0·750	3·00	0·732	3·70	0·674
0·30	0·057	1·00	0·229	1·70	0·532	2·40	0·752	3·10	0·726	3·80	0·664
0·40	0·078	1·10	0·260	1·80	0·598	2·50	0·754	3·20	0·720	3·90	0·654
0·50	0·098	1·20	0·294	1·90	0·670	2·60	0·752	3·30	0·710	4·00	0·644
0·60	0·121	1·30	0·333	2·00	0·710	2·70	0·750	3·40	0·702	4·35	0·610

x	RADr	x	RADr	x	RADr	x	RADr	x	RADr	x	RADr
0	0	0·60	0·113	1·20	0·274	1·80	0·506	2·40	0·774	3·00	0·782
0·10	0·016	0·70	0·137	1·30	0·307	1·90	0·559	2·50	0·784	3·10	0·776
0·20	0·035	0·80	0·162	1·40	0·341	2·00	0·617	2·60	0·790	3·20	0·770
0·30	0·053	0·90	0·186	1·50	0·377	2·10	0·682	2·70	0·790	3·40	0·748
0·40	0·071	1·00	0·213	1·60	0·416	2·20	0·730	2·80	0·790	3·60	0·728
0·50	0·092	1·10	0·241	1·70	0·458	2·30	0·760	2·90	7·784	4·75	0·610

x	r_i	r_o	x	r_i	r_o	x	r_i	r_o
0	0·844	0·855	0·25	0·976	1·015	0·50	1·000	1·063
0·05	0·880	0·896	0·30	0·989	1·028	STR TAPER		
0·10	0·910	0·937	0·35	0·996	1·040	1·437	1·000	1·125
0·15	0·936	0·970	0·40	0·998	1·049			
0·20	0·958	0·995	0·45	0·999	1·056			

x	r_i	r_o	x	r_i	r_o	x	r_i	r_o
0	0·9000	0·9100	0·5	0·9965	1·0640	1·000	0·9999	1·1225
0·1	0·9265	0·9465	0·6	0·9999	1·0875	1·100	0·9999	1·1240
0·2	0·9530	0·9815	0·7	0·9999	1·1010			
0·3	0·9730	1·0115	0·8	0·9999	1·1130			
0·4	0·9880	1·0400	0·9	0·9999	1·1205			

x	r_i	r_o	x	r_i	r_o	x	r_i	r_o
0	0·9525	0·9675	0·5	0·9975	1·0560	1·000	0·9999	1·116
0·1	0·9600	0·9795	0·6	0·9999	1·0725	1·10	0·9999	1·1215
0·2	0·975	1·0010	0·7	0·9999	1·0855	1·20	0·9999	1·125
0·3	0·986	1·0205	0·8	0·9999	1·098	1·30	0·9999	1·125
0·4	0·995	1·0400	0·9	0·9999	1·108			

FIG. 3. Cowl and centrebody dimensions.

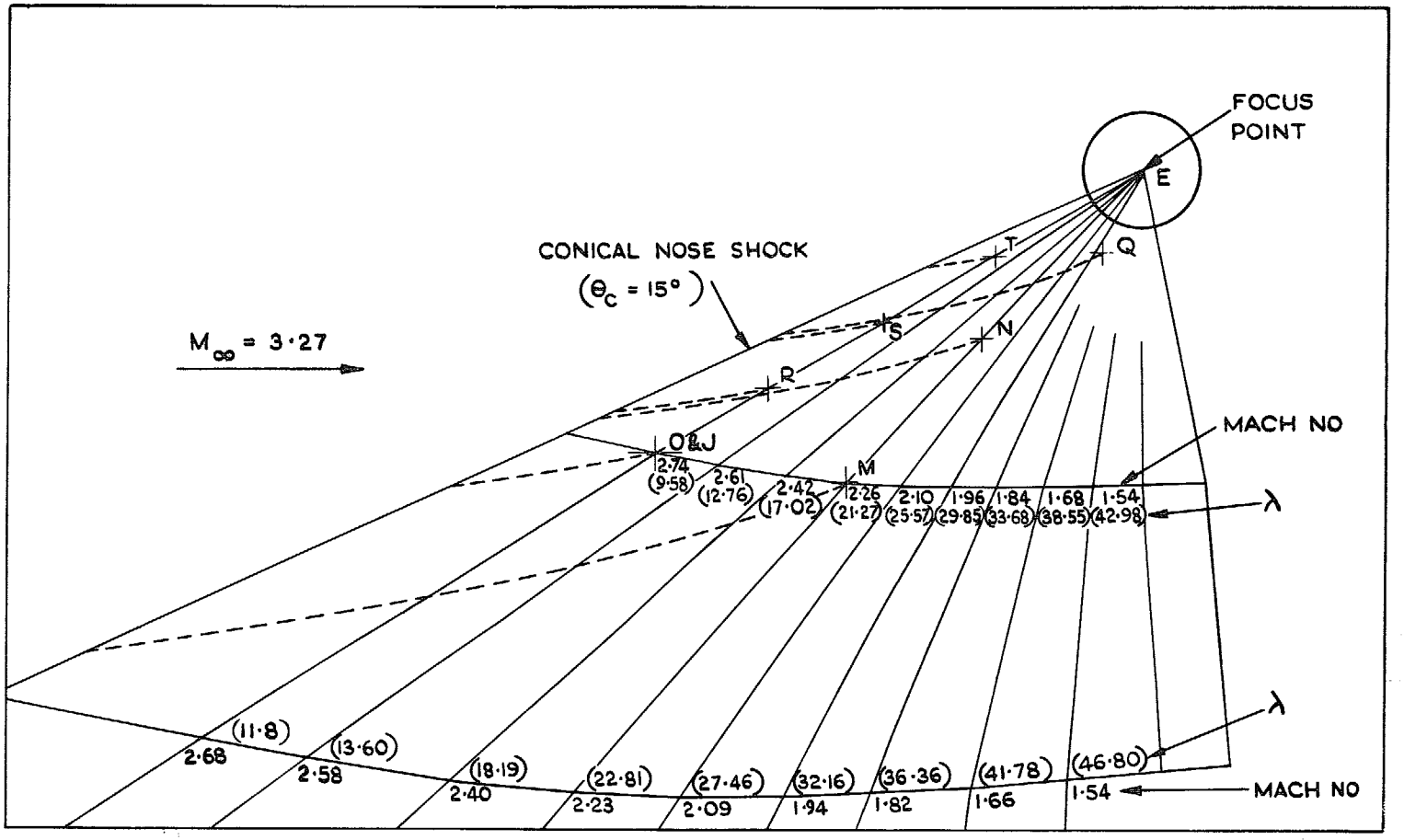

FIG. 4. Characteristics net in the region of the focus point for $M_\infty = 3{\cdot}27$.

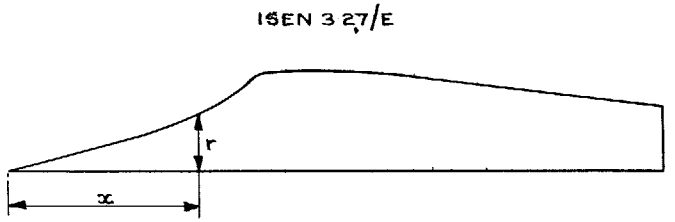

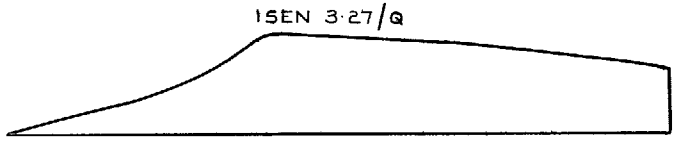

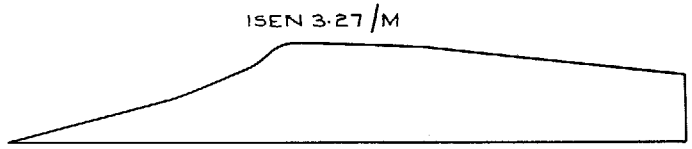

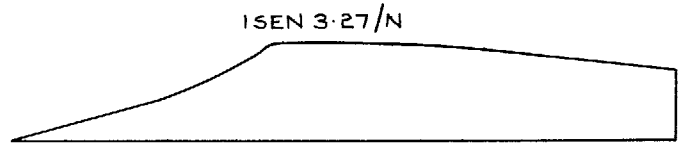

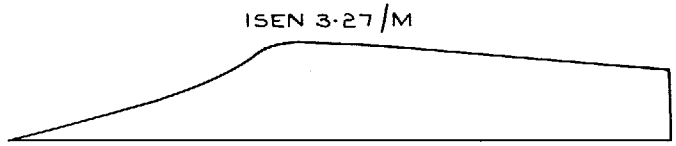

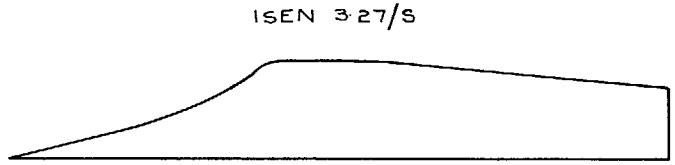

x	RADr	x	RADr	x	RADr	x	RADr
0	0	2·000	0·684	2·400	0·877	3·300	0·862
15° TAPER TO		2·100	0·770	2·500	0·878	3·500	0·850
1·000	0·269	2·150	0·823	2·800	0·878	3·750	0·830
1·250	0·341	2·200	0·852	2·900	0·8765	4·000	0·806
1·500	0·427	2·250	0·863	3·000	0·8735	STR TAPER TO	
1·750	0·532	2·300	0·872	3·100	0·871	5·735	0·613

x	RADr	x	RADr	x	RADr	x	RADr	x	RADr
0	0	1·5316	0·4327	2·0173	0·6690	2·3000	0·8790	3·000	0·8880
15° TAPER TO		1·6514	0·4797	2·0731	0·7084	2·3500	0·8880	3·250	0·8760
1·0721	0·2866	1·7378	0·5175	2·1273	0·7527	2·4000	0·8920	3·500	0·8600
1·1990	0·3222	1·8138	0·5525	2·1500	0·7740	2·5000	0·8940	4·000	0·8130
1·3035	0·3550	1·8746	0·5836	2·2000	0·8250	2·6000	0·8940	STR TAPER TO	
1·3998	0·3862	2·9293	0·6143	2·2500	0·8670	2·7500	0·8940	2·792	0·6150

x	RADr	x	RADr	x	RADr	x	RADr	x	RADr
0	0	1·8349	0·5330	2·3637	0·8363	2·6500	0·8780	3·7500	0·8300
15° TAPER TO		1·9310	0·5750	2·4000	0·8520	2·8000	0·8780	4·0000	0·8060
1·1912	0·3185	2·0155	0·6139	2·4250	0·8620	2·9000	0·8765	STR TAPER TO	
1·3323	0·3580	2·0829	0·6485	2·4500	0·8690	3·0000	0·8735	5·916	0·6140
1·4484	0·3945	2·1437	0·6826	2·4750	0·8730	3·1000	0·8710		
1·5554	0·4291	2·2416	0·7433	2·5000	0·8770	3·3000	0·8620		
1·7018	0·4808	2·3036	0·7871	2·6000	0·8780	3·5000	0·8500		

x	RADr	x	RADr	x	RADr	x	RADr	x	RADr
0	0	1·7136	0·4978	2·2000	0·7750	3·0000	0·8550	3·7000	0·8320
15° TAPER TO		1·8033	0·5369	2·2500	0·8090	3·1000	0·8540	3·8000	0·8250
1·1125	0·2974	1·8822	0·5733	2·3000	0·8330	3·2000	0·8520	3·9000	0·8060
1·2442	0·3343	1·9452	0·6056	2·3500	0·8470	3·3000	0·8500	STR. TAPER TO	
1·3526	0·3684	2·0019	0·6374	2·4000	0·8550	3·4000	0·8470	5·8220	0·6130
1·4525	0·4007	2·0933	0·6942	2·4500	0·8560	3·5000	0·8420		
1·5893	0·4490	2·1512	0·7350	2·5000	0·8560	3·6000	0·8370		

x	RADr	x	RADr	x	RADr	x	RADr	x	RADr
0	0	1·630	0·460	2·146	0·712	2·600	0·851	STR TAPER TO	
15° TAPER TO		1·757	0·510	2·200	0·749	2·900	0·851	5·782	0·612
1·1121	0·2980	1·849	0·551	2·250	0·789	3·200	0·846		
1·276	3·428	1·930	0·588	2·300	0·817	3·300	0·838		
1·387	0·3777	1·995	0·621	2·400	0·843	3·500	0·825		
1·489	0·4109	2·053	0·654	2·500	0·850	3·600	0·815		

x	RADr	x	RADr	x	RADr	x	RADr	x	RADr
0	0	1·583	0·447	2·086	0·691	2·500	0·873	STR TAPER TO	
15° TAPER TO		1·707	0·496	2·100	0·701	2·600	0·873	5·771	0·610
1·108	0·296	1·796	0·535	2·200	0·781	2·700	0·871		
1·239	0·333	1·875	0·571	2·250	0·827	2·900	0·866		
1·347	0·367	1·937	0·603	2·300	0·852	3·100	0·855		
1·447	0·399	1·994	0·635	2·400	0·870	3·000	0·825		

FIG. 5a. Centrebody dimensions.

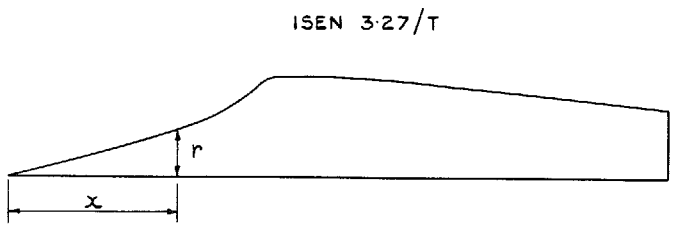

x	RAD T	x	RAD T	x	RAD T	x	RAD T	x	RAD T
0	0	1·537	0·434	2·000	0·653	2·500	0·892	3·750	0·817
15° TAPER TO		1·657	0·481	2·100	0·725	2·700	0·892	STR TAPER TO	
1·076	0·288	1·744	0·519	2·200	0·825	2·800	0·889	5·755	0·612
1·203	0·323	1·820	0·554	2·250	0·868	3·000	0·885		
1·308	0·356	1·881	0·586	2·300	0·883	3·250	0·864		
1·405	0·388	1·936	0·617	2·400	0·890	3·500	0·843		

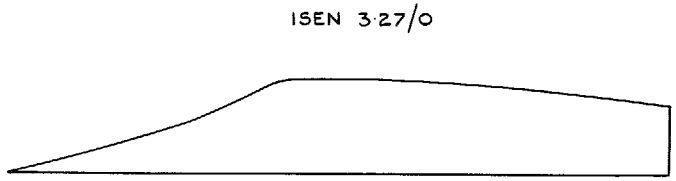

x	RAD T	x	RAD T	x	RAD T	x	RAD T	x	RAD T
0	0	2·000	0·611	2·600	0·831	4·000	0·790	5·600	0·635
15° TAPER TO		2·100	0·664	3·100	0·831	4·400	0·756	5·801	0·613
1·000	0·269	2·200	0·725	3·200	0·828	4·800	0·718		
1·250	0·336	2·300	0·774	3·400	0·823	5·000	0·698		
1·500	0·411	2·400	0·811	3·600	0·815	5·200	0·678		
1·750	0·500	2·500	0·828	3·800	0·803	5·400	0·657		

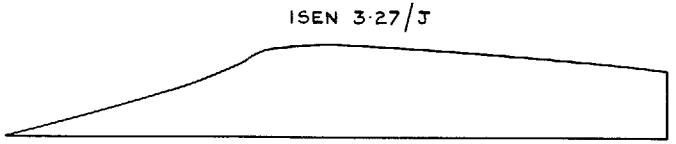

x	RAD T	x	RAD T	x	RAD T	x	RAD T	x	RAD T
0	0	2·000	0·611	2·600	0·801	3·400	0·795	5·801	0·615
15° TAPER TO		2·100	0·664	2·700	0·802	3·600	0·789		
1·000	0·269	2·200	0·725	2·800	0·803	4·000	0·768		
1·250	0·336	2·300	0·773	3·000	0·803	4·500	0·733		
1·500	0·411	2·400	0·791	3·100	0·802	5·000	0·692		
1·750	0·500	2·500	0·799	3·200	0·800	5·500	0·645		

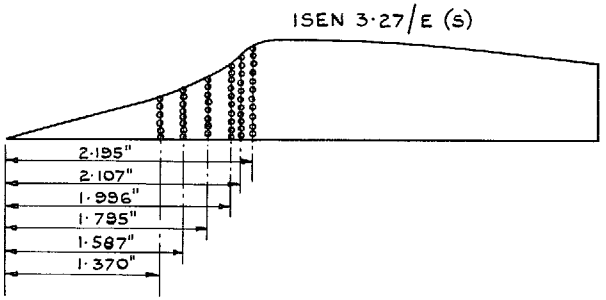

x	RAD T	x	RAD T	x	RAD T	x	RAD T	x	RAD T
0	0	2·000	0·684	2·400	0·877	3·300	0·862		
15° TAPER TO		2·100	0·770	2·500	0·877	3·500	0·850		
1·000	0·269	2·150	0·823	2·800	0·878	3·750	0·830		
1·250	0·341	2·200	0·852	2·900	0·8765	4·000	0·806		
1·500	0·427	2·250	0·863	3·000	0·8735	STR	TAPER		
1·750	0·532	2·300	0·872	3·100	0·8710	5·118	0·686		

FIG. 5b. Centrebody dimensions.

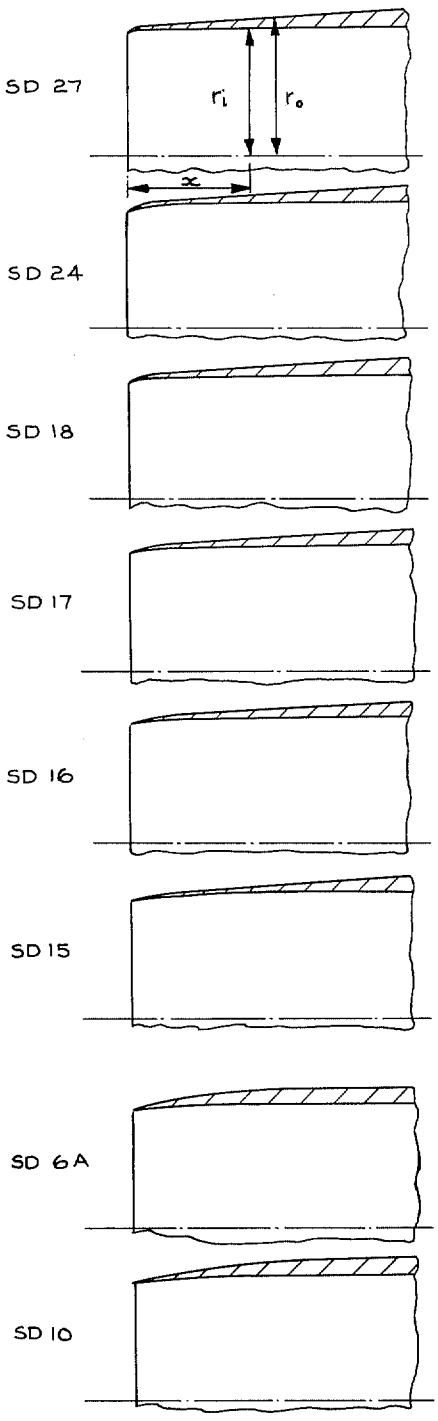

x	RADri	RADro
0	0·9525	0·9575
0·04	0·974	ST TAPER
0·09	0·990	1·0137
0·15	1·000	ST TAPER
2·25	1·000	1·125

x	RADri	RADro	x	RADri	RADro
0	0·940	0·945	0·20	0·998	ST TAPER
0·10	0·976	ST TAPER	0·30	0·999	
0·15		1·011	0·40	1·000	
			2·25	1·000	1·125

x	RADri	RADro	x	RADri	RADro
0	0·9525	0·9575	0·30	0·999	
0·1	0·9830	ST TAPER	0·40	1·000	
0·19		1·0139	1·75	1·000	
0·20	0·9980	ST TAPER	2·25		1·125

x	RADri	RADro	x	RADri	RADro
0	0·9525	0·9575	0·30	0·997	ST TAPER
0·1	0·9760	ST TAPER	0·40	1·000	
0·2	0·989		1·75	1·000	
0·23		1·0106	2·25		1·125

x	RADri	RADro	x	RADri	RADro
0	0·9525	0·9575	0·40	0·997	ST TAPER
0·10	0·976	ST TAPER	0·60	1·000	
0·20	0·989		1·75	1·000	
0·30		1·0105	2·25		1·125

x	RADri	RADro	x	RADri	RADro
0	0·9525	0·9575	0·6	0·993	
0·1	0·966	ST TAPER	0·7	0·995	
0·2	0·977		0·8	0·998	
0·3	0·983		0·9	0·999	
0·4	0·988	1·0049	1·0	1·000	
0·5	0·992	ST TAPER	1·75	1·000	
			2·25		1·125

x	RADri	RADro	x	RADri	RADro
0	0·95	0·9575	0·7	1·00	1·0855
0·1	0·96	0·9795	0·8	0·999	1·098
0·2	0·97	1·001	0·9	0·998	1·108
0·3	0·98	1·0205	1·0	0·998	1·116
0·4	0·989	1·040	1·1		1·1215
0·5	0·996	1·056	1·2		1·125
0·6	1·00	1·0725	1·3		1·125

x	RADri	RADro	x	RADri	RADro
0	0·952	0·958	0·6	0·993	1·038
0·1	0·958	0·972	0·7	0·999	1·053
0·2	0·966	0·985	0·9	1·001	1·076
0·3	0·972	0·998	1·1	1·001	1·094
0·4	0·979	1·010	1·5	1·001	1·119
0·5	0·986	1·027	1·7	1·001	1·125

FIG. 5c. Cowl dimensions.

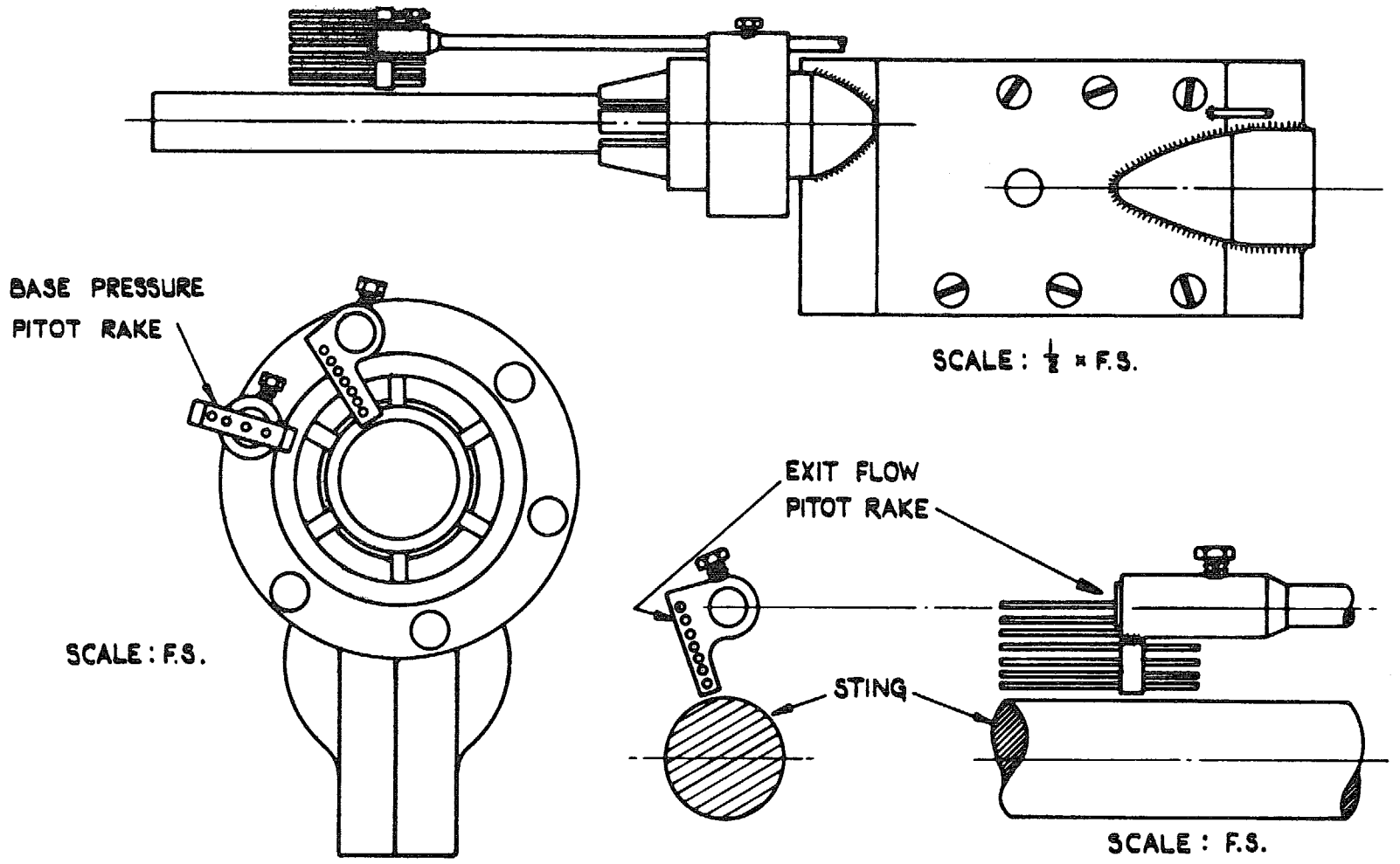

FIG. 6. Strain gauge drag balance.

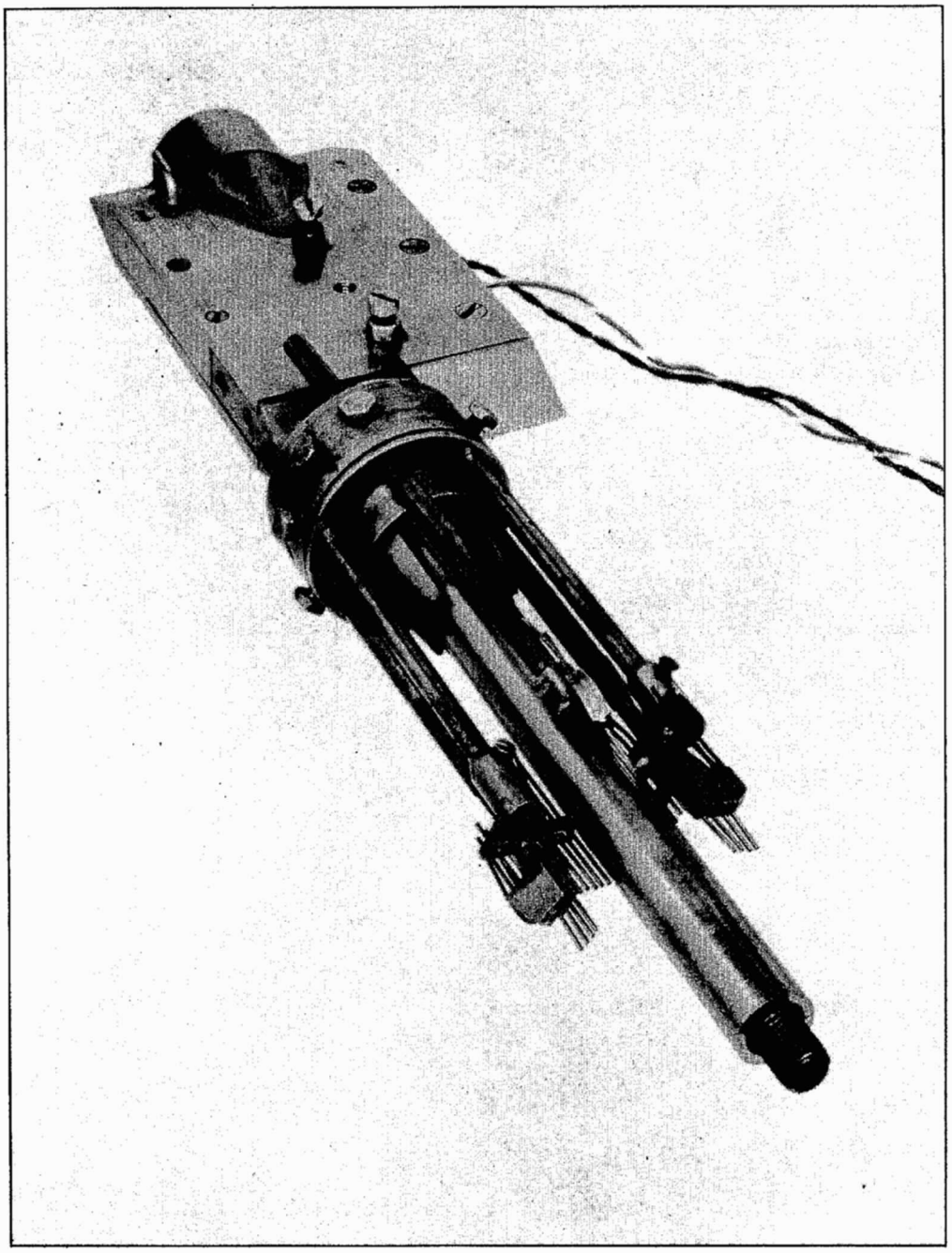

FIG. 7. Strain gauge drag balance with exit flow and base pressure pitot tube rakes.

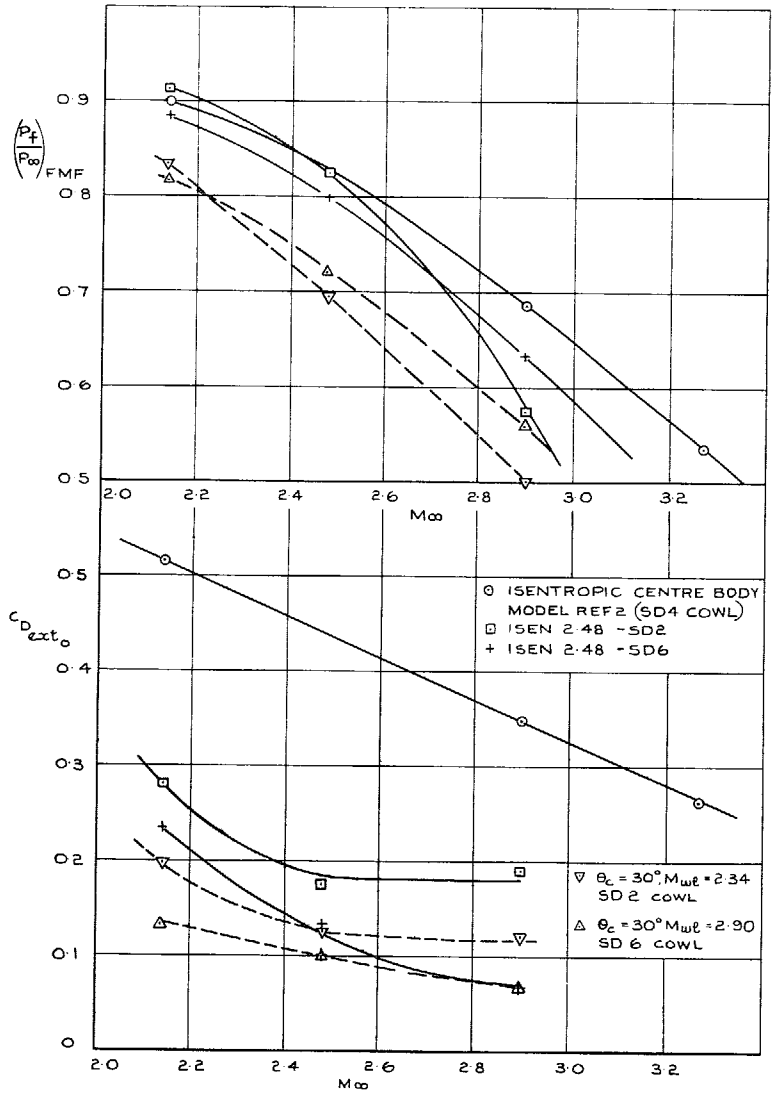

FIG. 8. Drag and pressure recovery at full mass flow for isentropic and conical centrebody (Ref. 5) configurations.

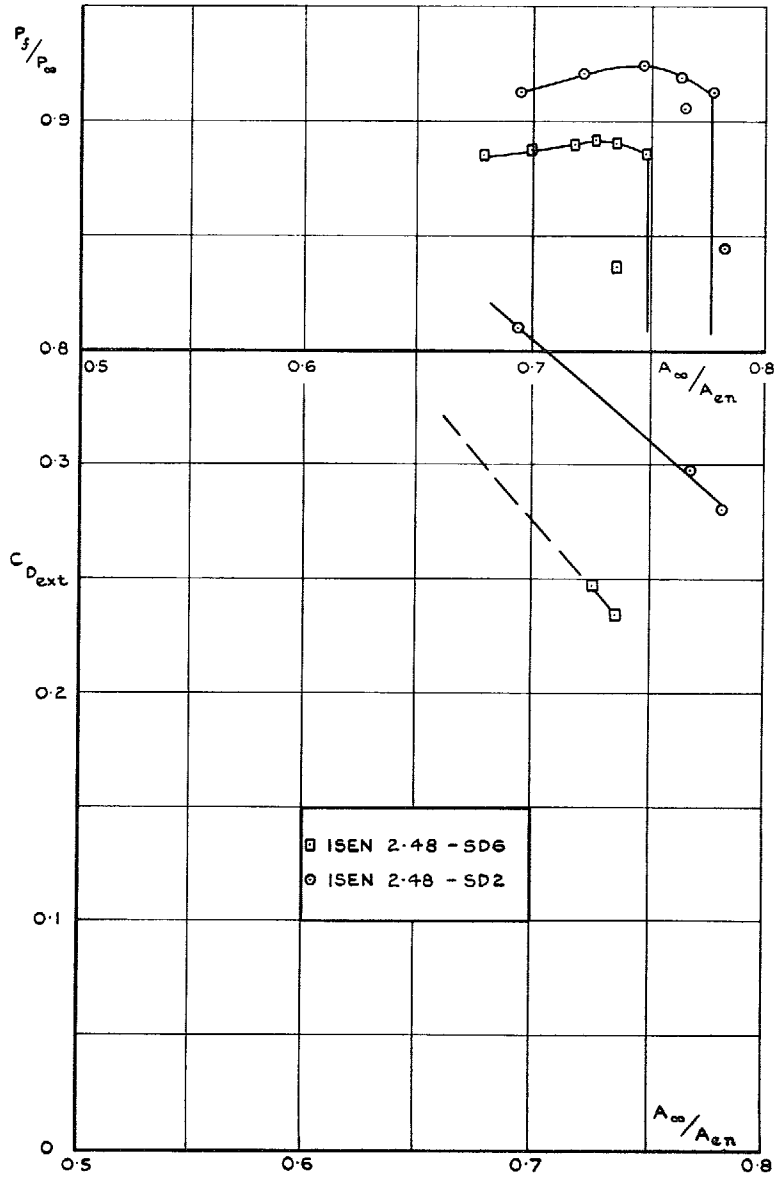

FIG. 9. Pressure recovery and drag of isentropic centrebody intakes ($M_d = 2·48$) at $M_\infty = 2·14$.

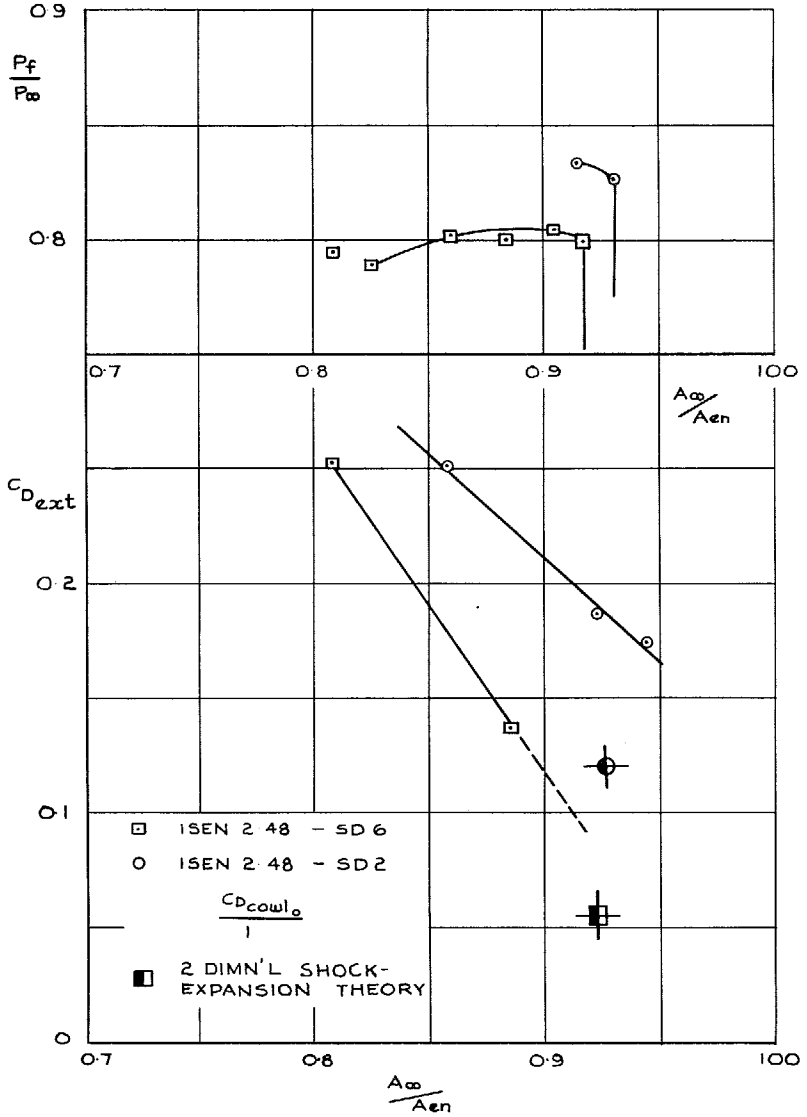

FIG. 10. Pressure recovery and drag of isentropic centrebody intakes ($M_d = 2{\cdot}48$) at $M_\infty = 2{\cdot}48$.

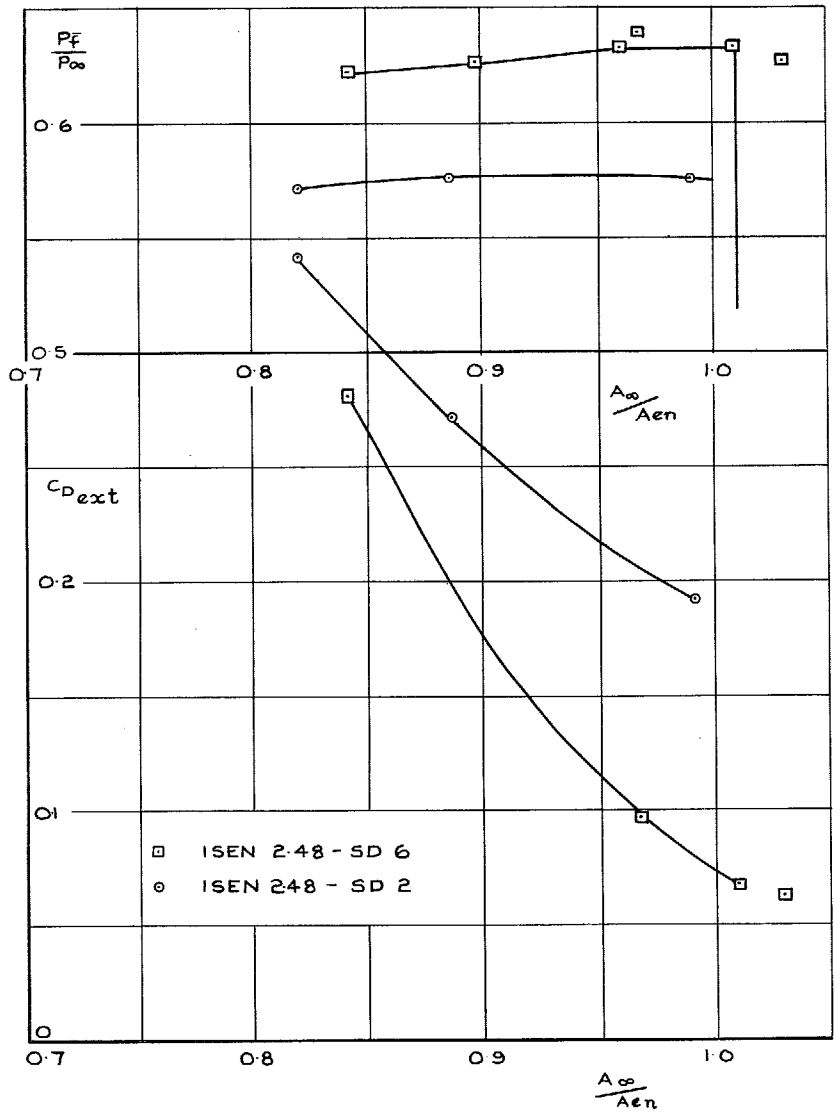

FIG. 11. Pressure recovery and drag of isentropic centrebody intakes ($M_d = 2{\cdot}48$) at $M_\infty = 2{\cdot}90$.

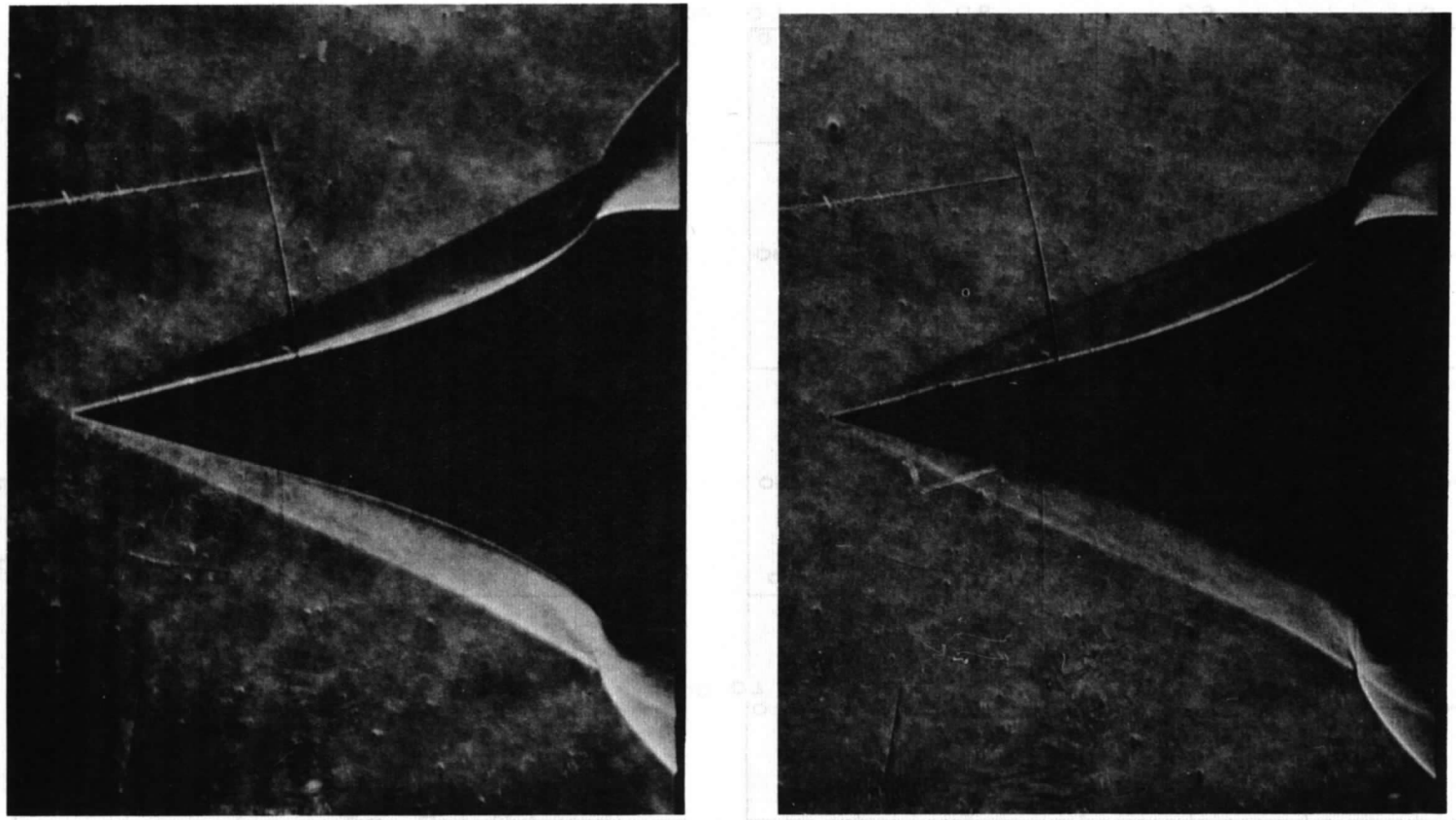

FIG. 12. Boundary layer development on an isentropic centrebody with and without a transition strip.

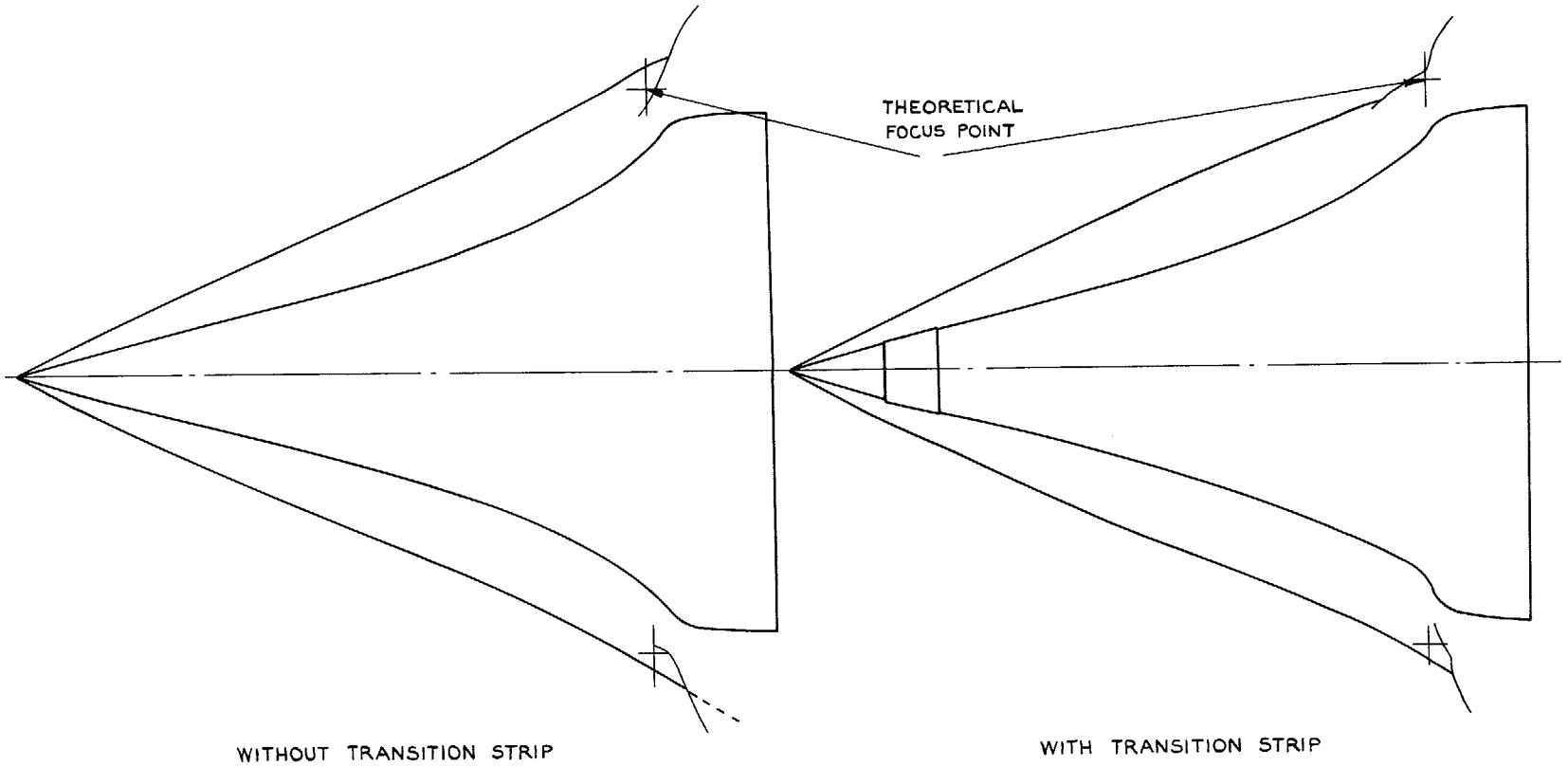

FIG. 13. Comparison of theoretical and actual focus point positions.

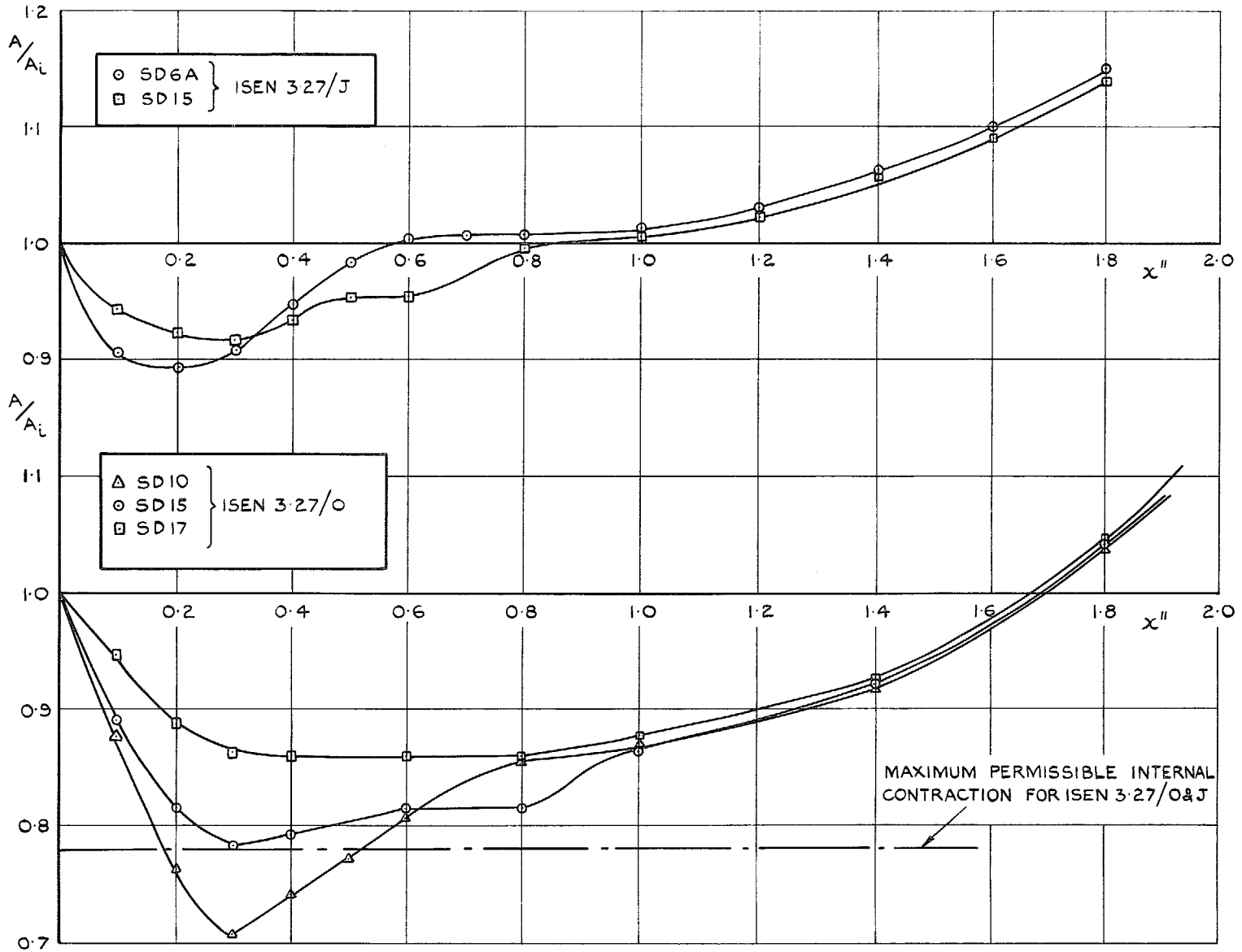

FIG. 14a. Duct internal area distributions.

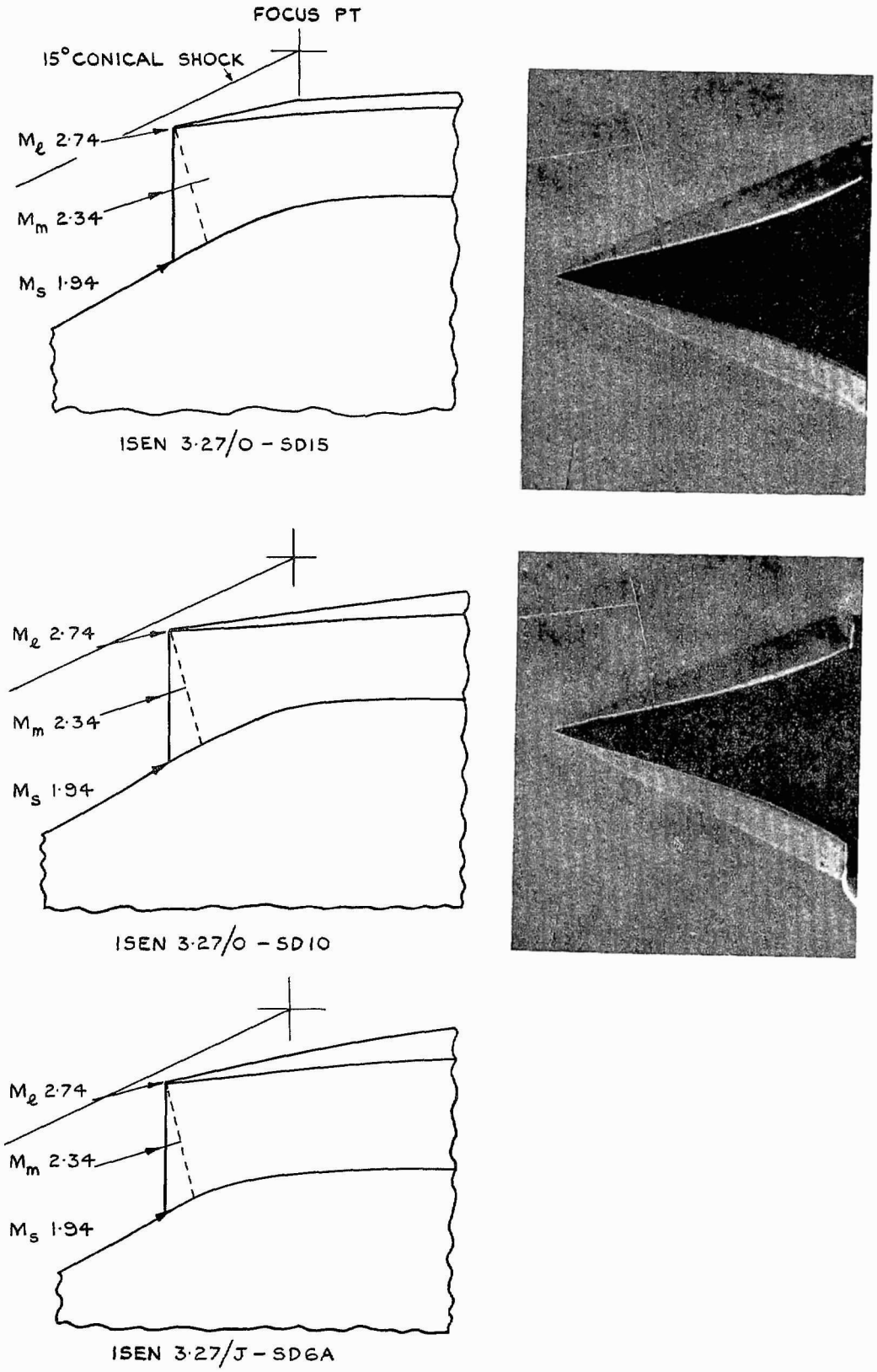

FIG. 14b. Theoretical and actual flow configurations.

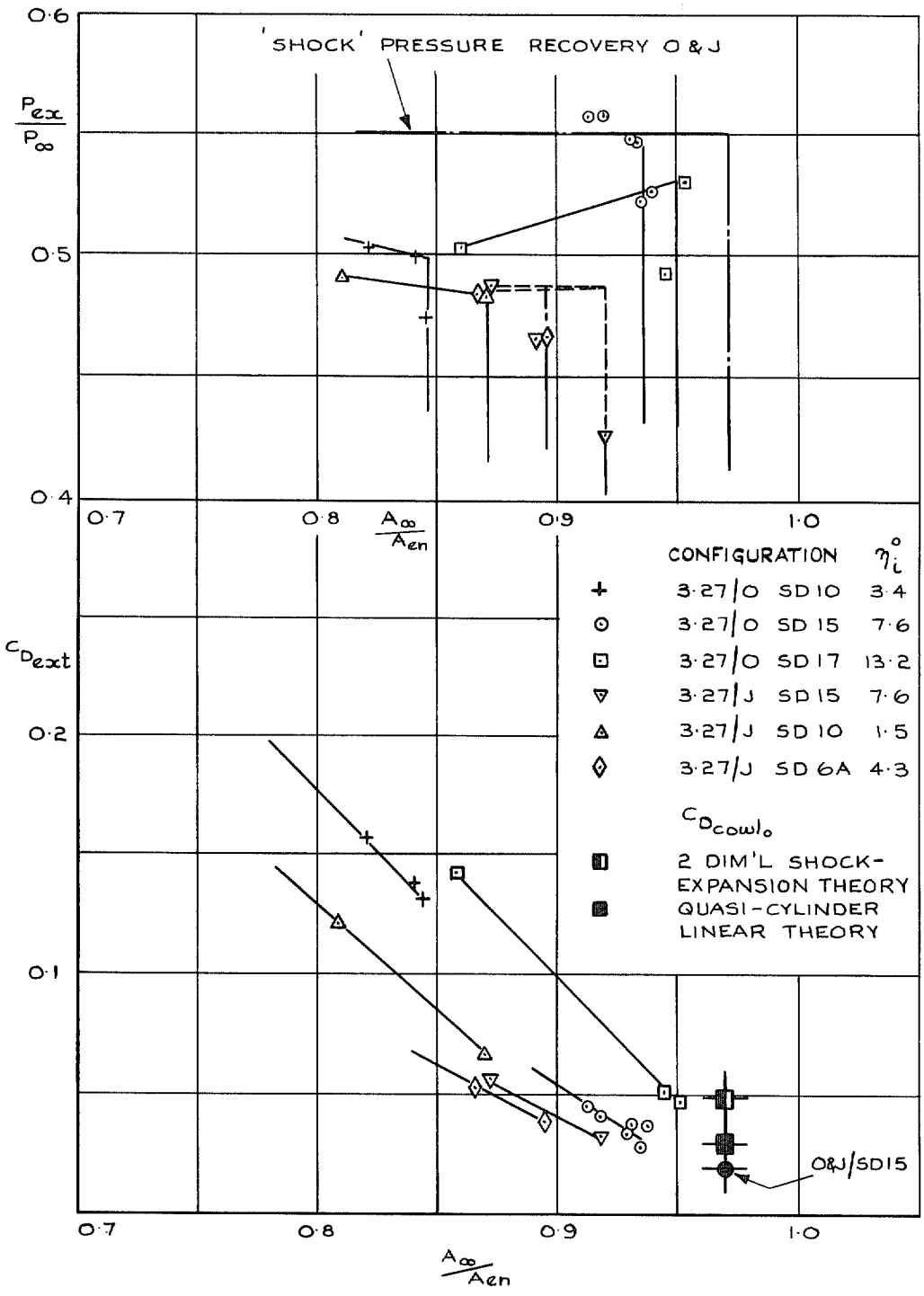

FIG. 14c. Drag and pressure recovery of Isen 3·27/O and J at $M_\infty = 3{\cdot}27$.

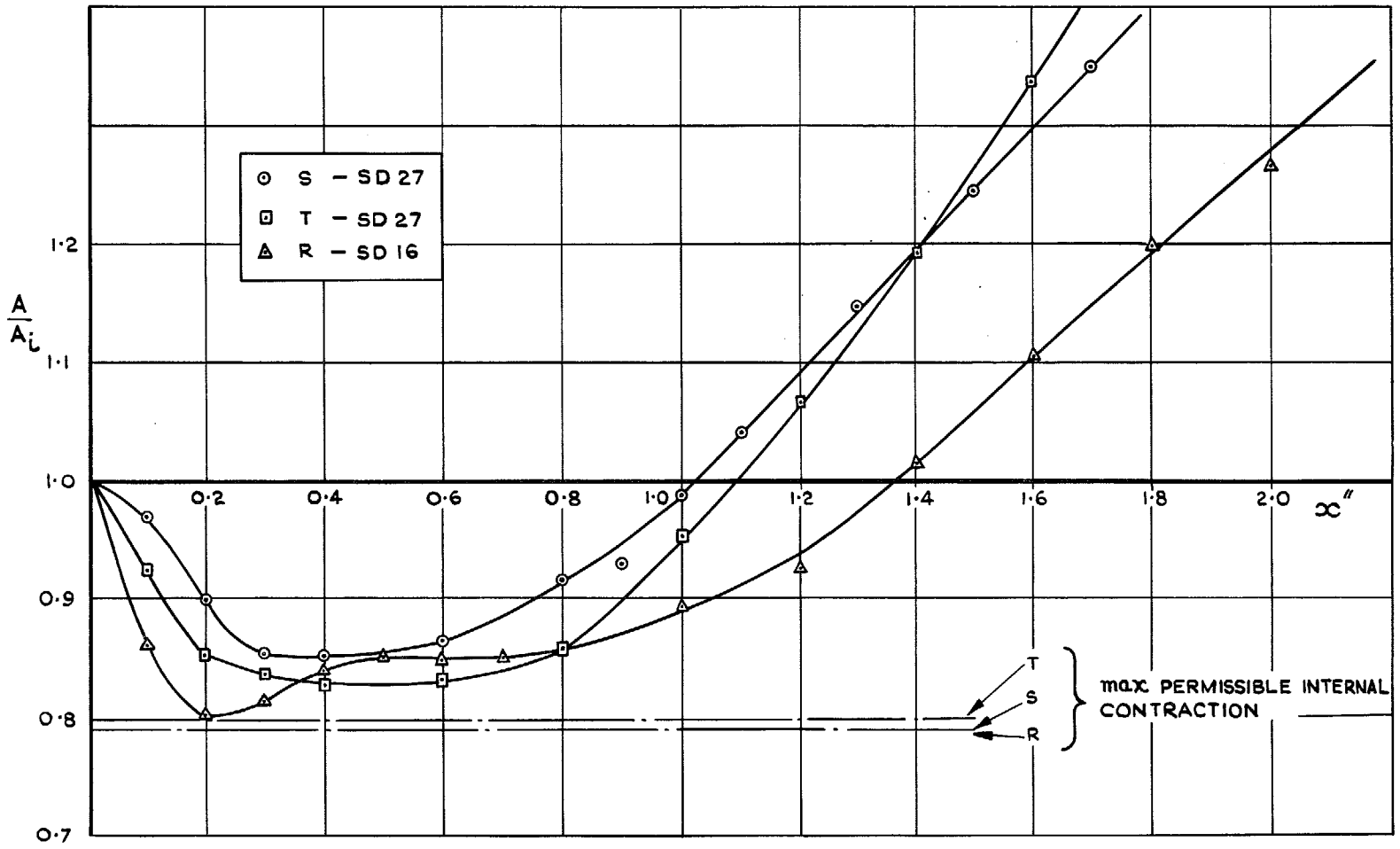

FIG. 15a. Duct internal area distribution.

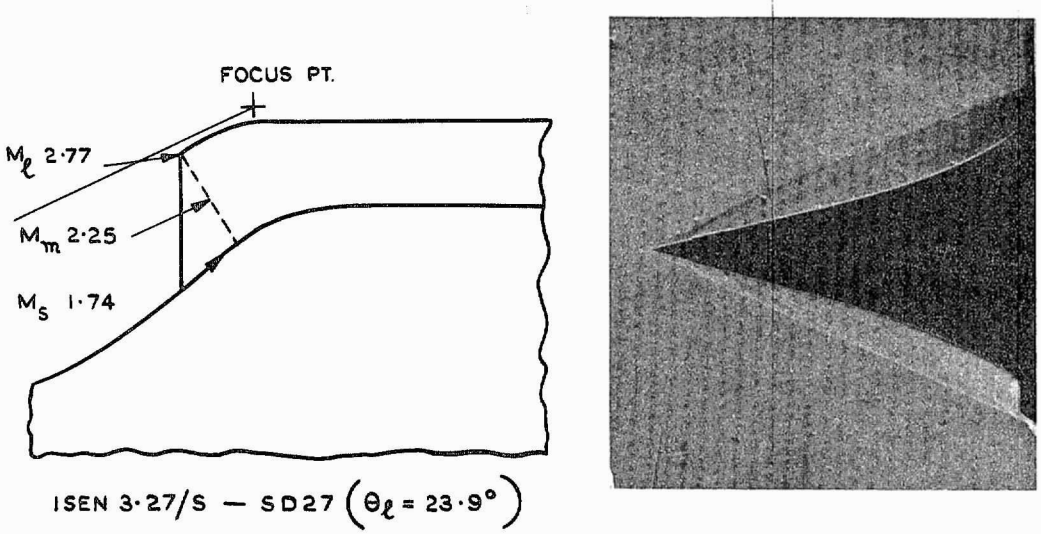

ISEN 3·27/S — SD27 $(\theta_\ell = 23{\cdot}9°)$

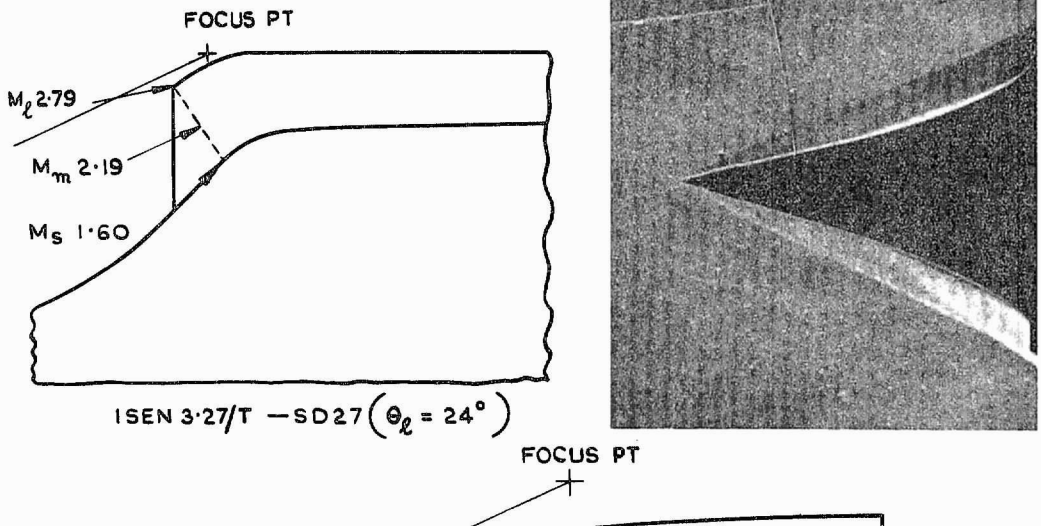

ISEN 3·27/T — SD27 $(\theta_\ell = 24°)$

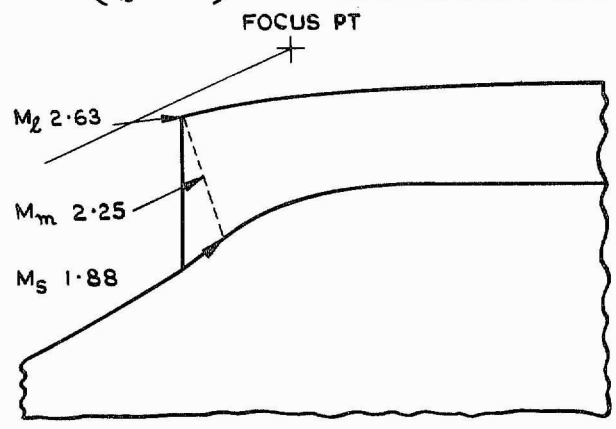

ISEN 3·27/R — SD 16 $(\theta_\ell = 23{\cdot}7°)$

FIG. 15b. Theoretical and actual flow configurations.

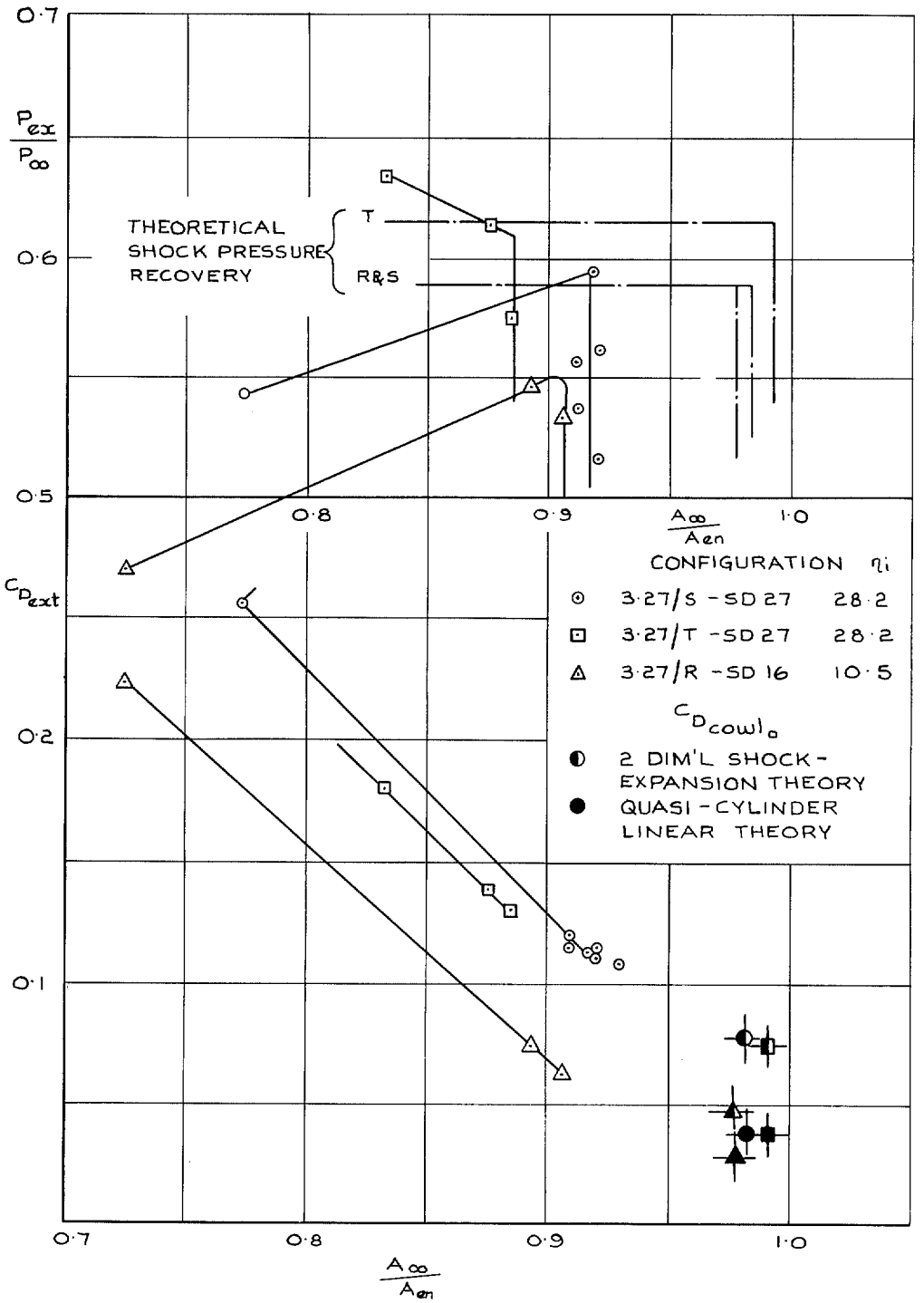

FIG. 15c. Drag and pressure recovery of Isen 3·27/R, S and T at $M_\infty = 3{\cdot}27$.

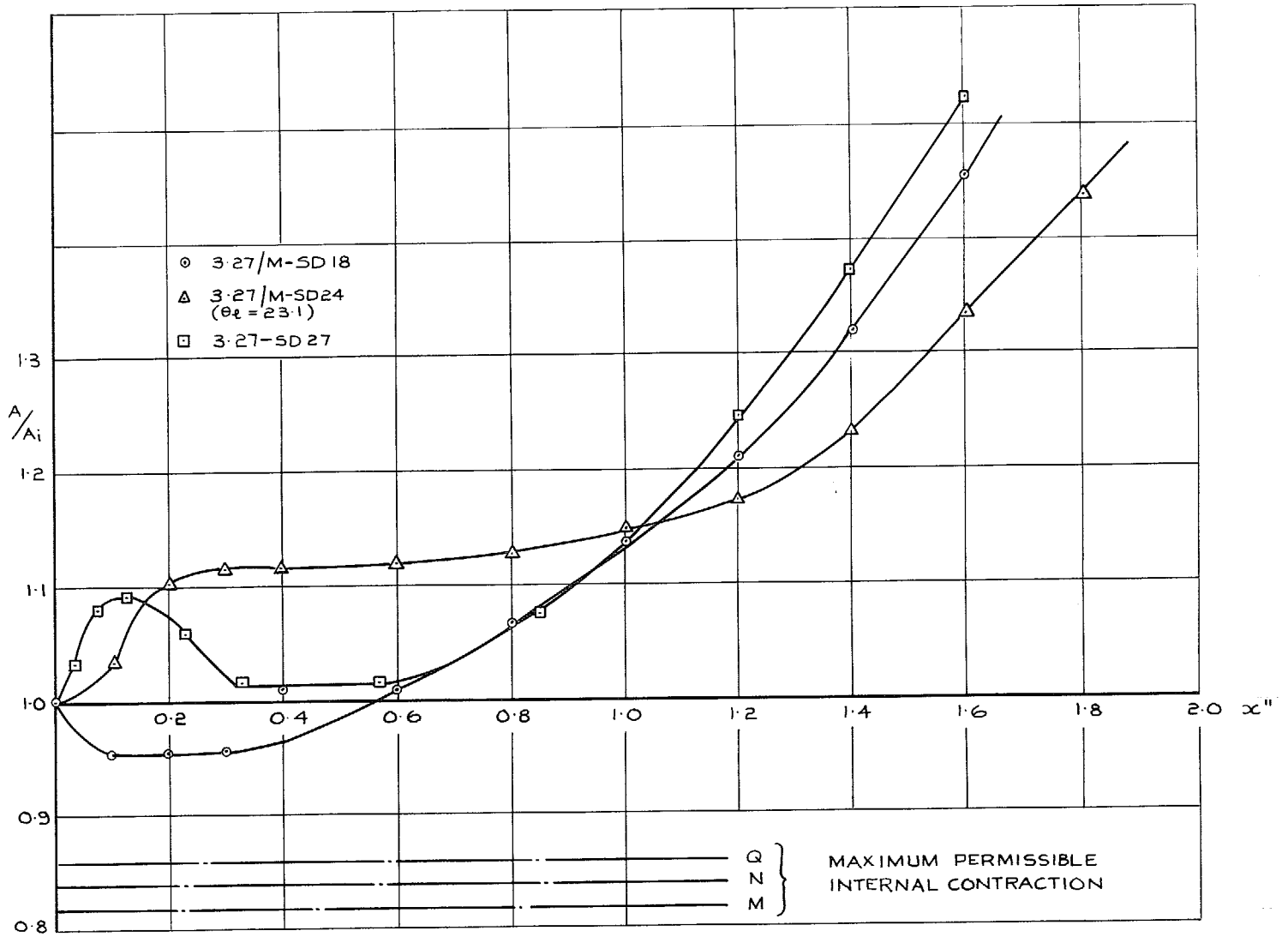

FIG. 16a. Duct internal area distributions.

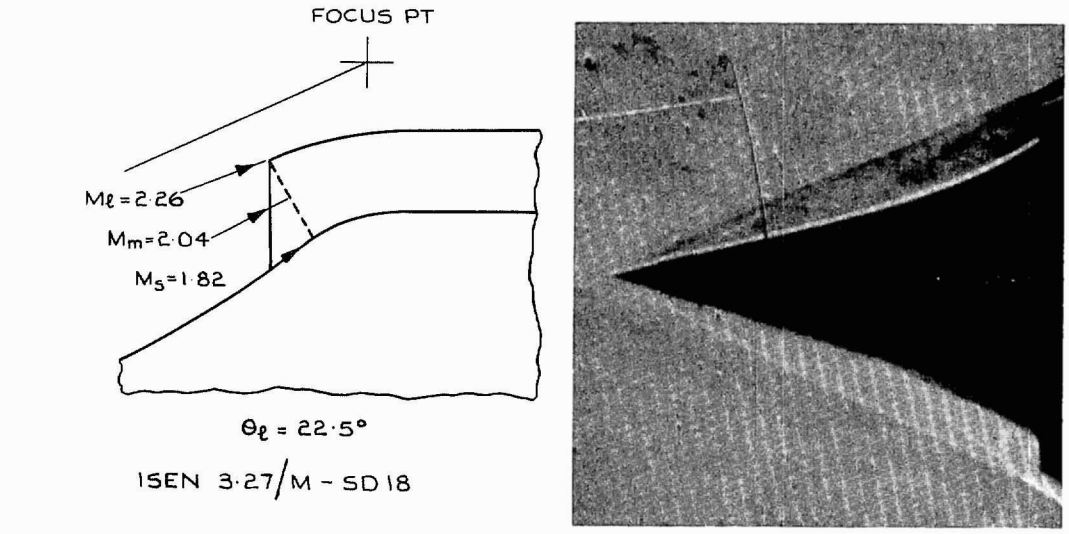

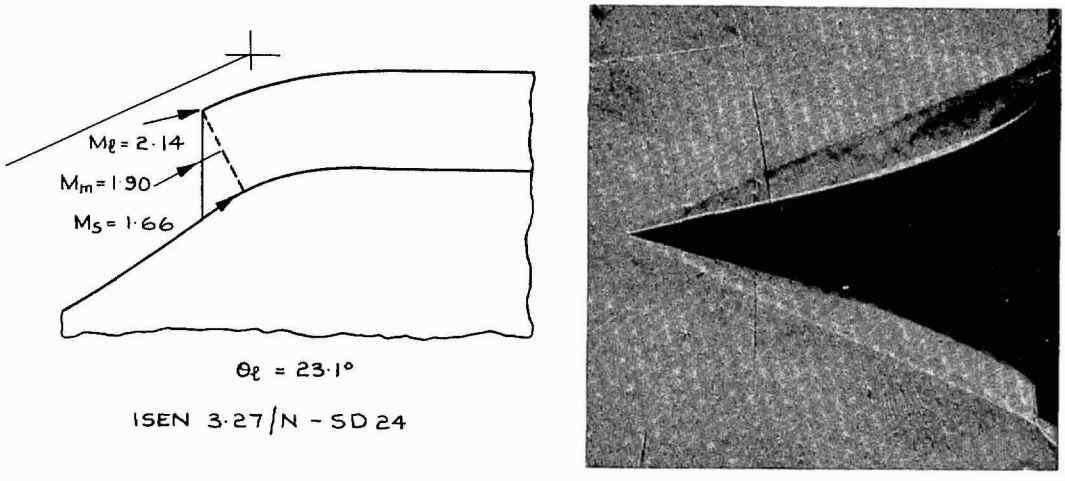

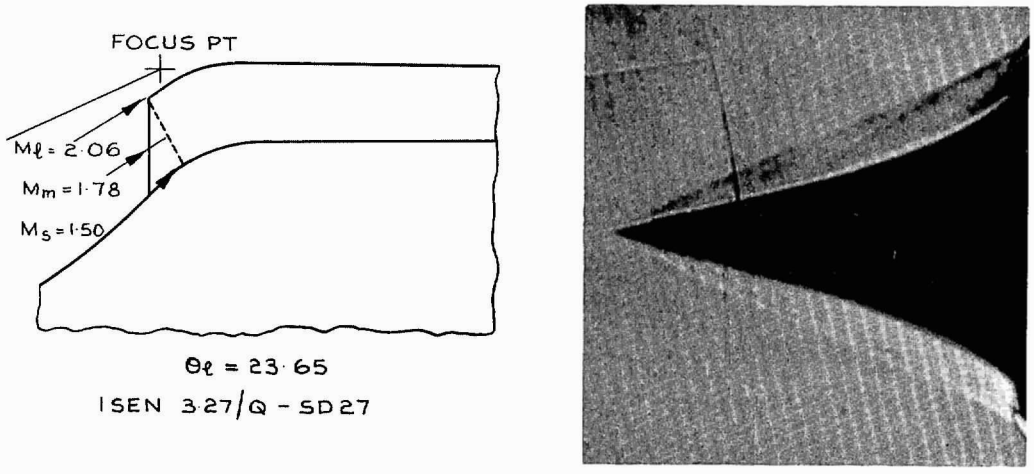

FIG. 16b. Theoretical and actual flow configurations.

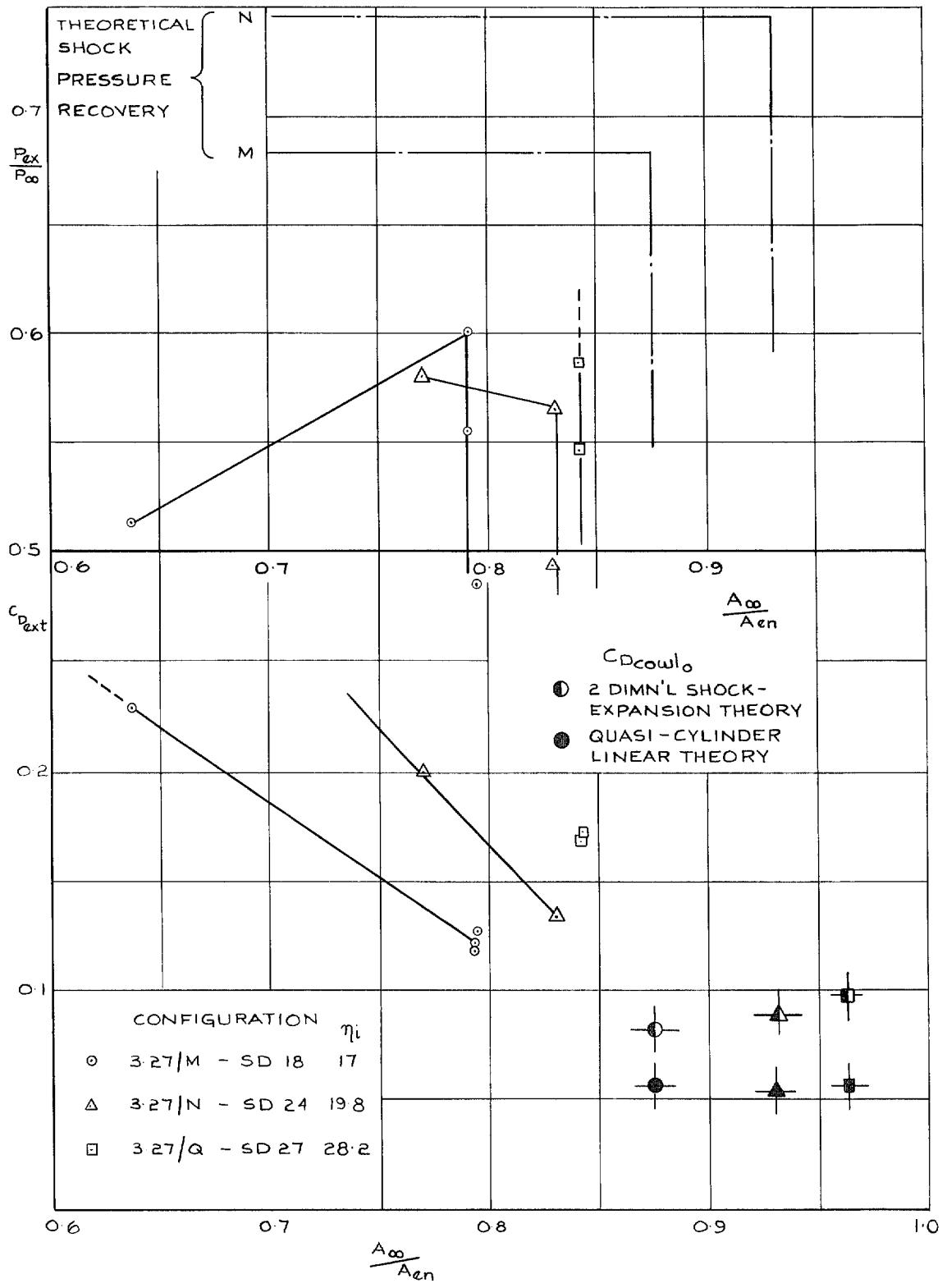

FIG. 16c. Drag and pressure of Isen 3·27/M, N and Q at $M_\infty = 3{\cdot}27$.

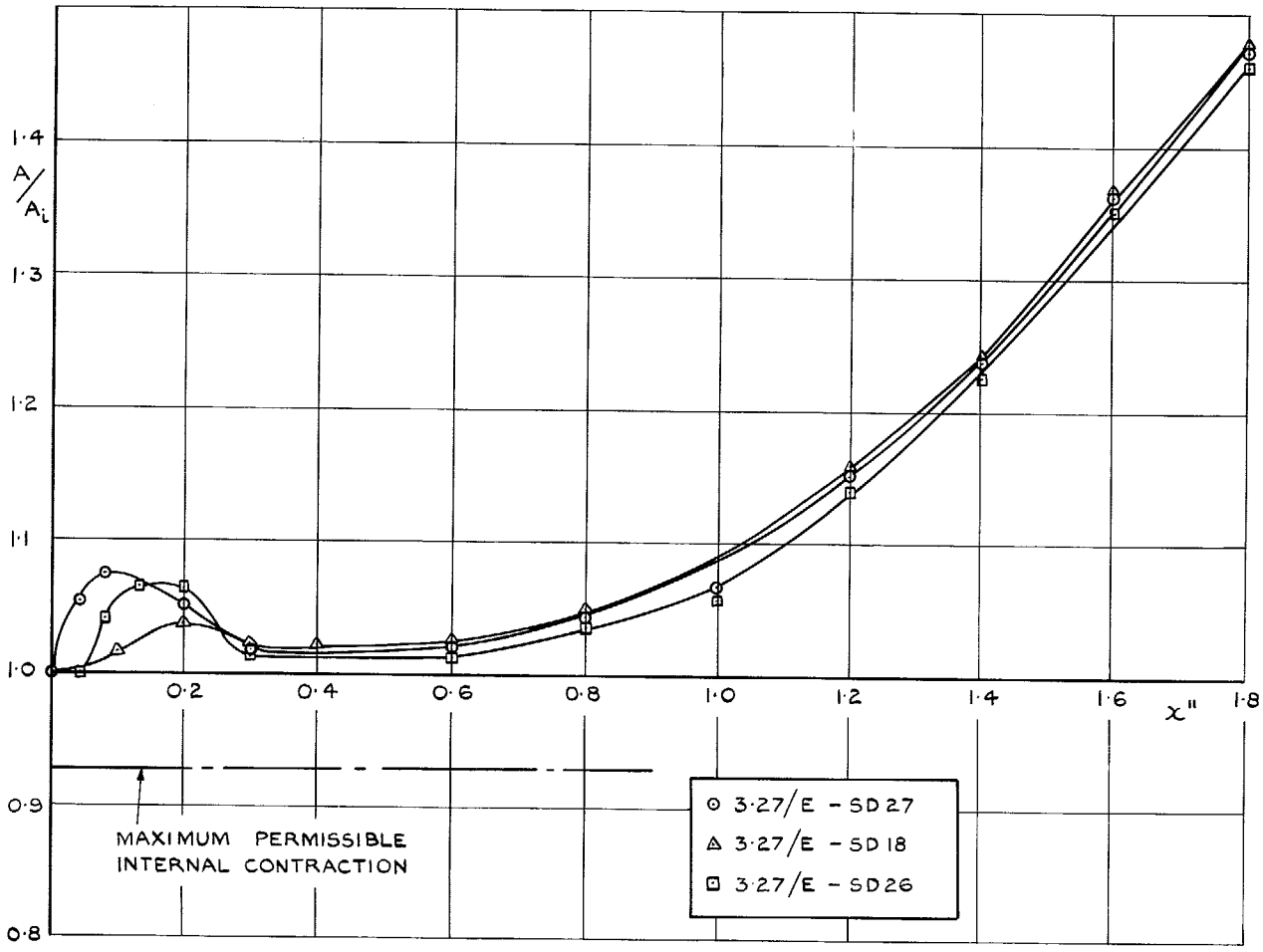

FIG. 17a. Duct internal area distributions.

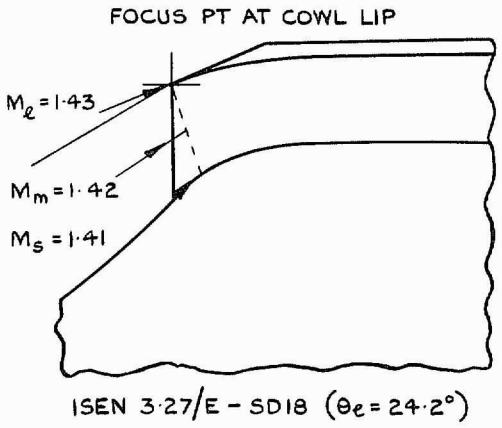

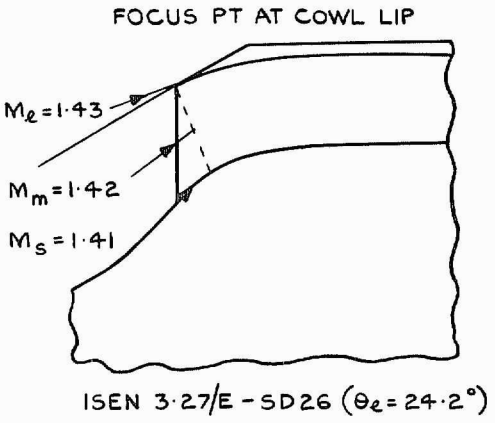

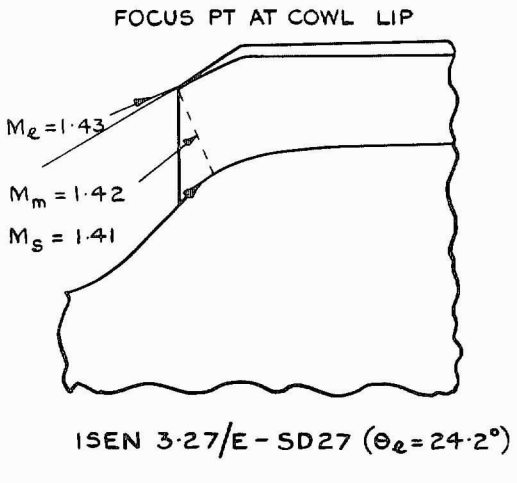

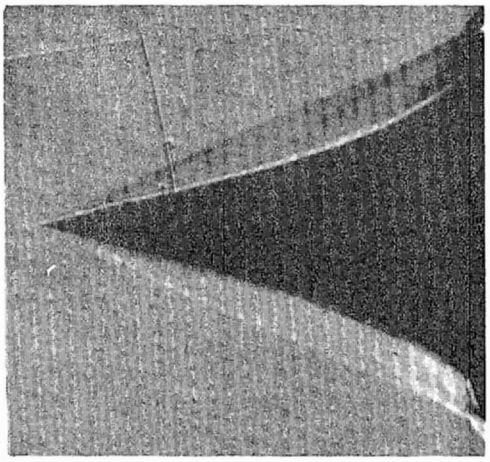

FIG. 17b. Theoretical and actual flow configurations.

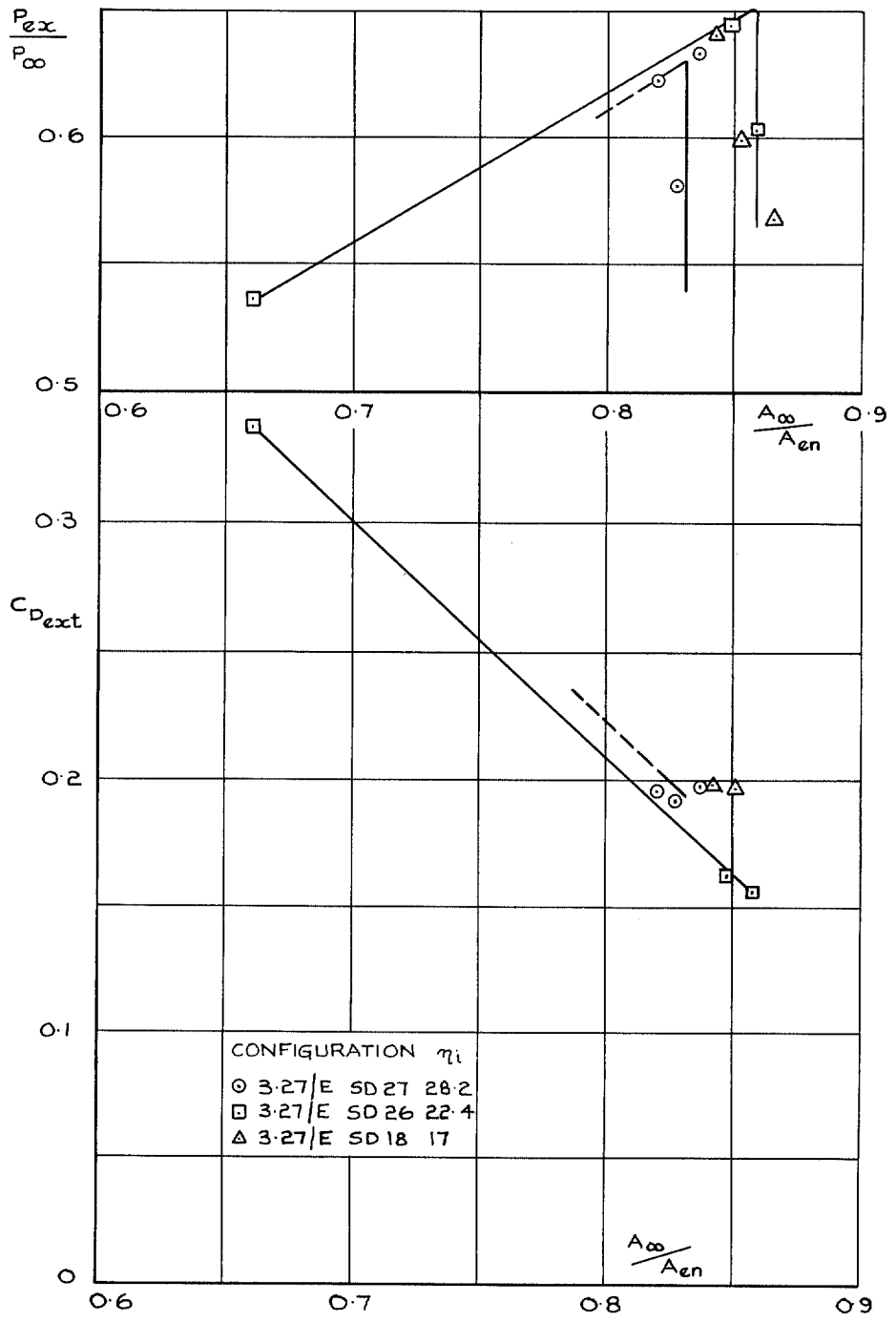

FIG. 17c. Drag and pressure recovery of Isen 3·27/E at $M_\infty = 3{\cdot}27$.

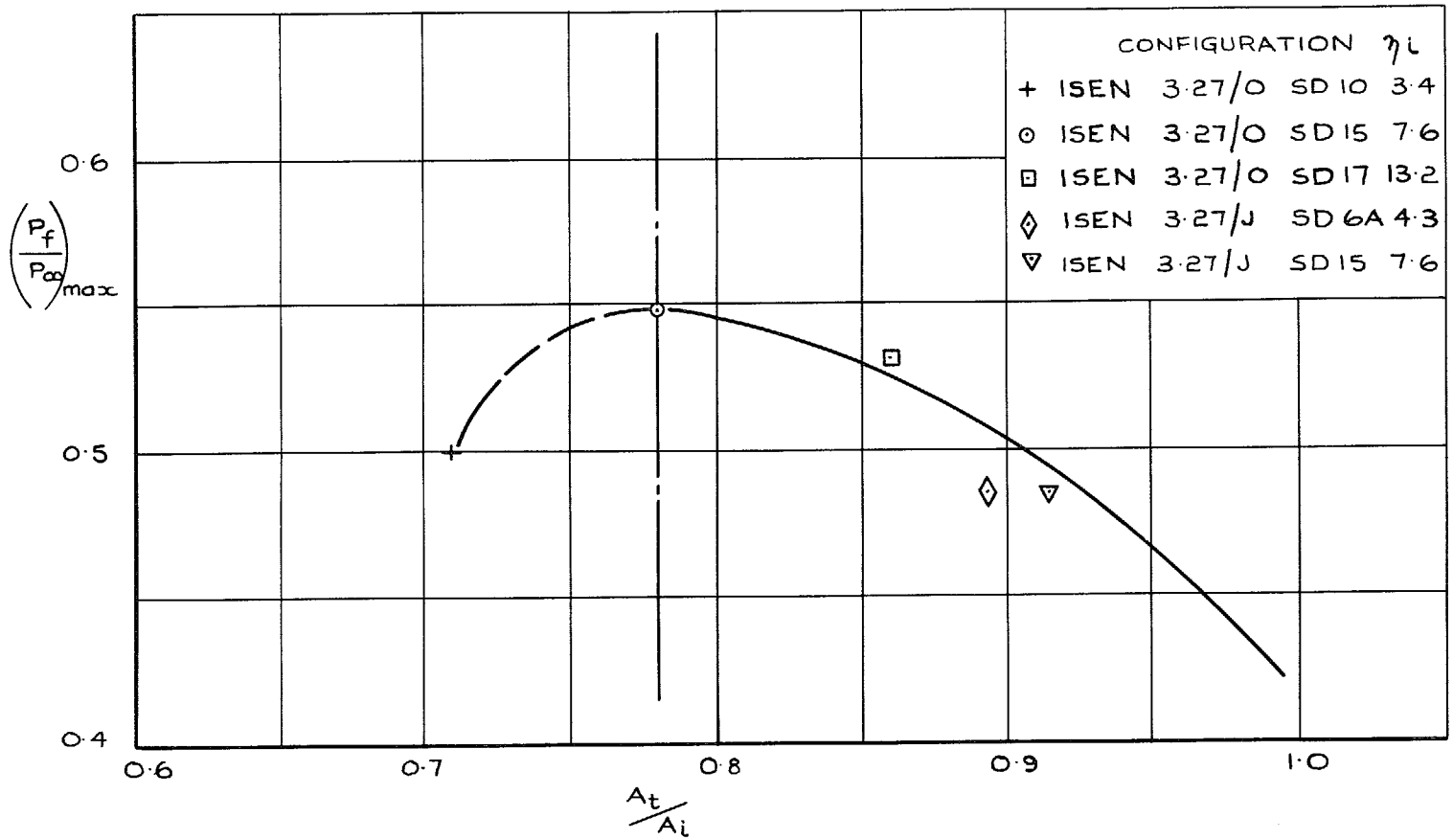

FIG. 18. Effect of internal contraction on pressure recovery.

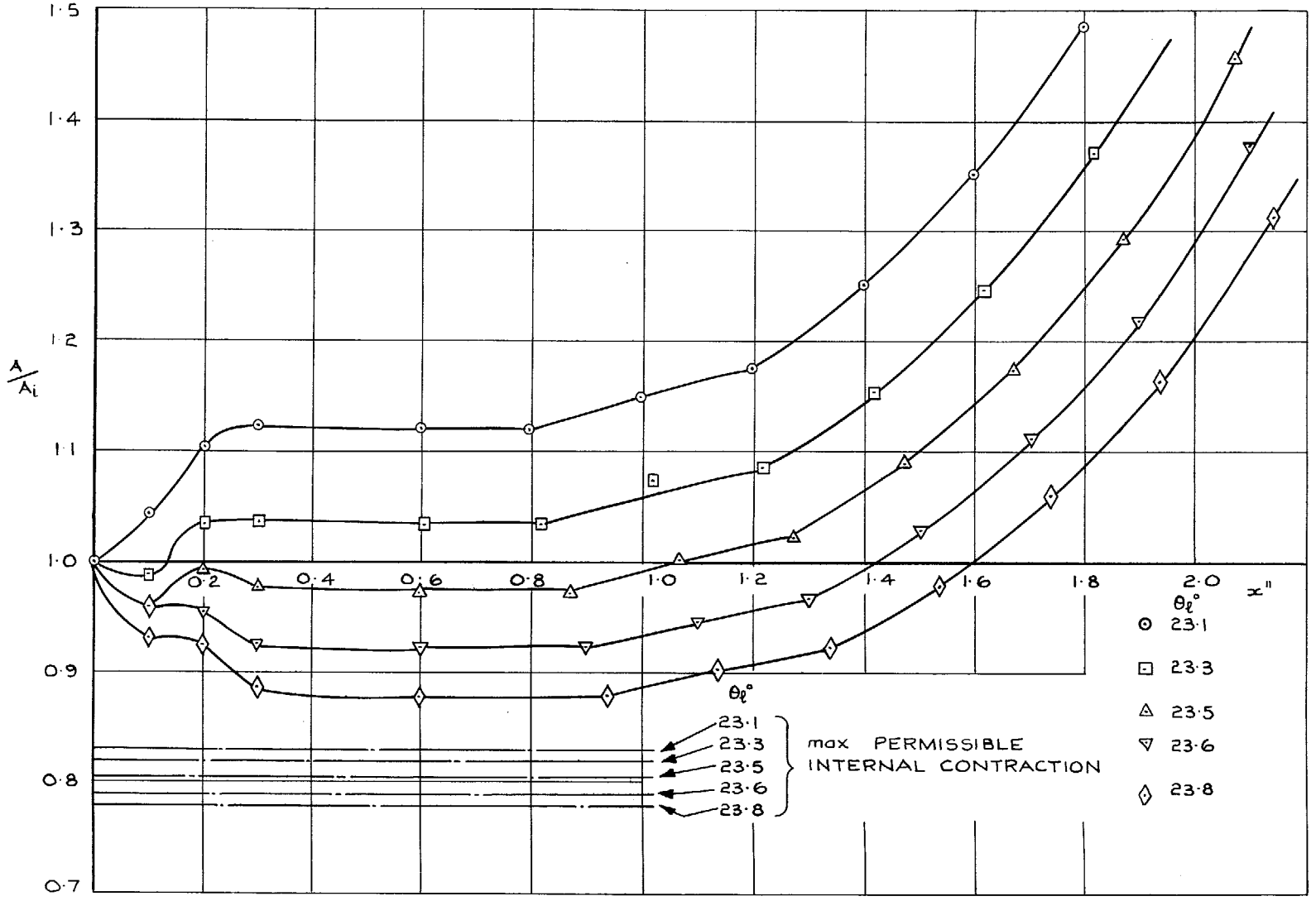

FIG. 19a. Duct internal area distributions.

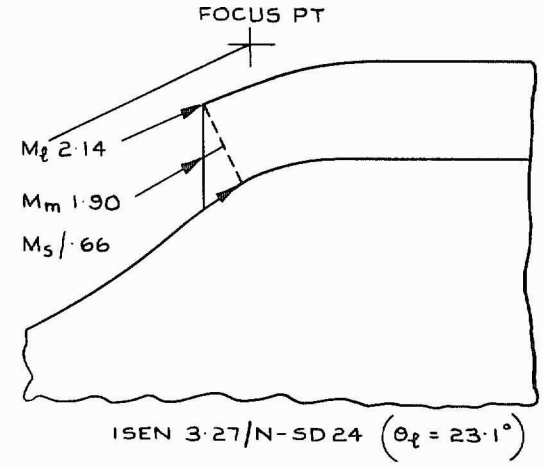

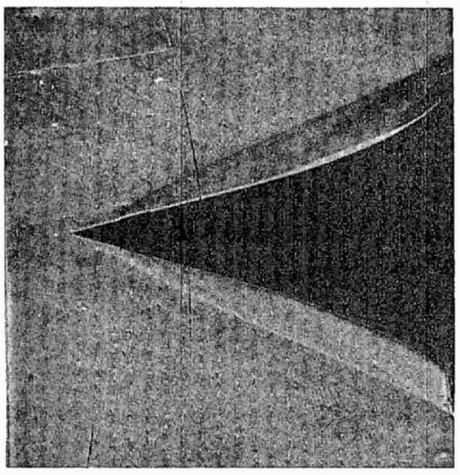

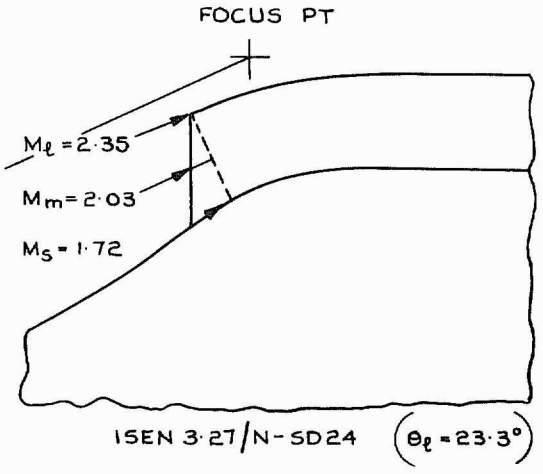

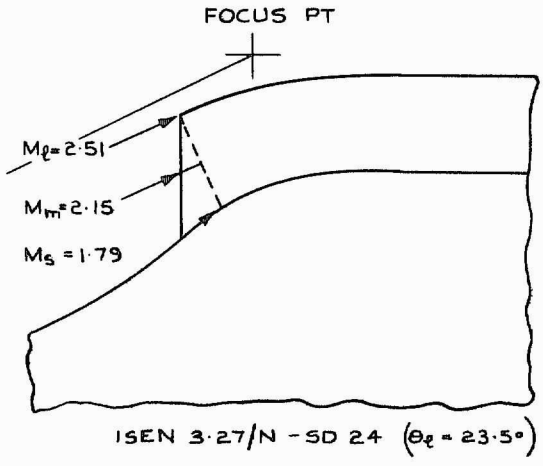

FIG. 19b. Theoretical and actual flow configurations.

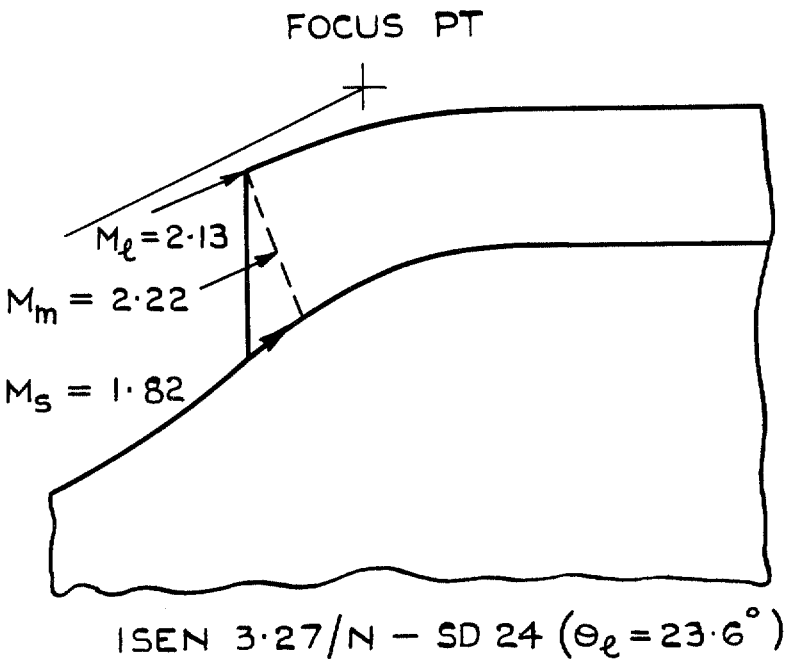

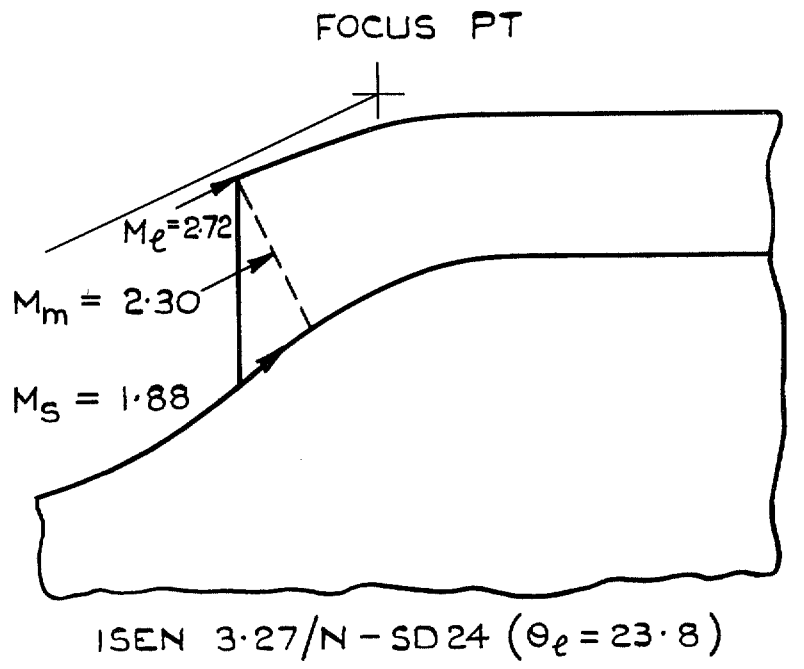

FIG. 19b (cont.). Theoretical flow configurations.

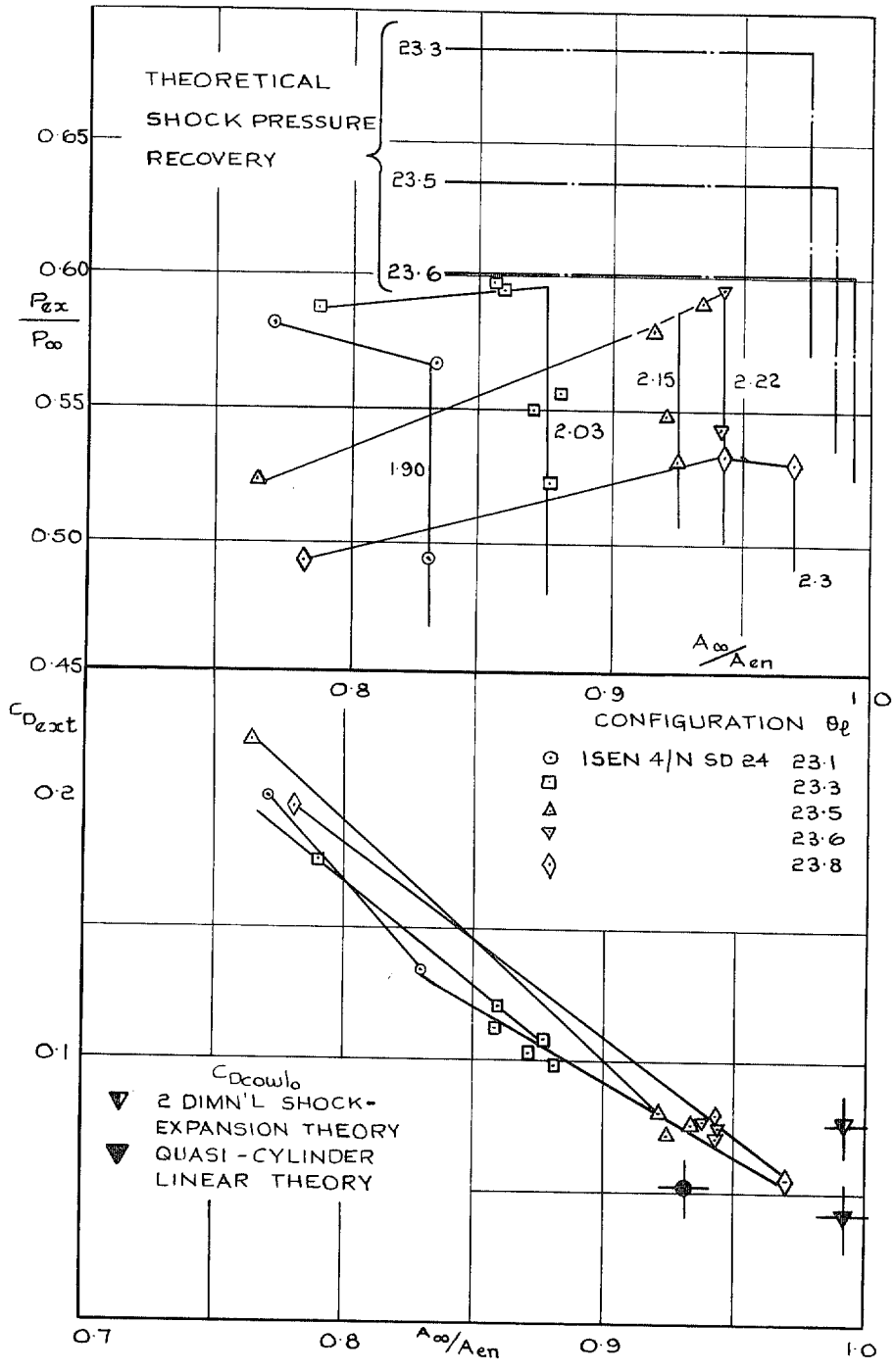

FIG. 19c. Drag and pressure recovery of Isen 3·27/N at $M_\infty = 3{\cdot}27$ (effect of withdrawing centrebody).

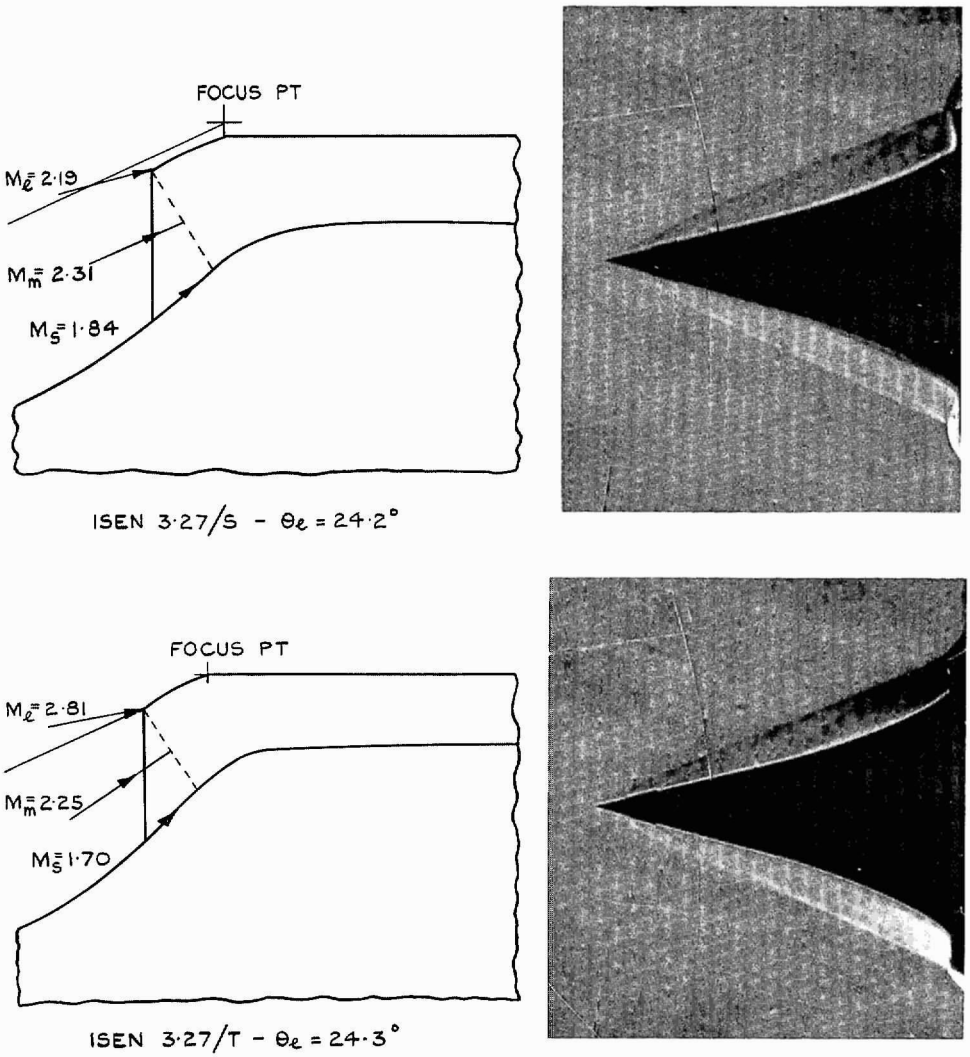

FIG. 20a. Theoretical and actual flow configurations.

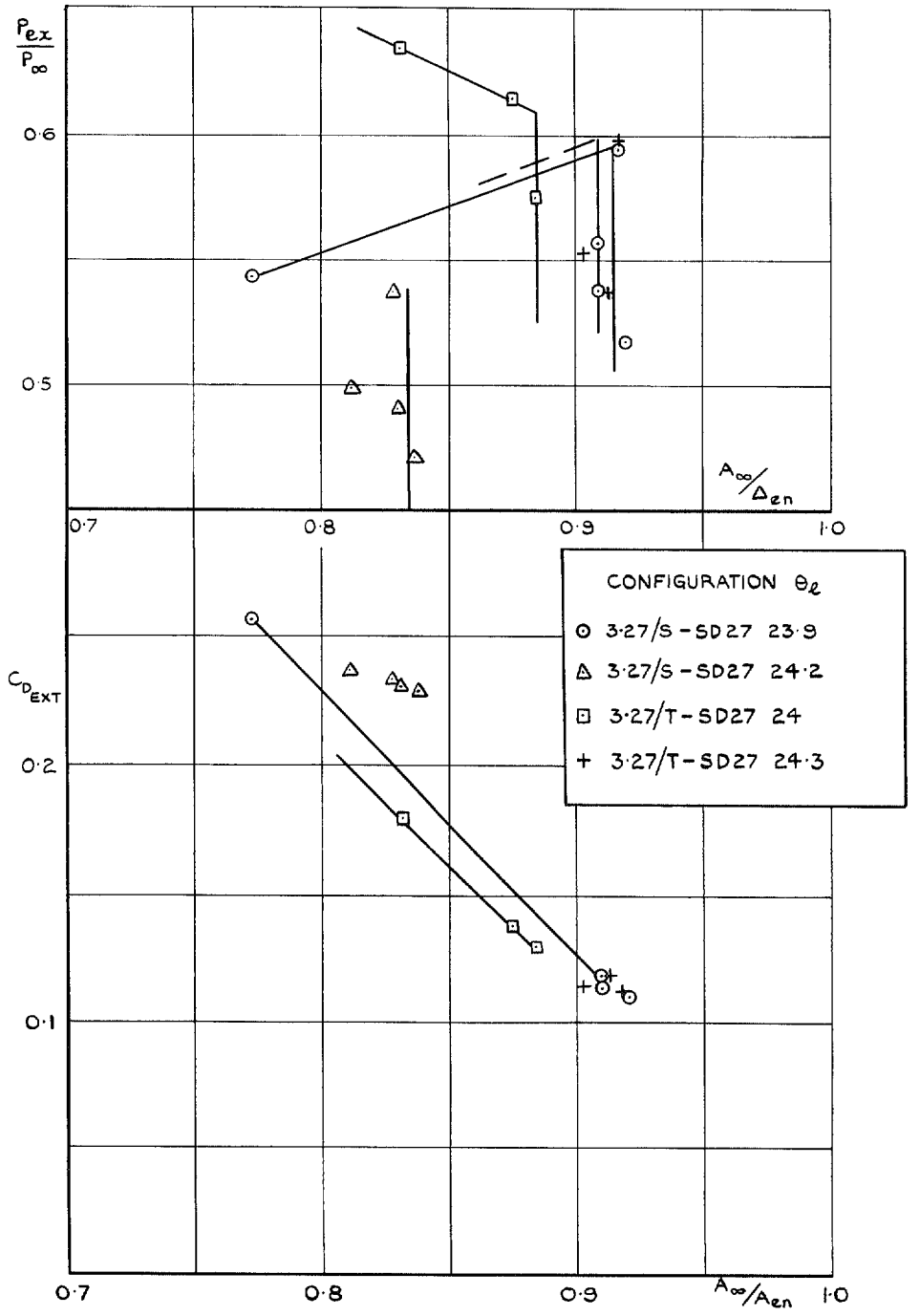

FIG. 20b. Effect of withdrawing centrebody for Isen 3·27/S and T at $M_\infty = 3{\cdot}27$.

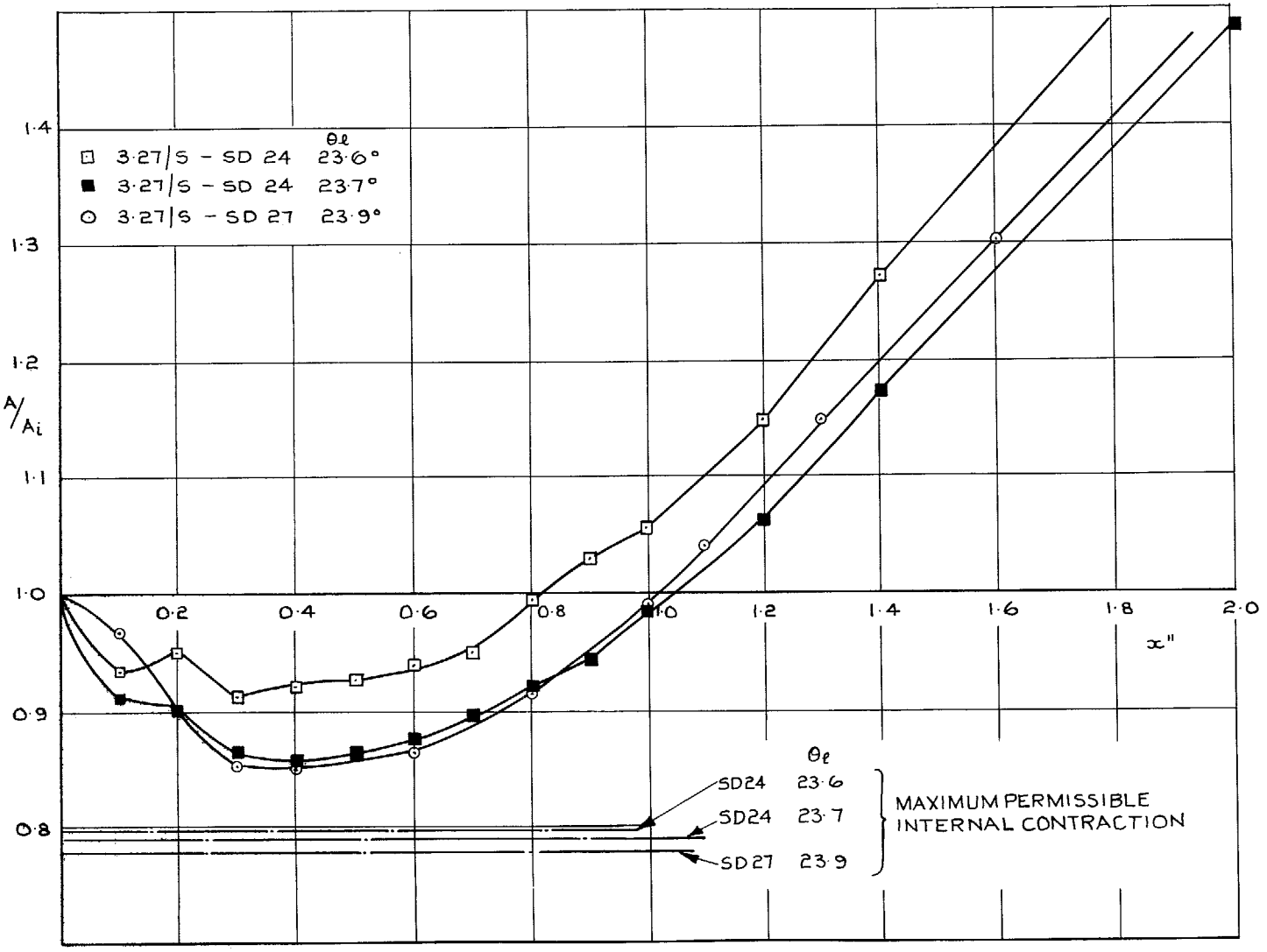

FIG. 21a. Duct internal area distributions.

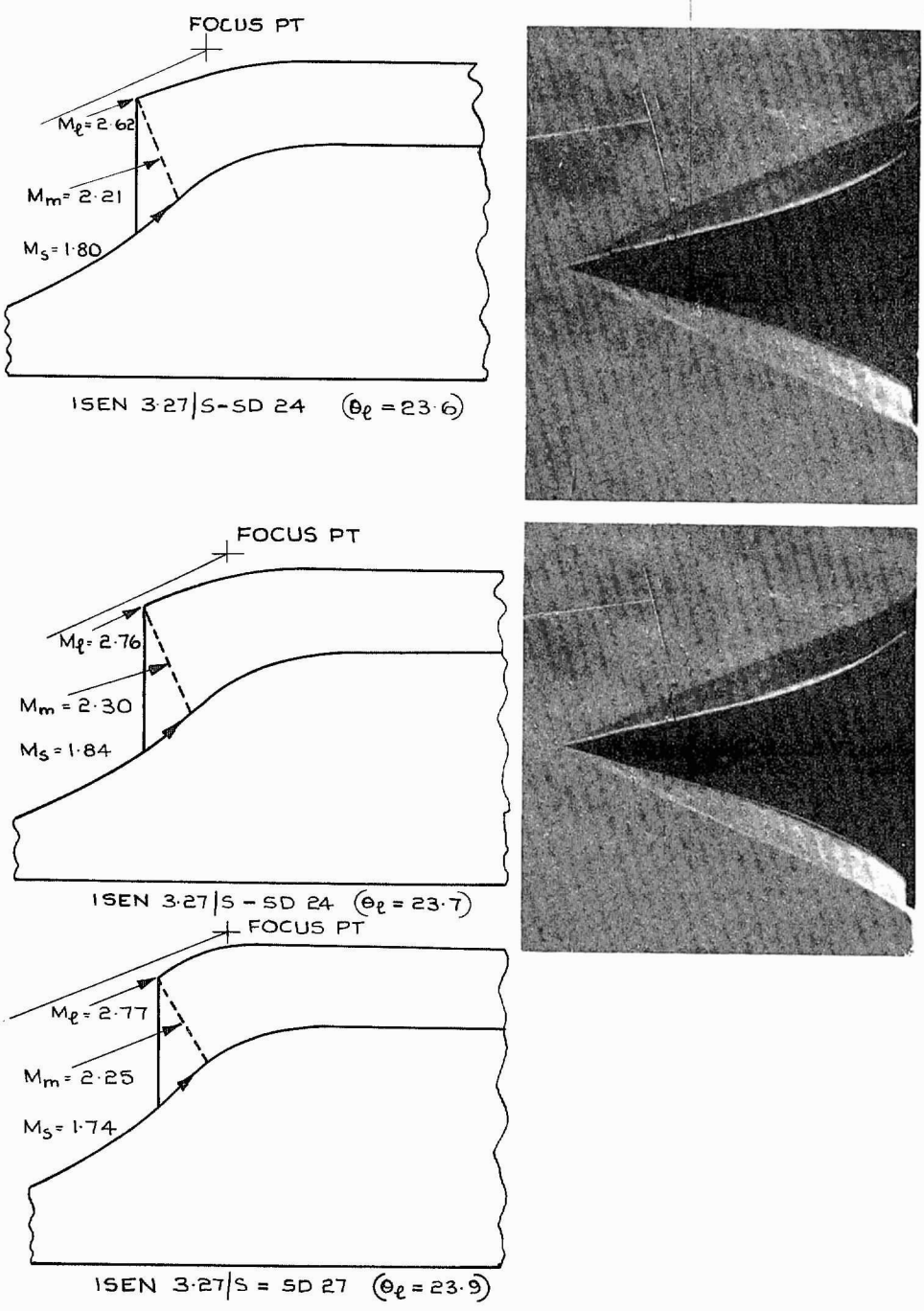

FIG. 21b. Theoretical and actual flow configurations.

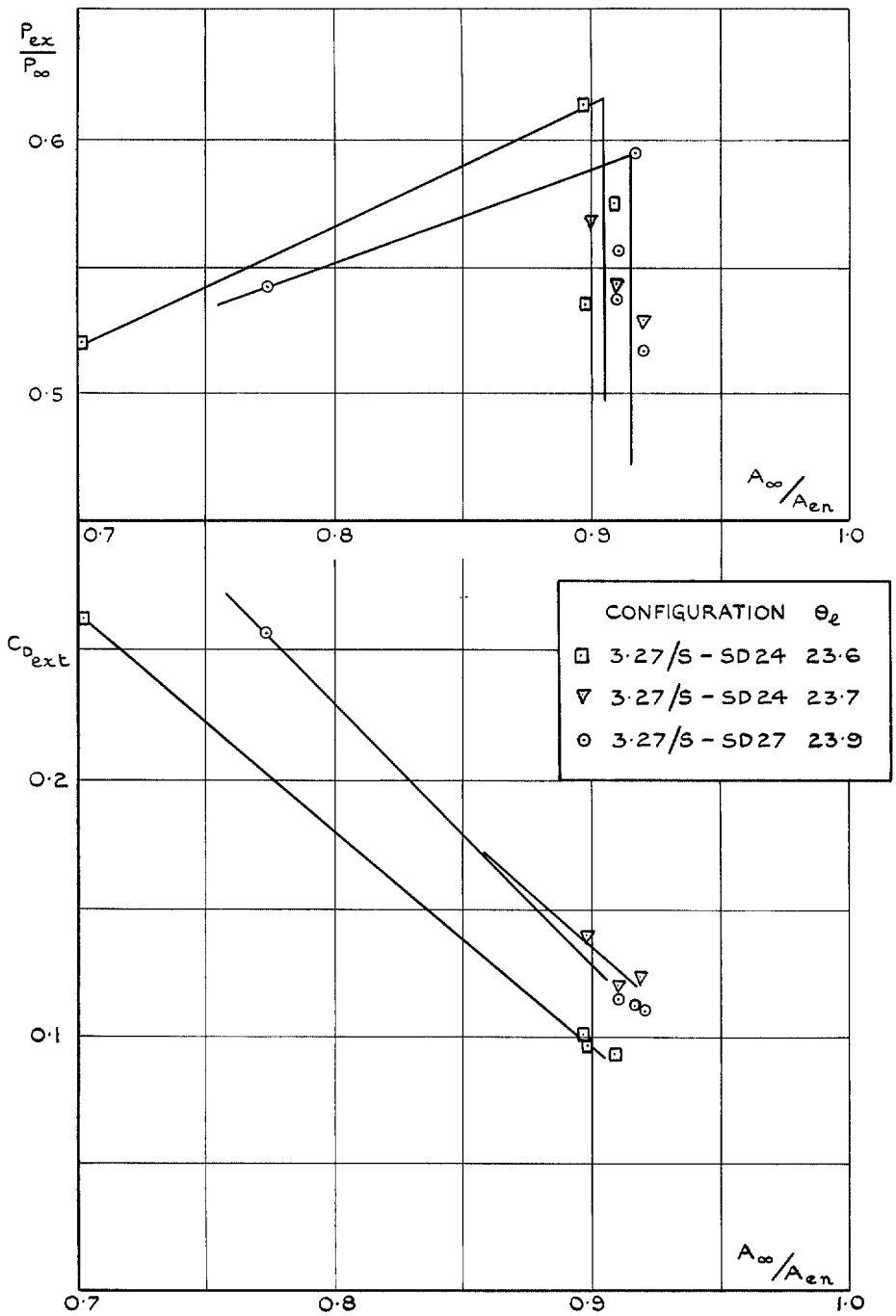

FIG. 21c. Effect of changing cowl shape for Isen 3·27/S at $M_\infty = 3·27$.

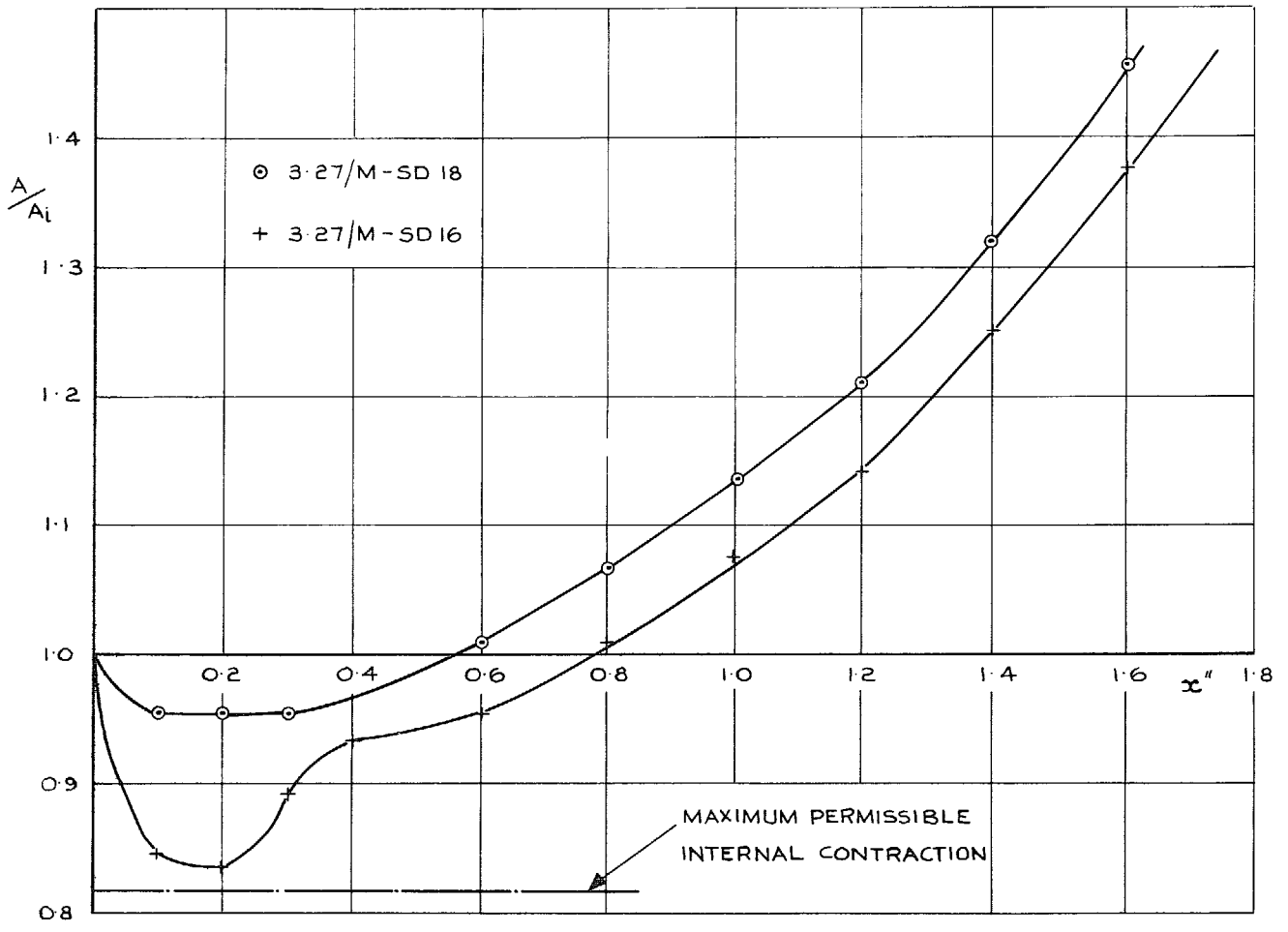

FIG. 22a. Duct internal area distributions.

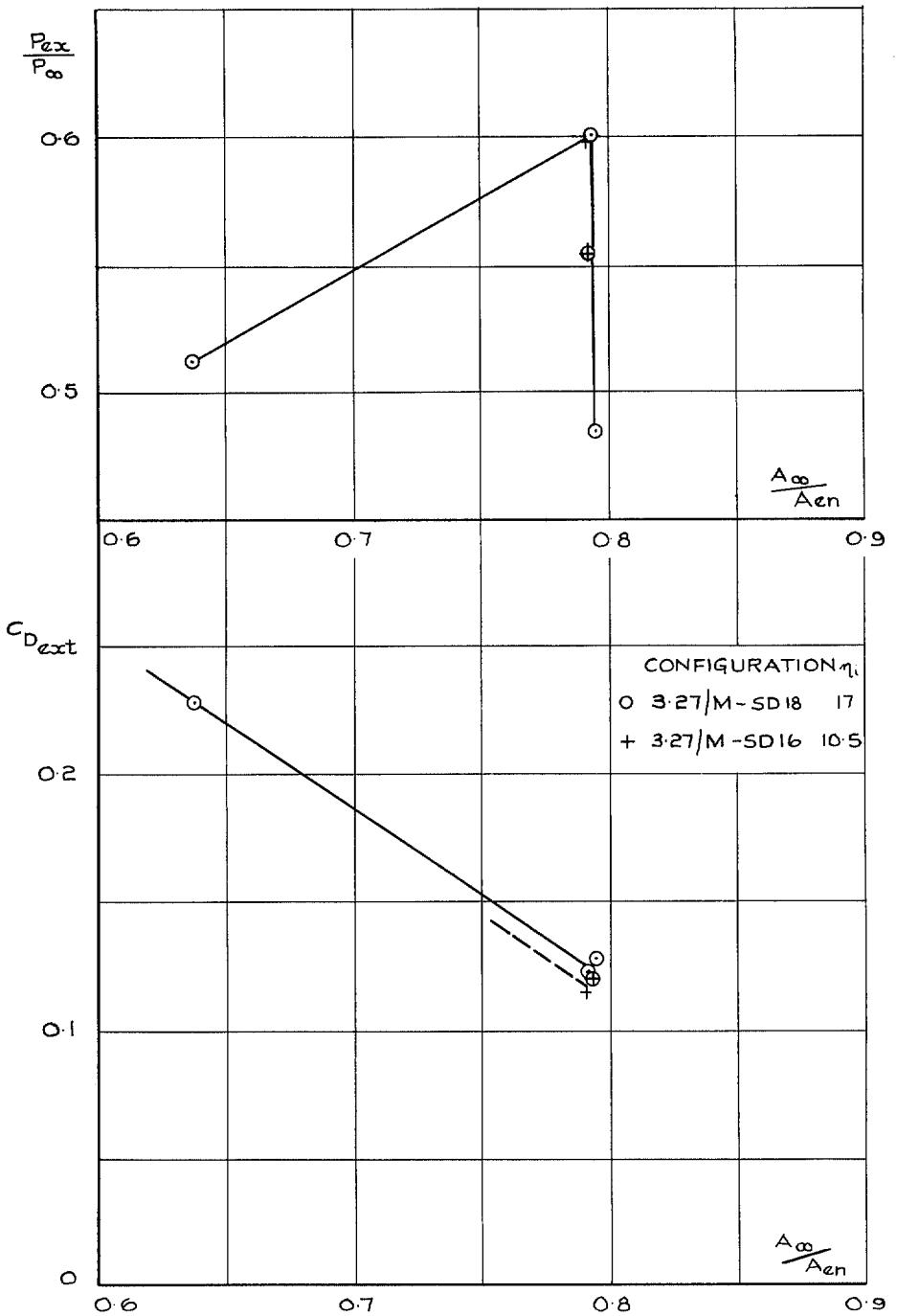

FIG. 22b. Effect of changing cowl shape for Isen 3·27/M at $M_\infty = 3{\cdot}27$.

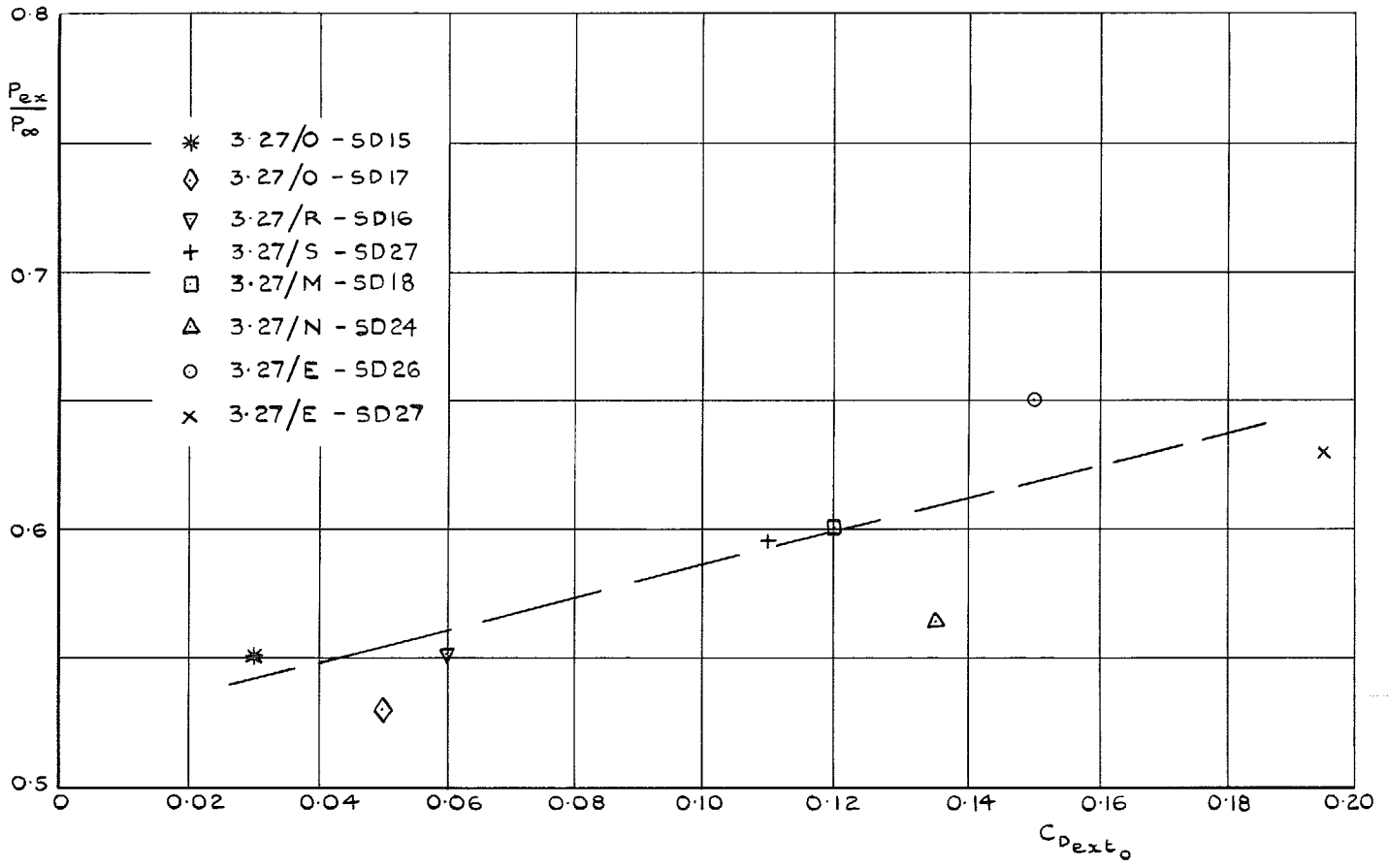

FIG. 23. Summary of pressure recovery and drag at full flow.

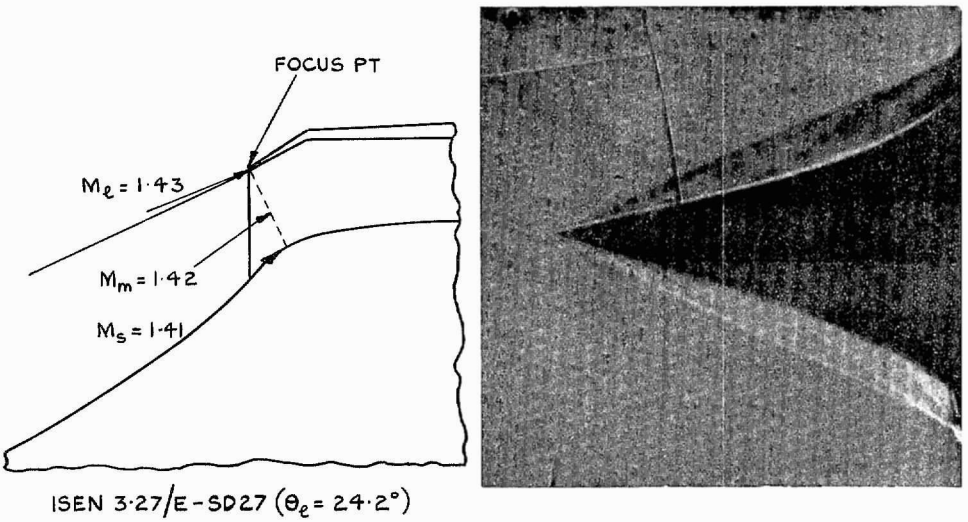

WITHOUT CENTREBODY BOUNDARY LAYER SUCTION

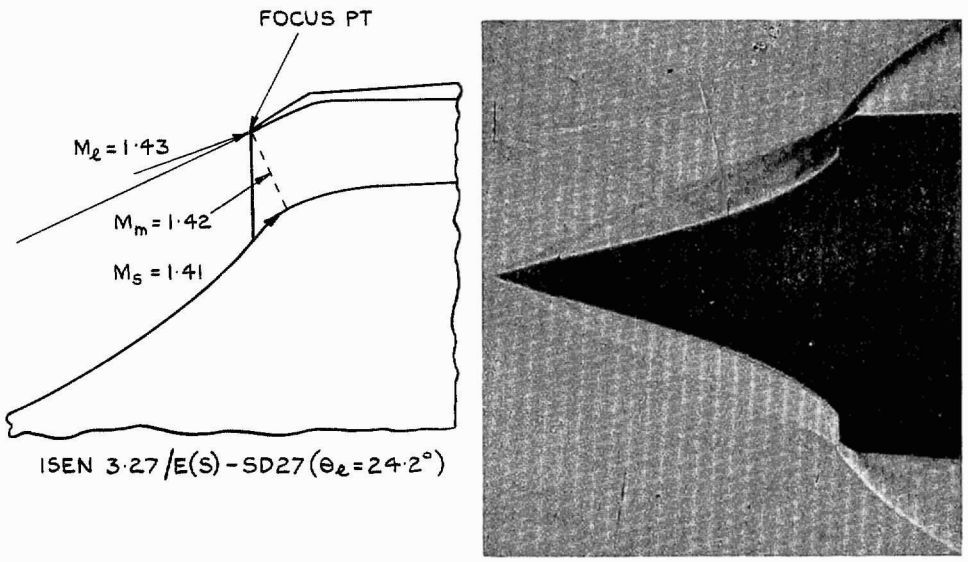

WITH CENTREBODY BOUNDARY LAYER SUCTION

FIG. 24a. Theoretical and actual flow configurations.

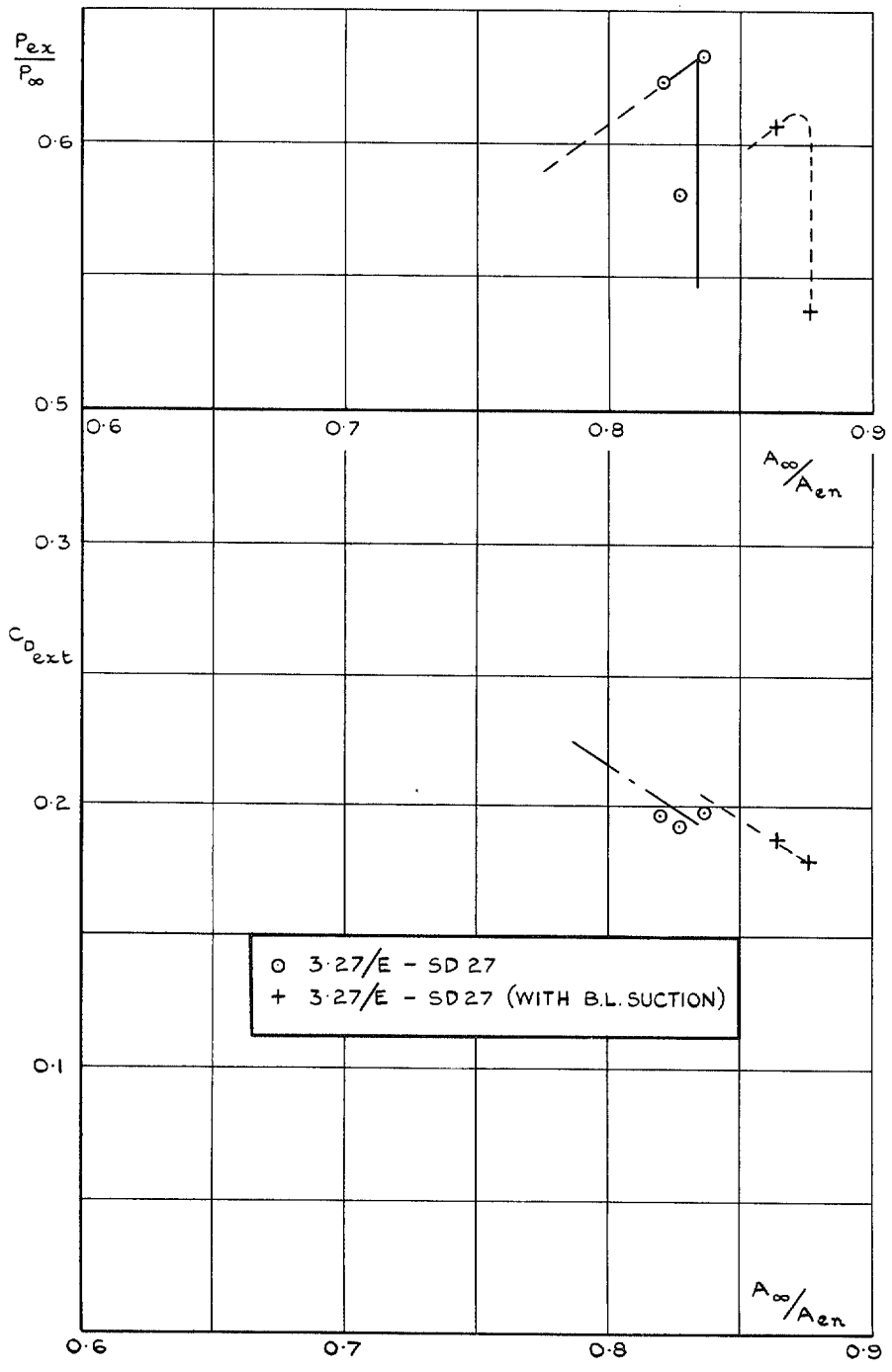

FIG. 24b. Drag and pressure recovery of Isen 3·27/E and E(S) at $M_\infty = 3{\cdot}27$.

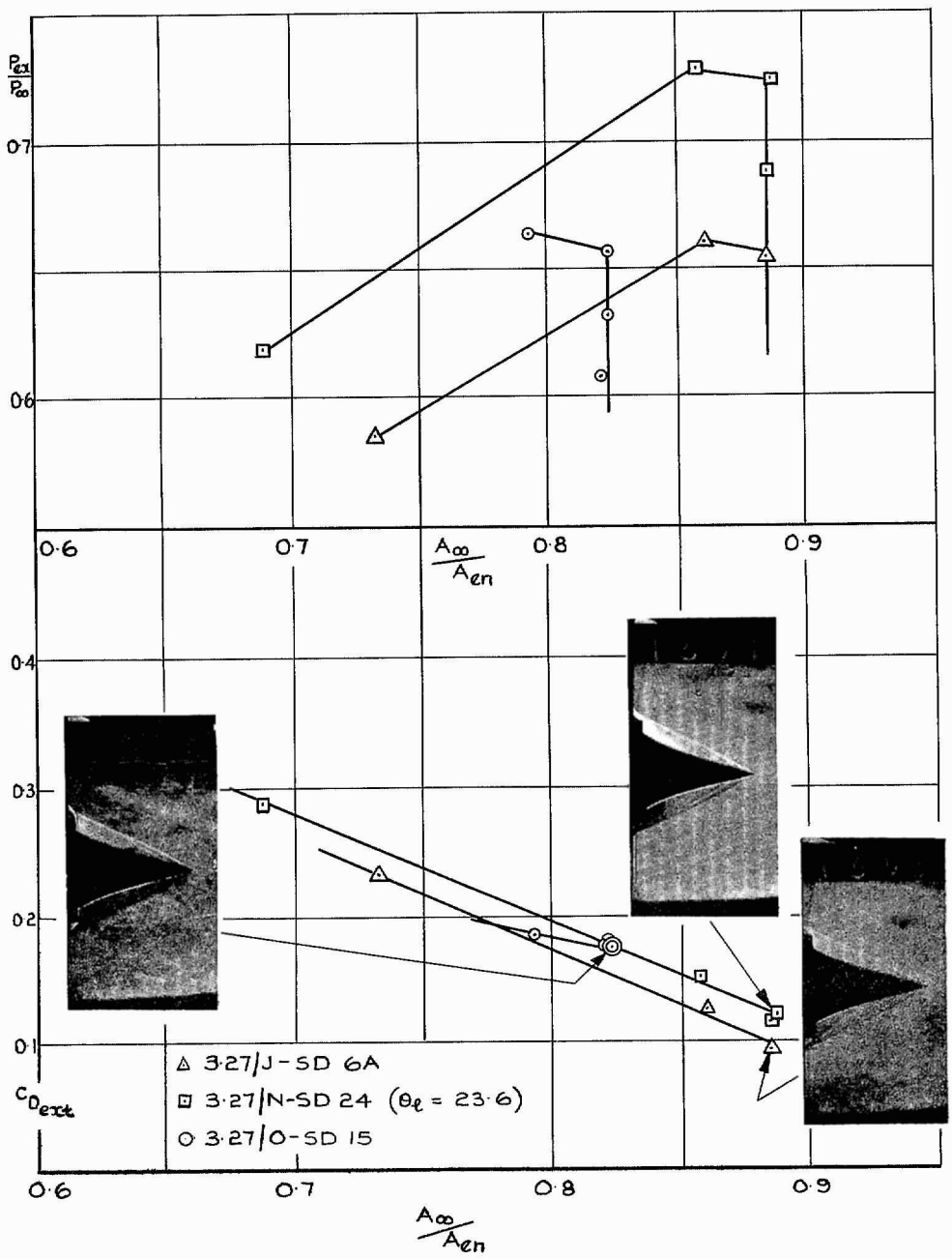

FIG. 25. Drag and pressure Recovery of Isen 3·27/J, N and O at $M_\infty = 2{\cdot}90$.

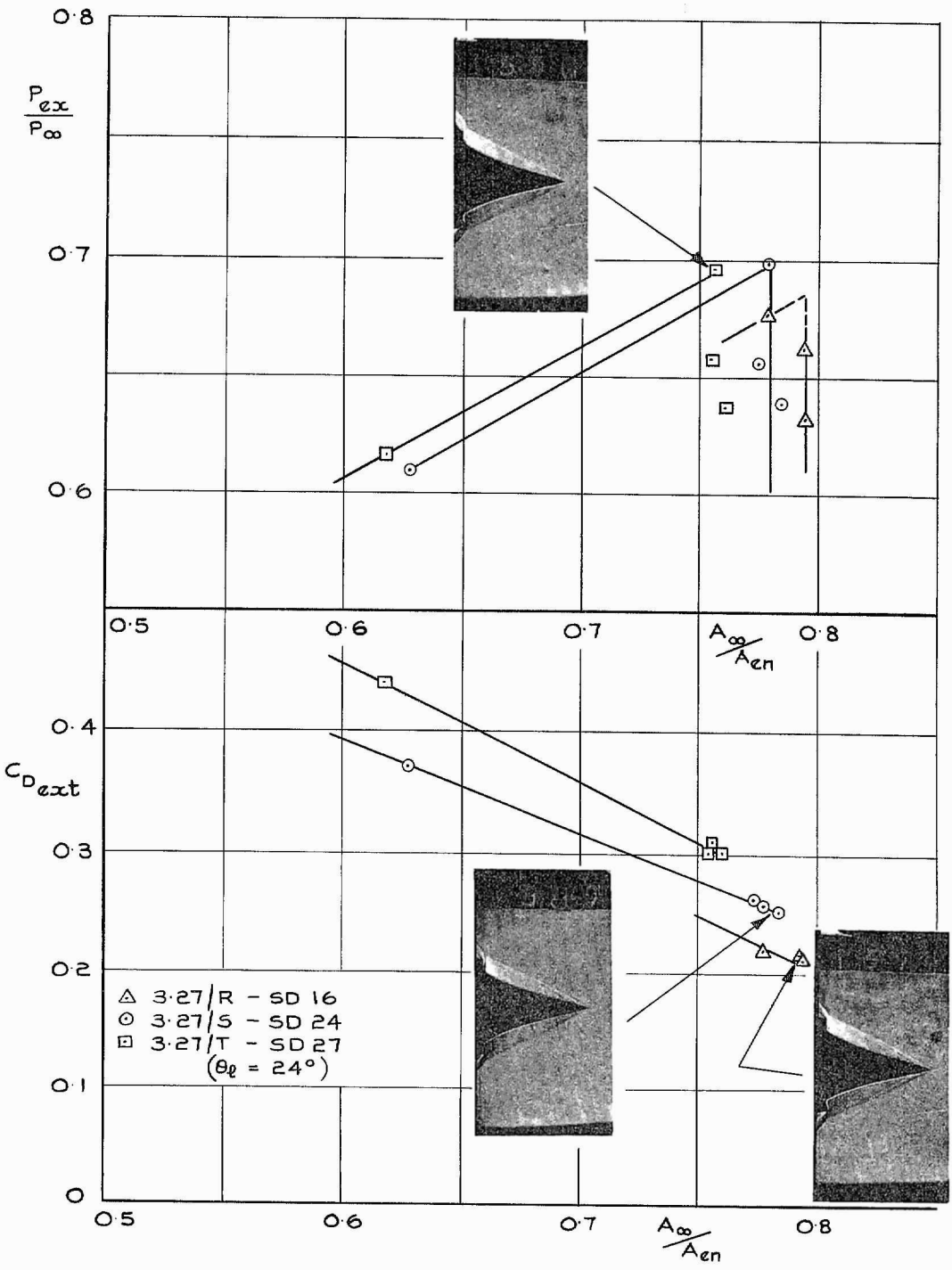

FIG. 26. Drag and pressure recovery of Isen 3·27/R, S and T at $M_\infty = 2.90$.

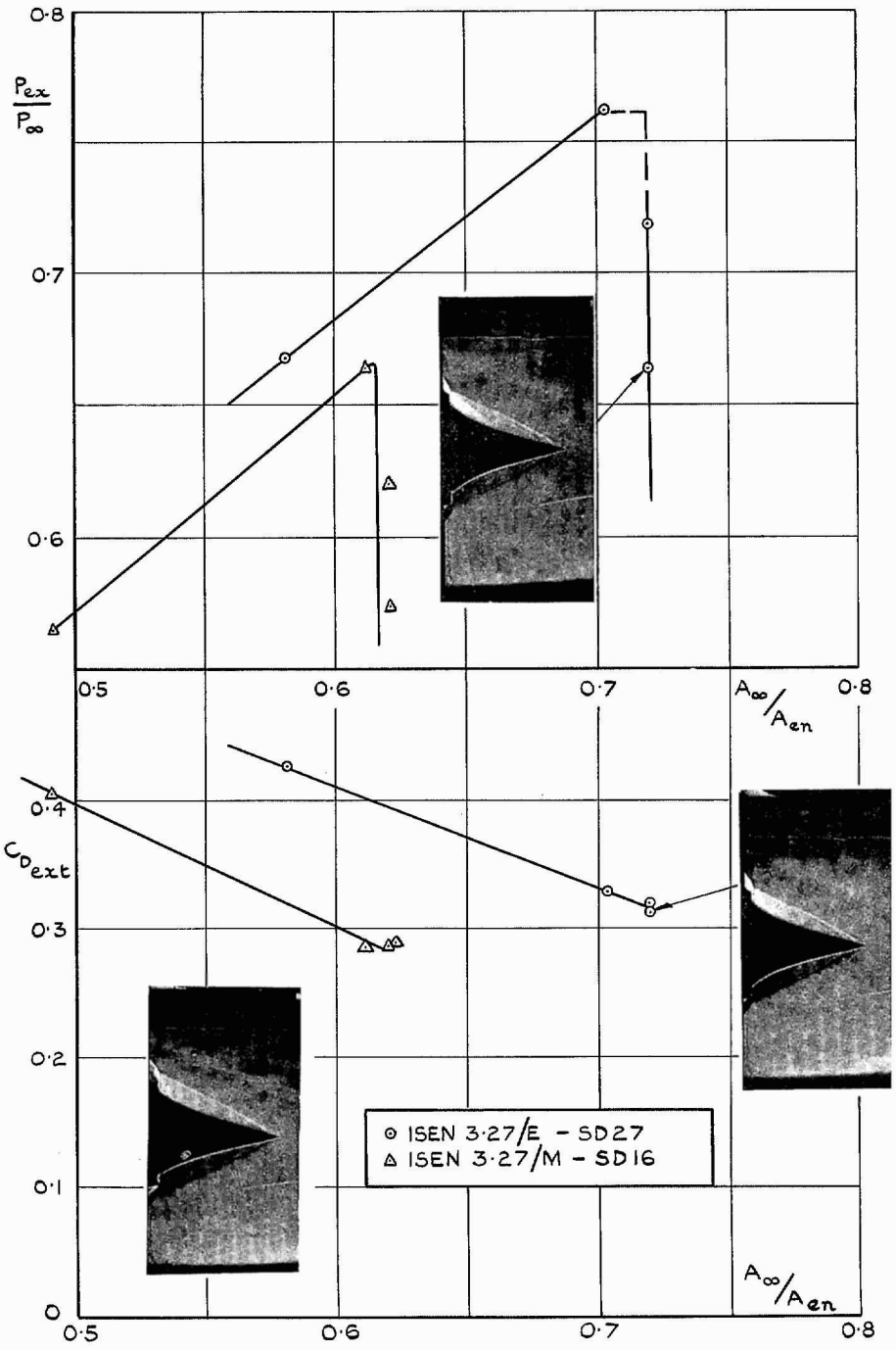

FIG. 27. Drag and pressure recovery of Isen 3·27/E and M at $M_\infty = 2{\cdot}90$.

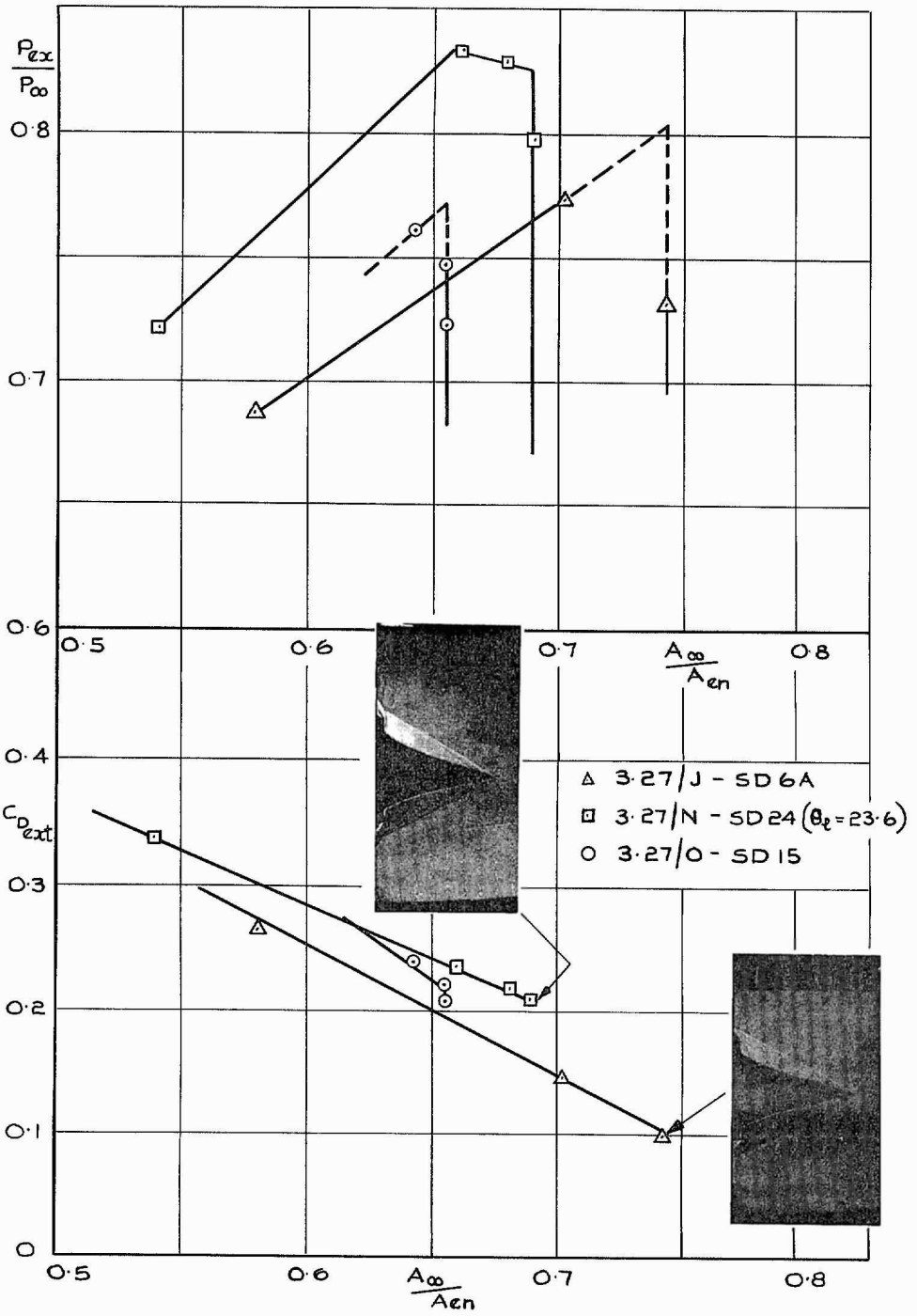

FIG. 28. Drag and pressure recovery of Isen 3·27/J, N and O at $M_\infty = 2{\cdot}48$.

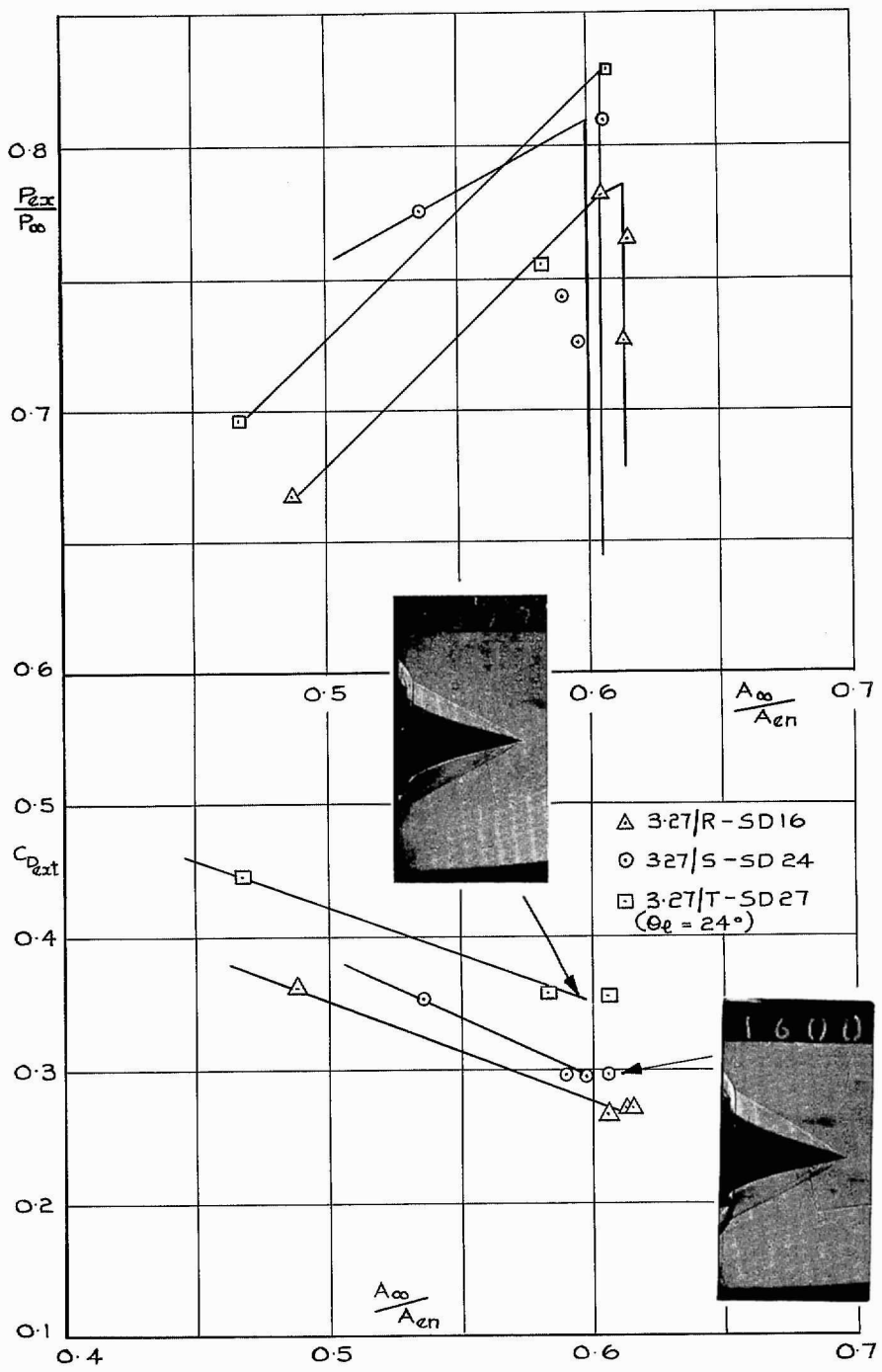

FIG. 29. Drag and pressure recovery of Isen 3·27/R, S and T at $M_\infty = 2{\cdot}48$.

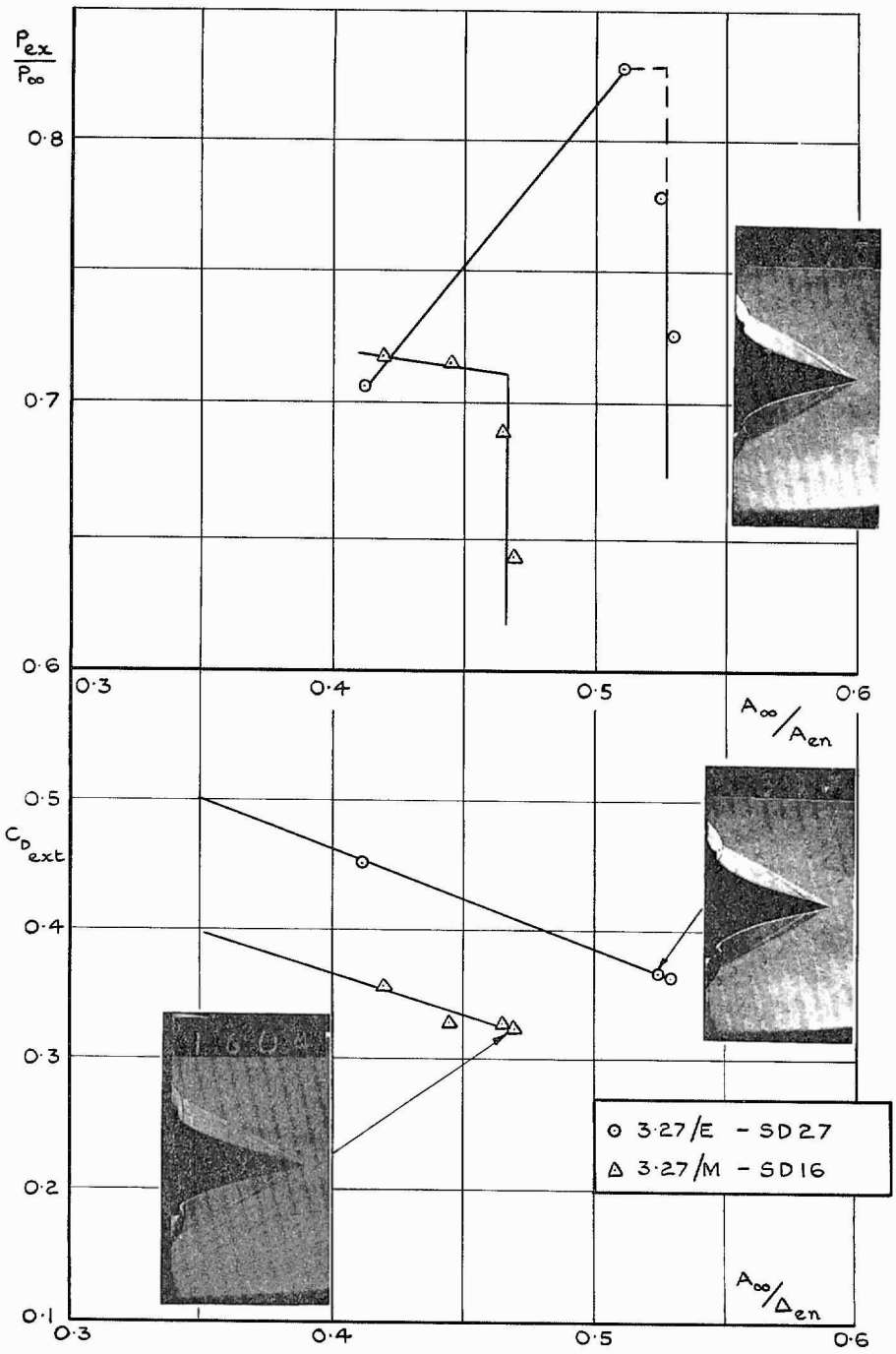

FIG. 30. Drag and pressure recovery of Isen 3·27/E and M at $M_\infty = 2{\cdot}48$.

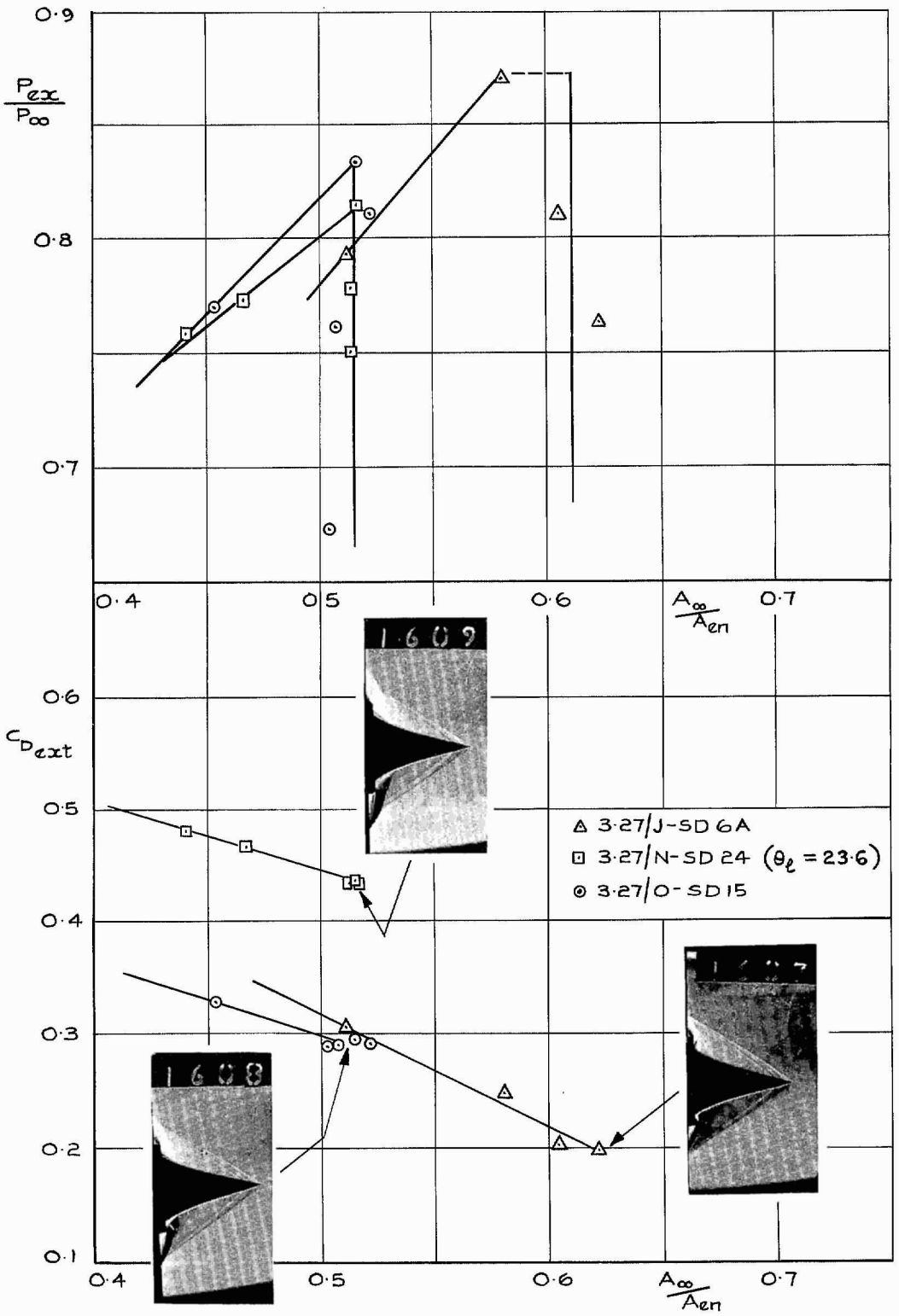

FIG. 31. Drag and pressure recovery of Isen 3·27/J, N and O at $M_\infty = 2·14$.

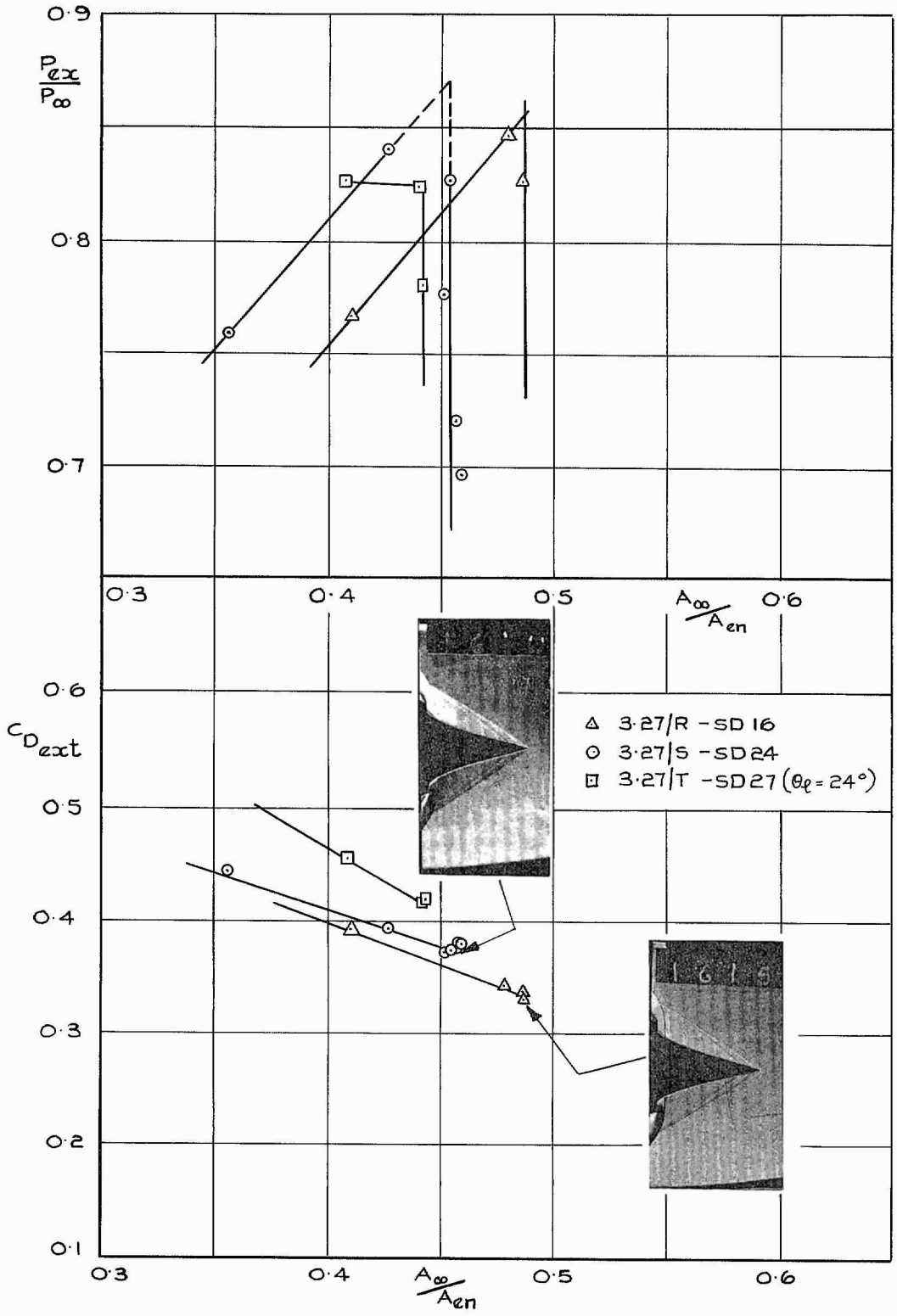

FIG. 32. Drag and pressure recovery of Isen 3·27/R, S and T at $M_\infty = 2{\cdot}14$.

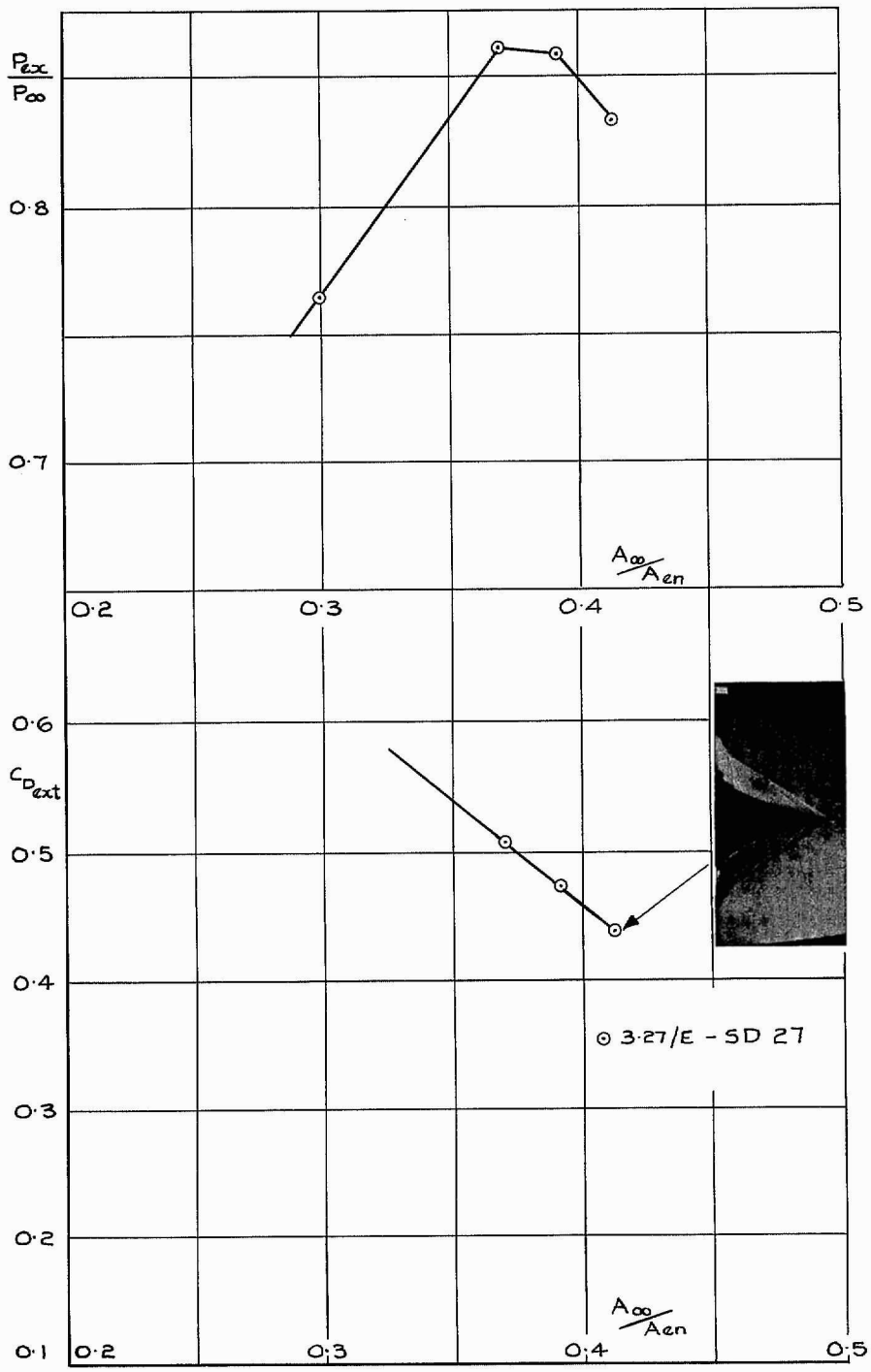

FIG. 33. Drag and pressure recovery of Isen 3·27/E at $M_\infty = 2{\cdot}14$.

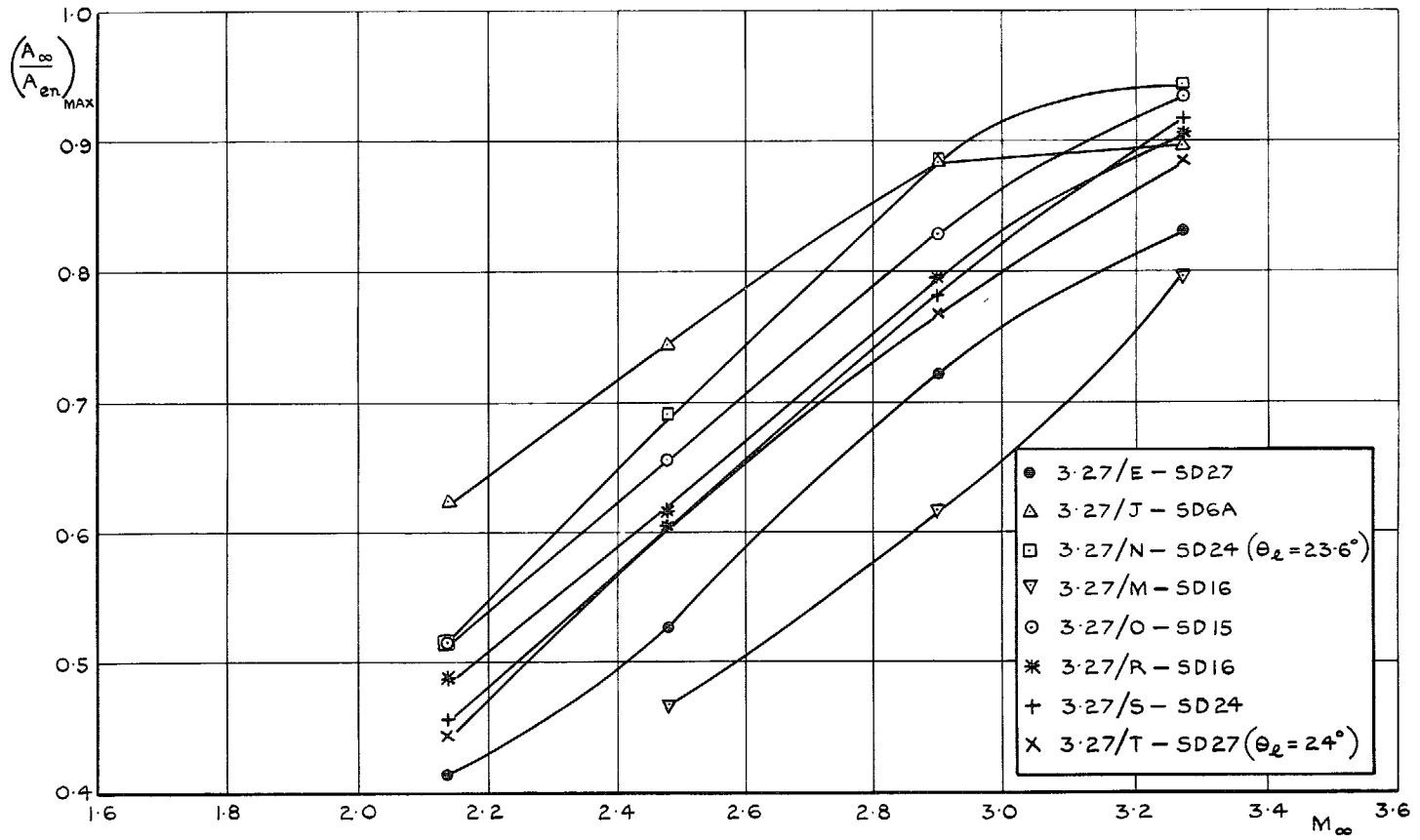

FIG. 34. Variation of maximum mass flow $(A_\infty/A_{en})_{max}$ with Mach number.

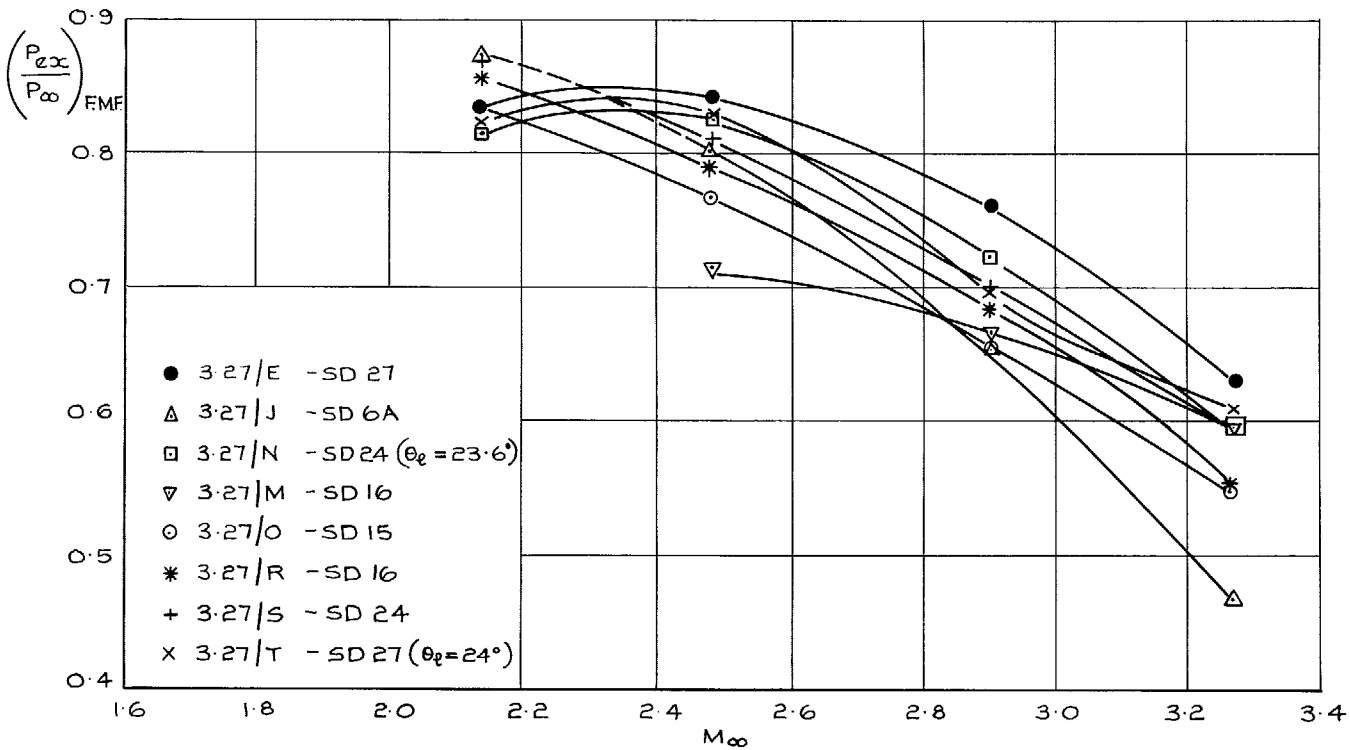

FIG. 35. Variation of pressure recovery at full mass flow $(P_{ex}/P_\infty)_{F.M.F.}$ with Mach number.

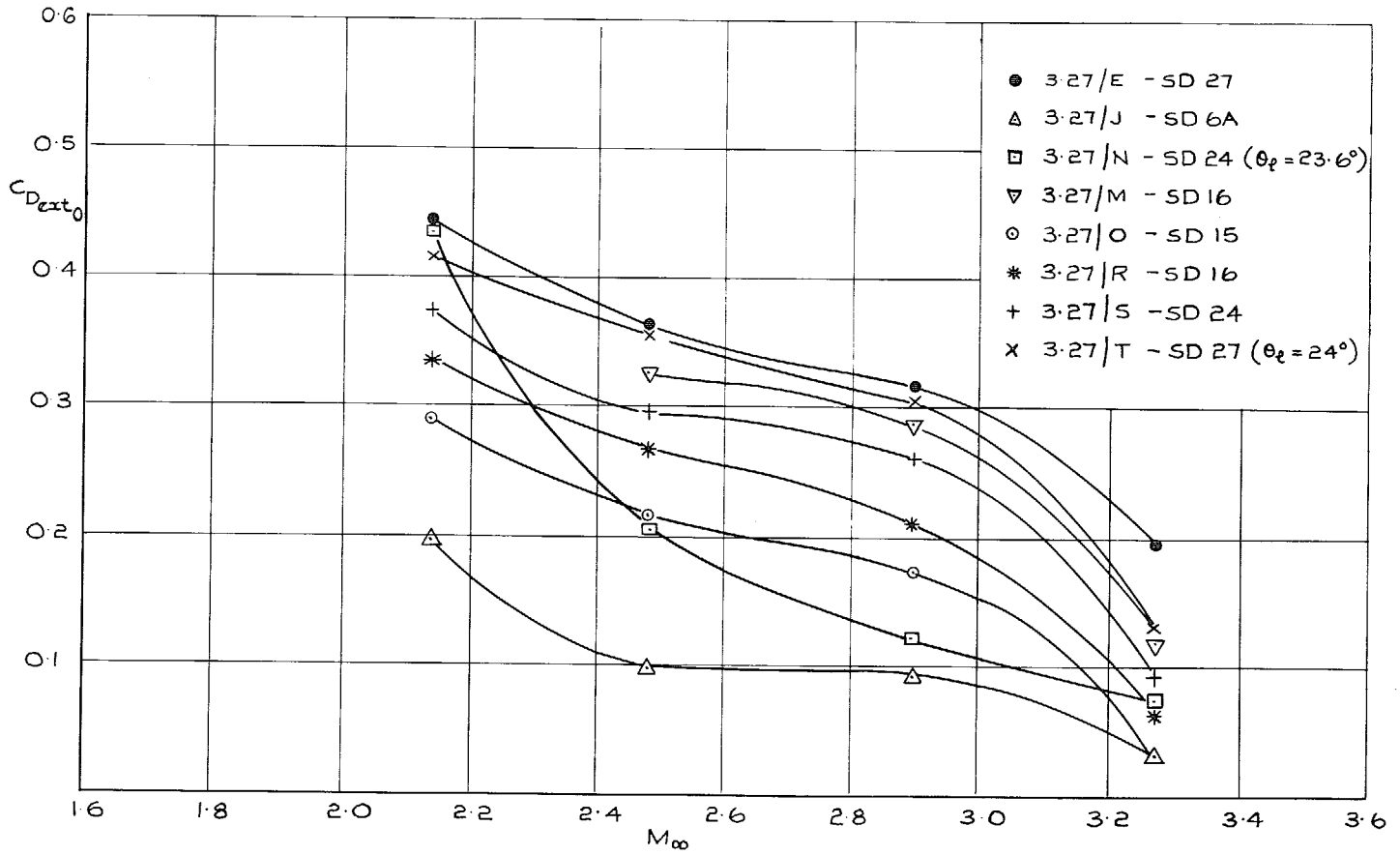

FIG. 36. Variation of external drag at full mass flow $C_{D_{ext_0}}$ with Mach number.

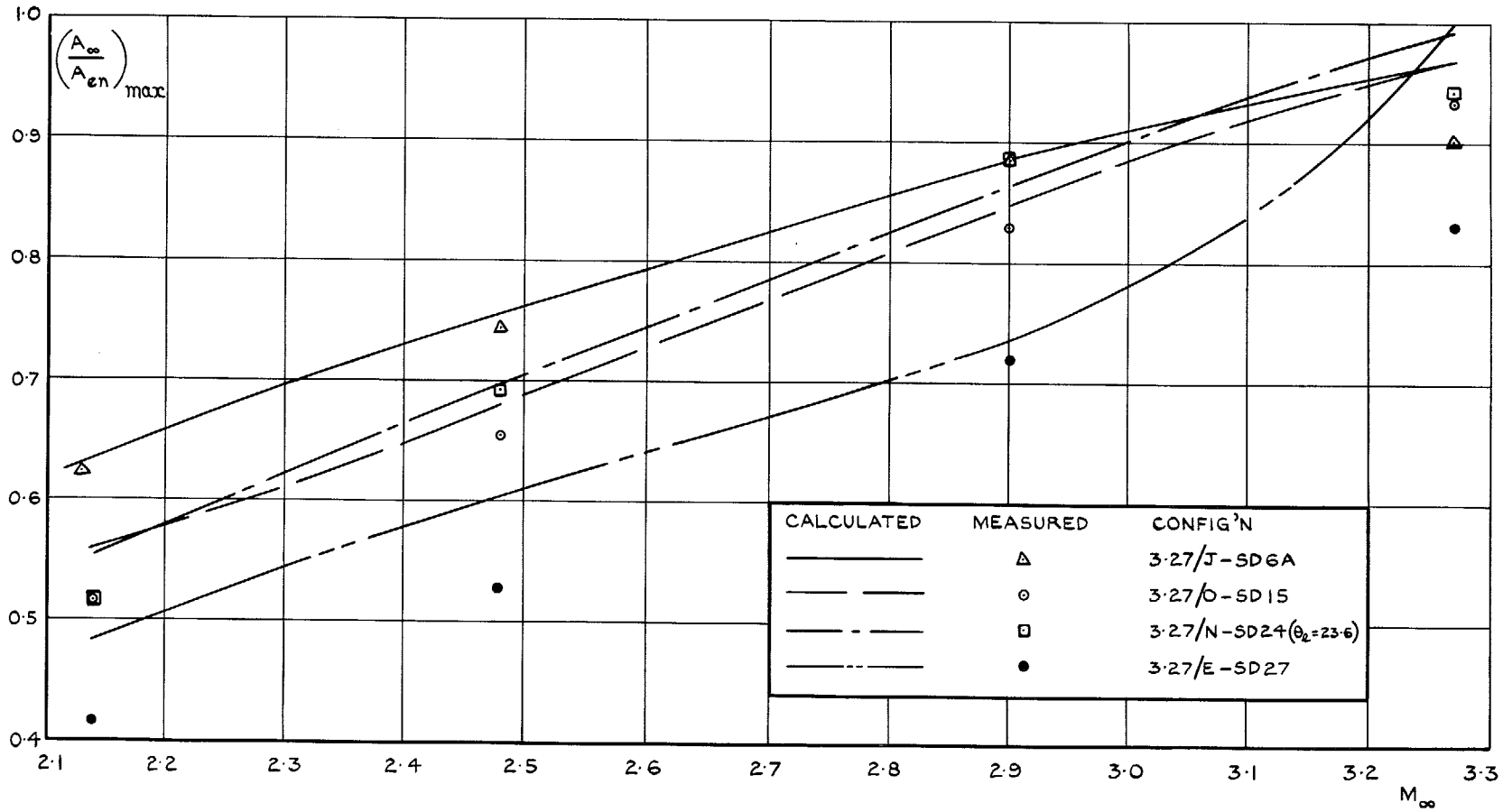

FIG. 37. Comparison of estimated and measured variation of $(A_\infty/A_{en})_{max}$ with M_∞.

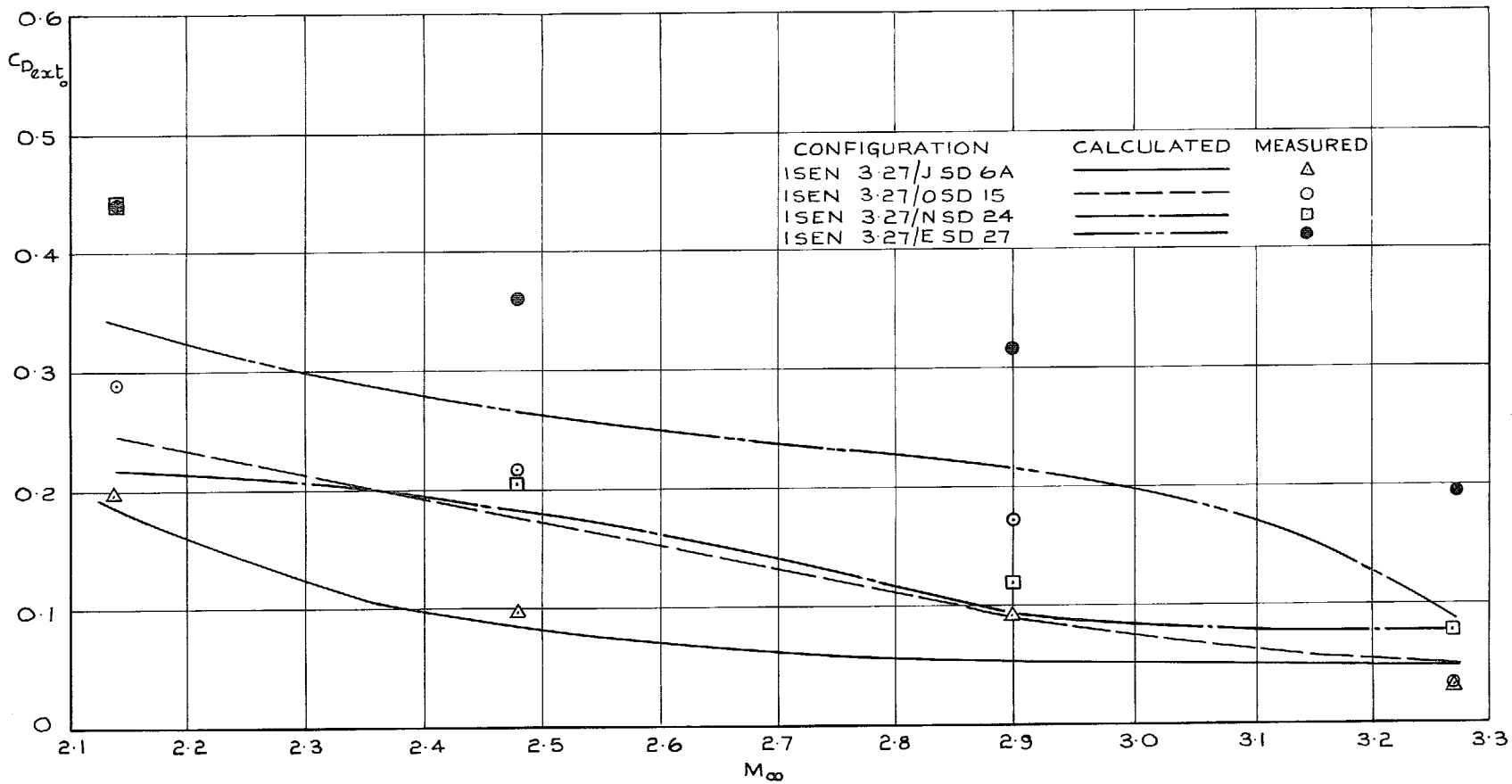

FIG. 38. Comparison of estimated and measured variation of drag at full mass flow $C_{D_{ext_0}}$ with M_∞.

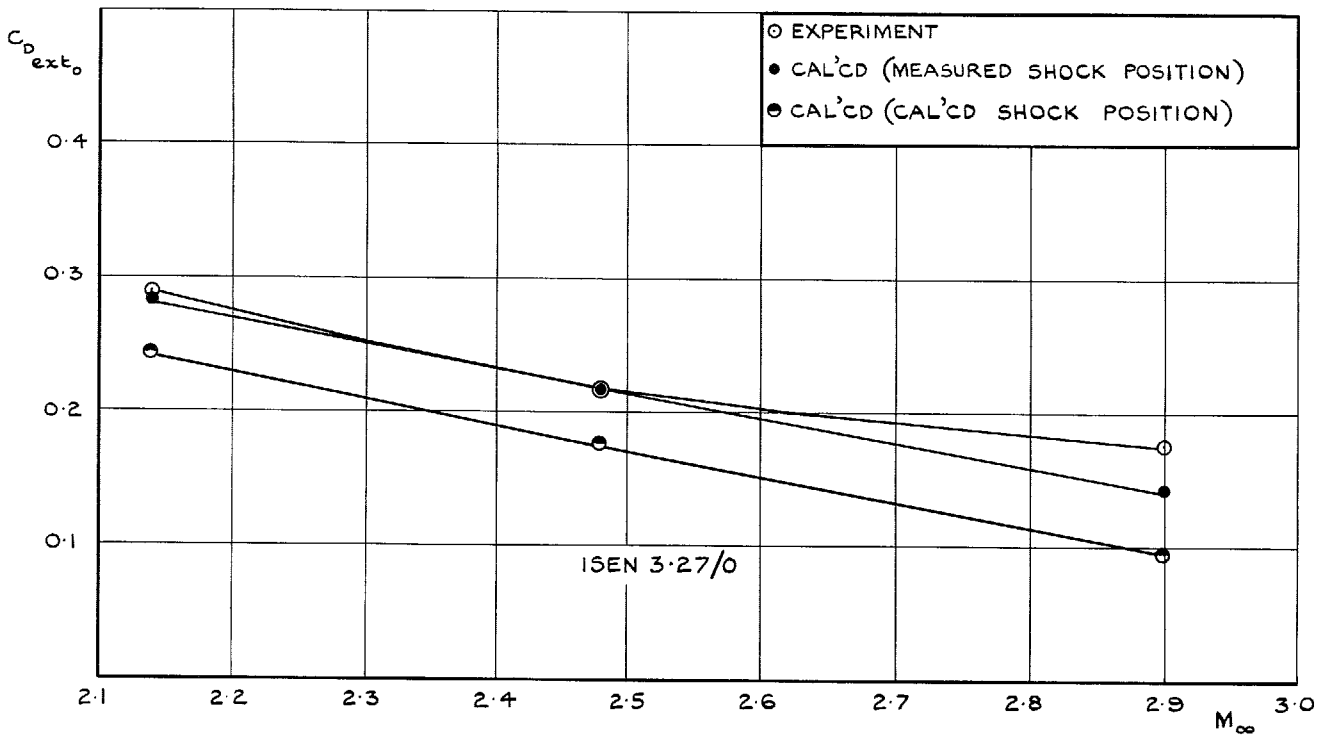

FIG. 39. Comparison of measured and calculated drag at full mass flow for Isen at 3·27/O.

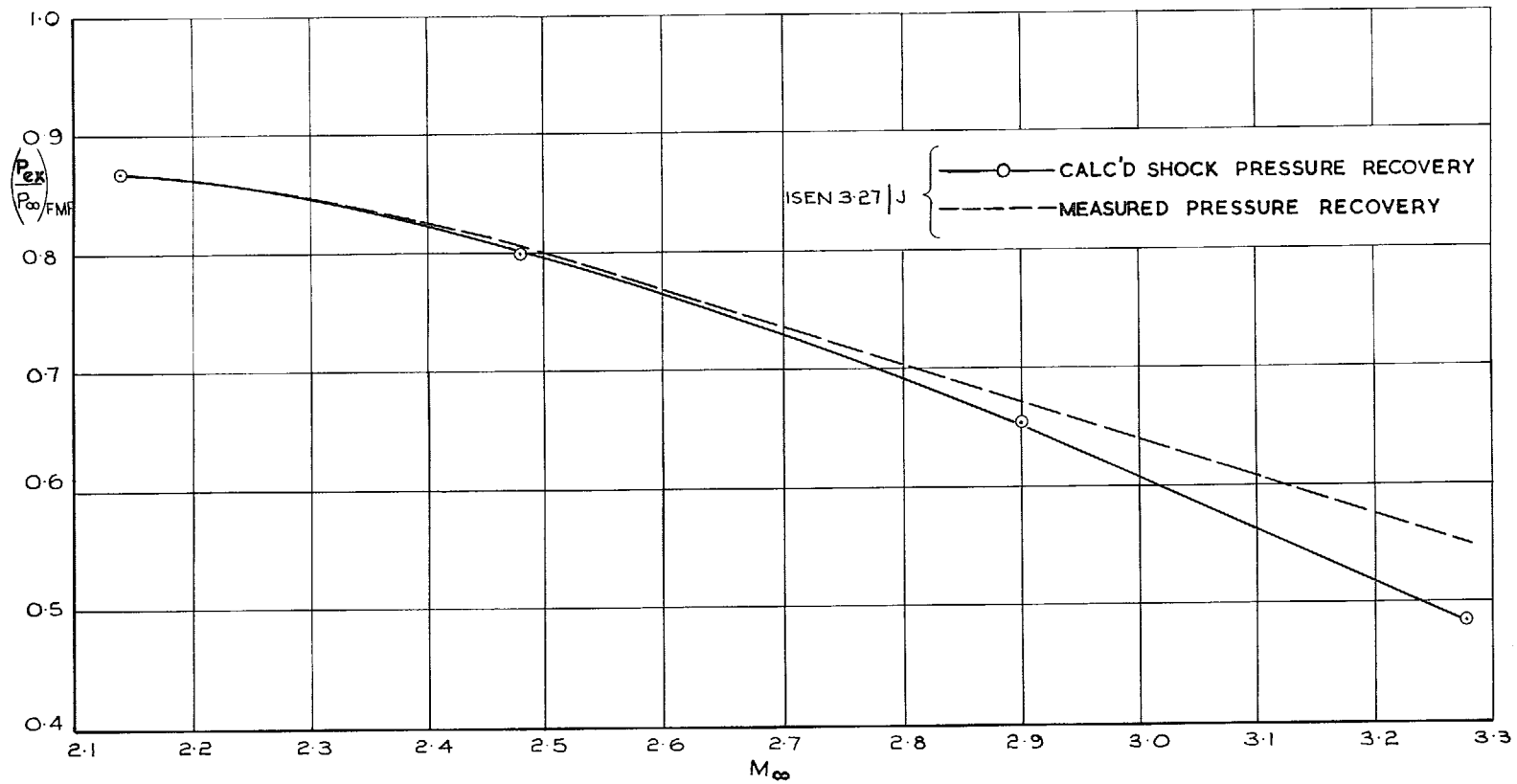

FIG. 40. Comparison of measured and calculated 'shock' pressure recovery for Isen 3·27/J.

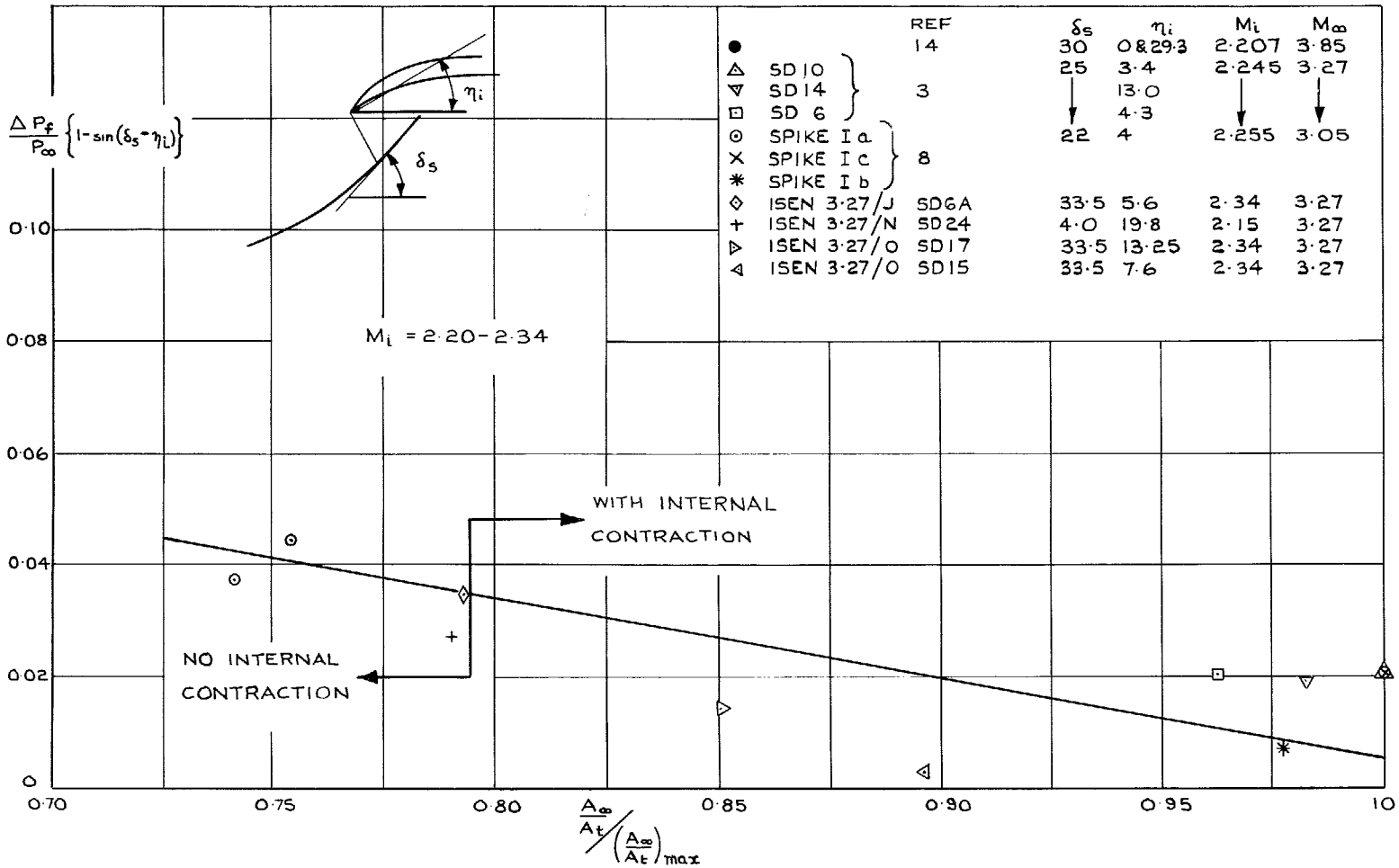

FIG. 41. Correlation of relative contraction ratio and residual loss.

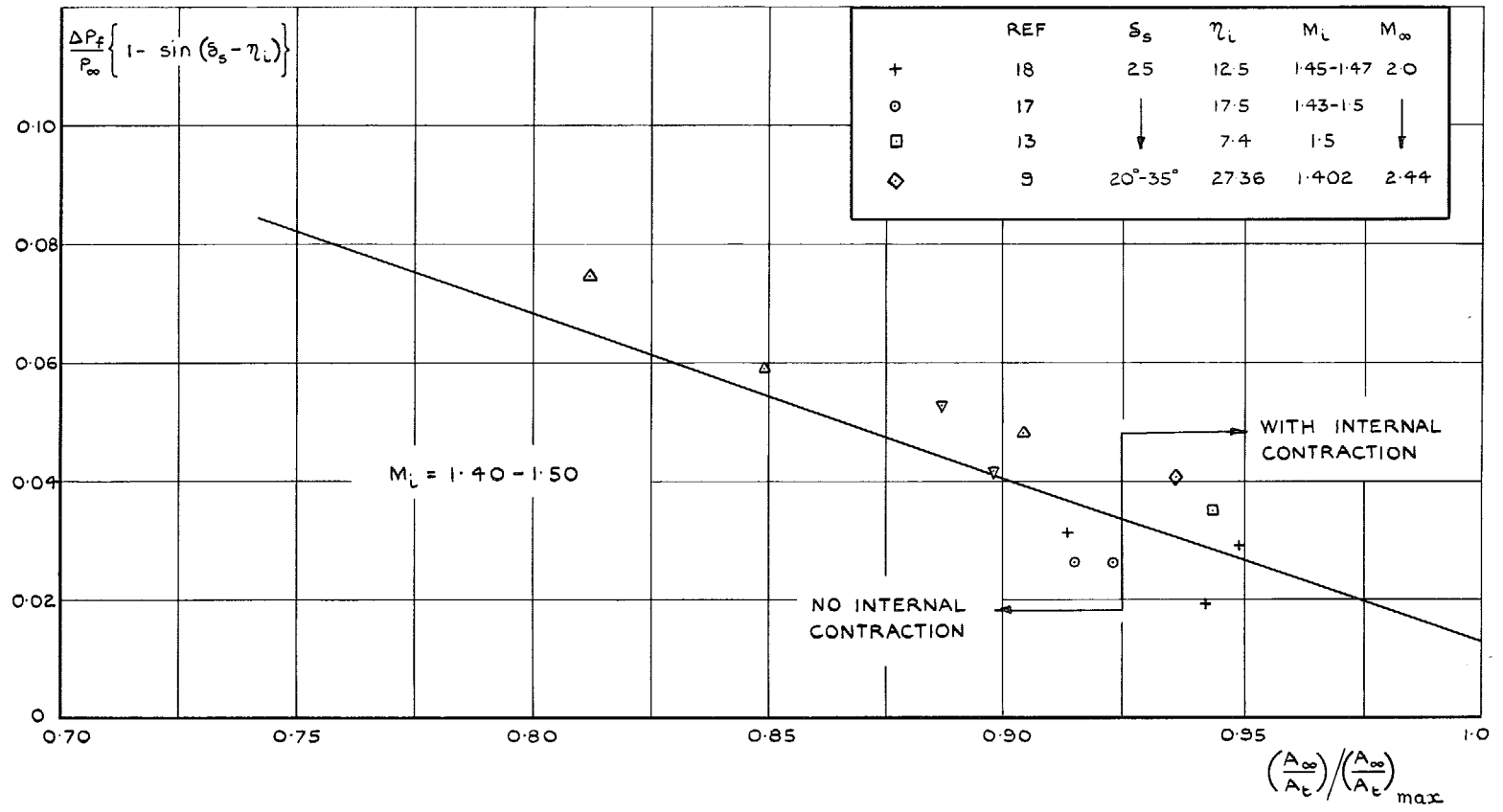

FIG. 42. Correlation of relative contraction ratio and residual loss.

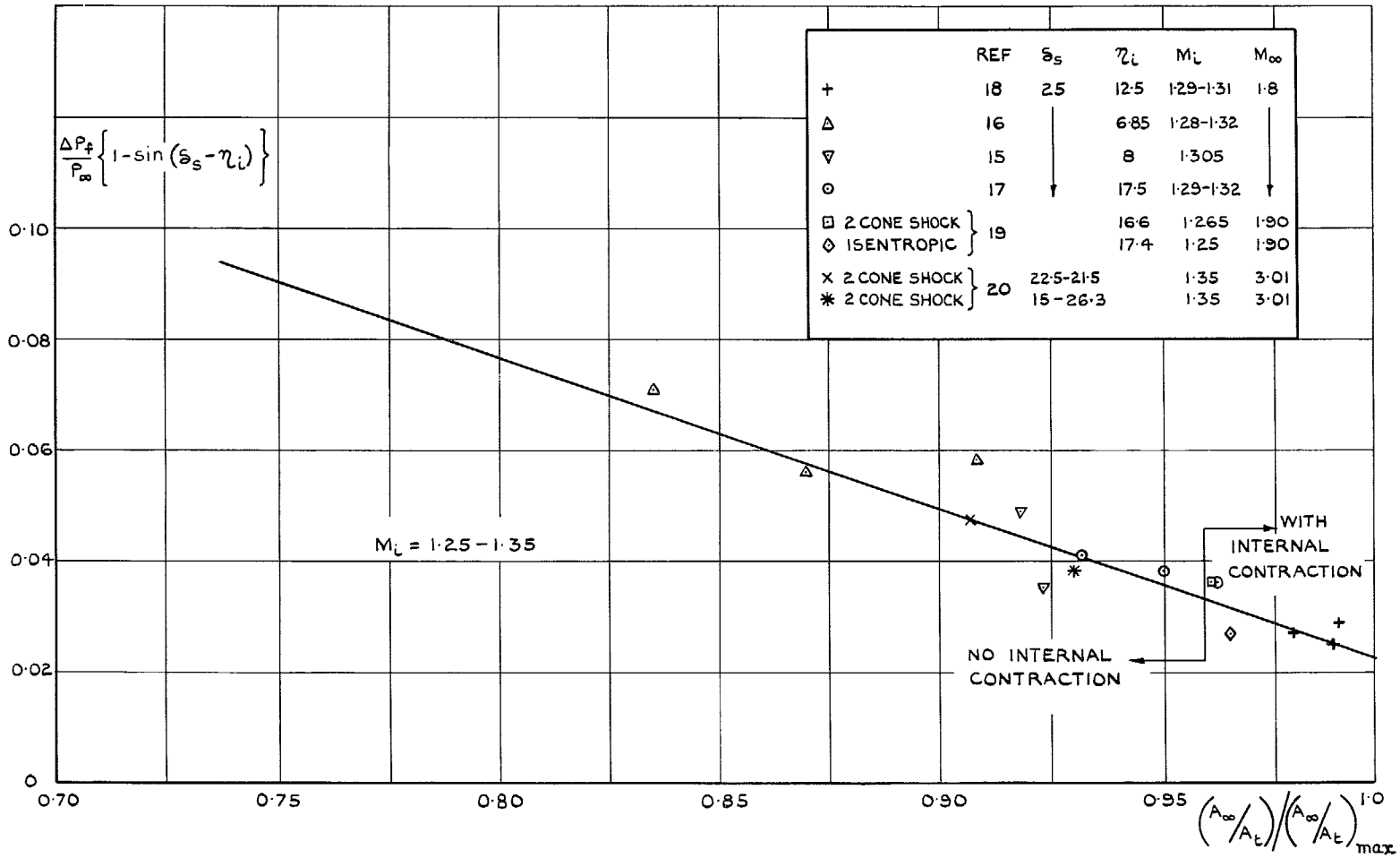

FIG. 43. Correlation of relative contraction ratio and residual loss.

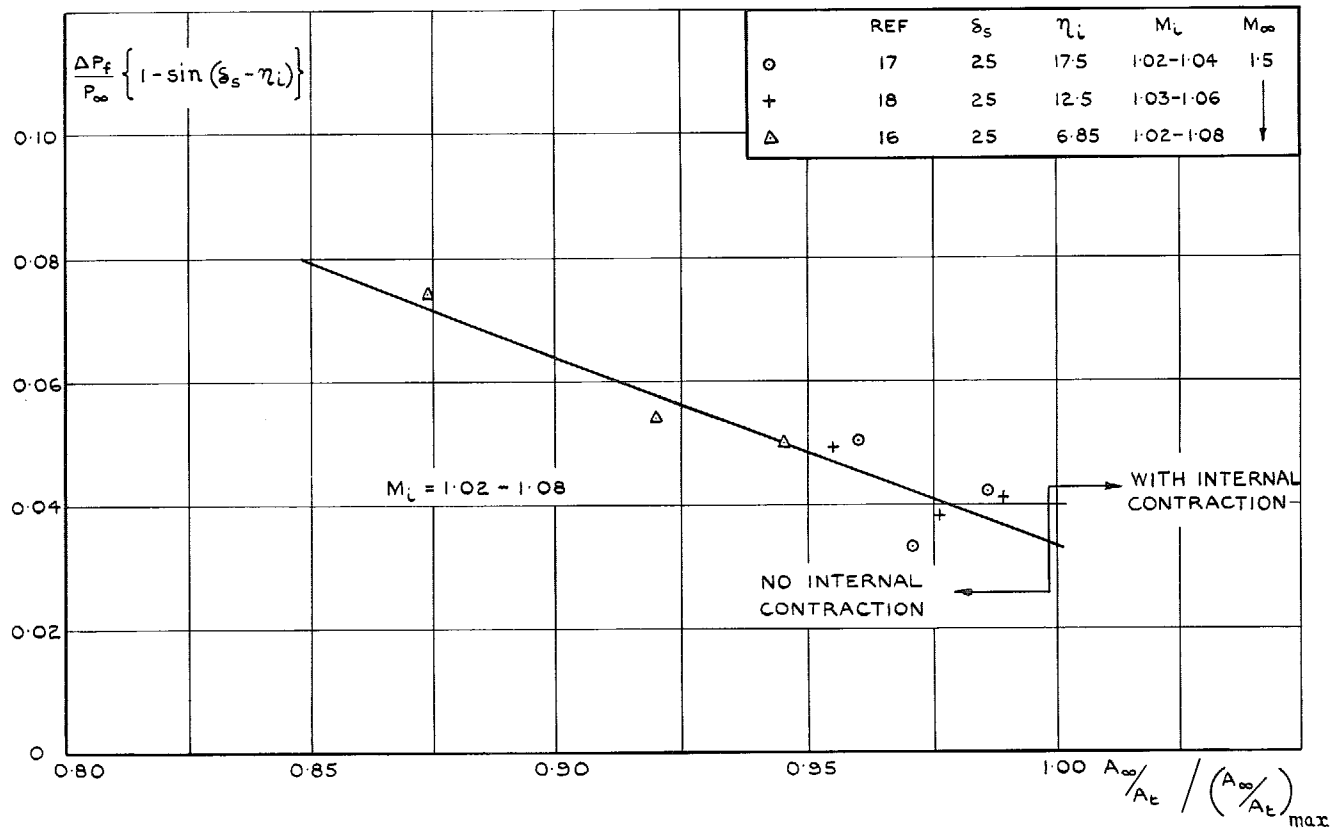

FIG. 44. Correlation of relative contraction ratio and residual loss.

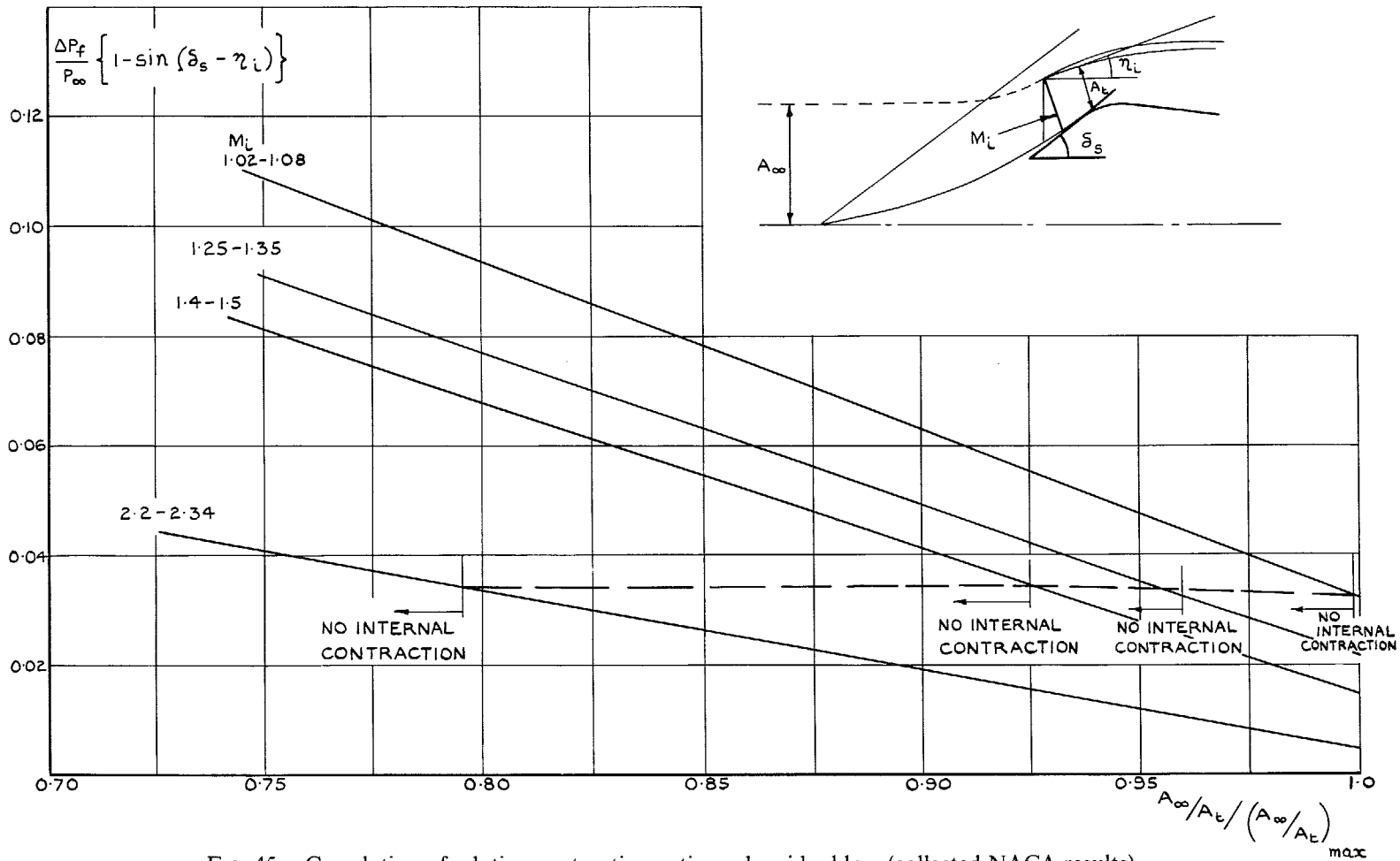

FIG. 45. Correlation of relative contraction ratio and residual loss (collected NACA results).

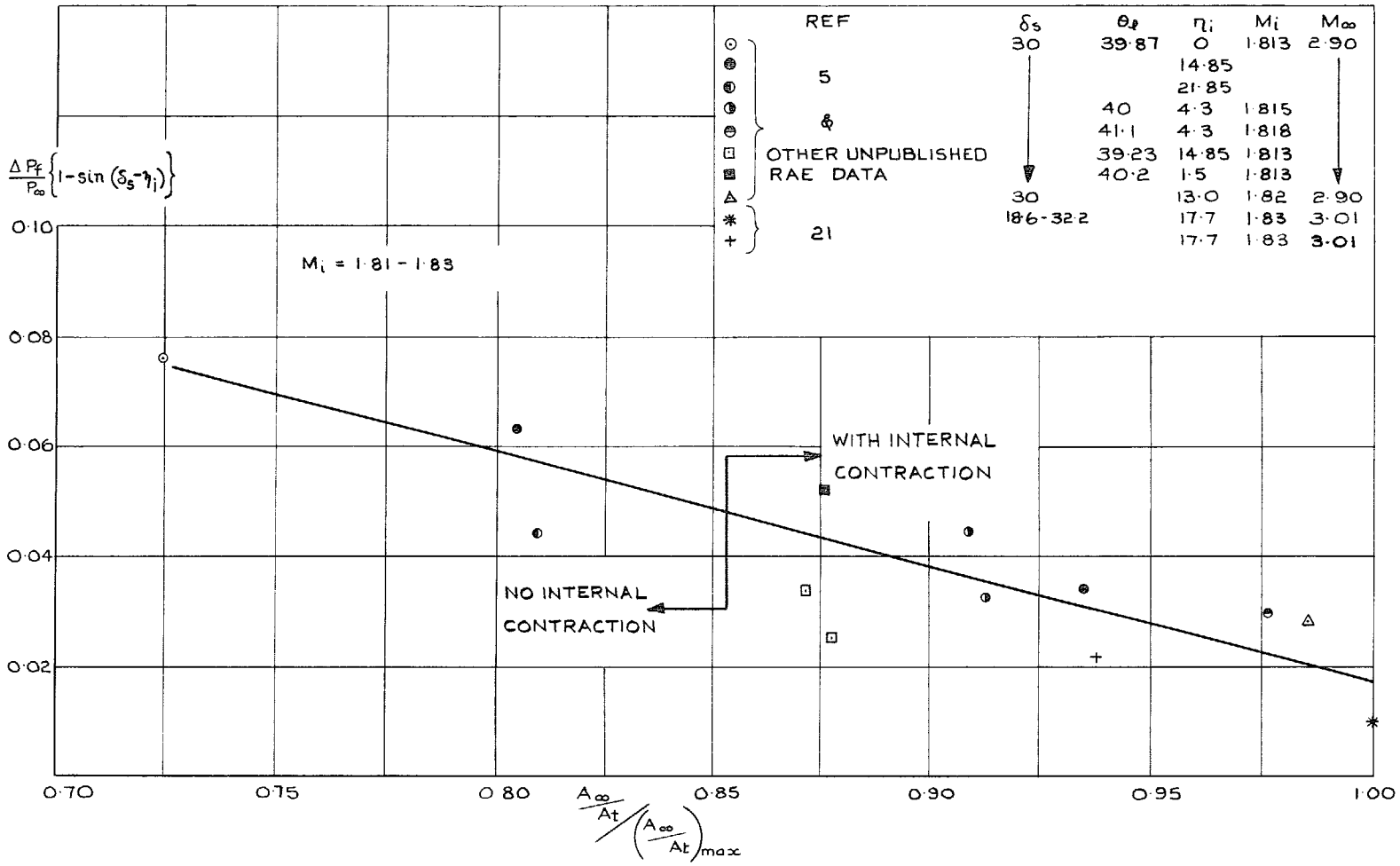

FIG. 46. Correlation of relative contraction ratio and residual loss.

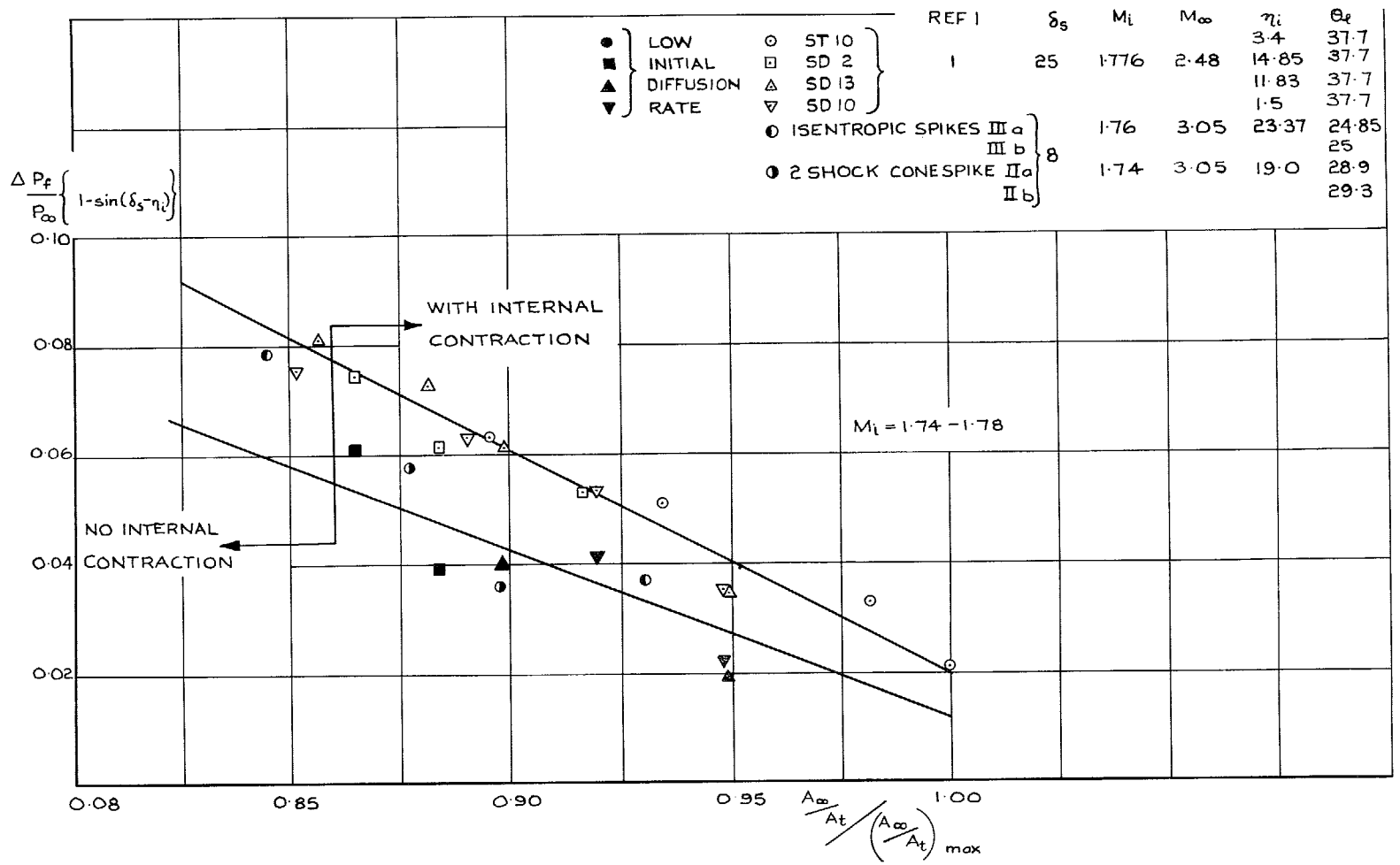

FIG. 47. Correlation of relative contraction ratio and residual loss.

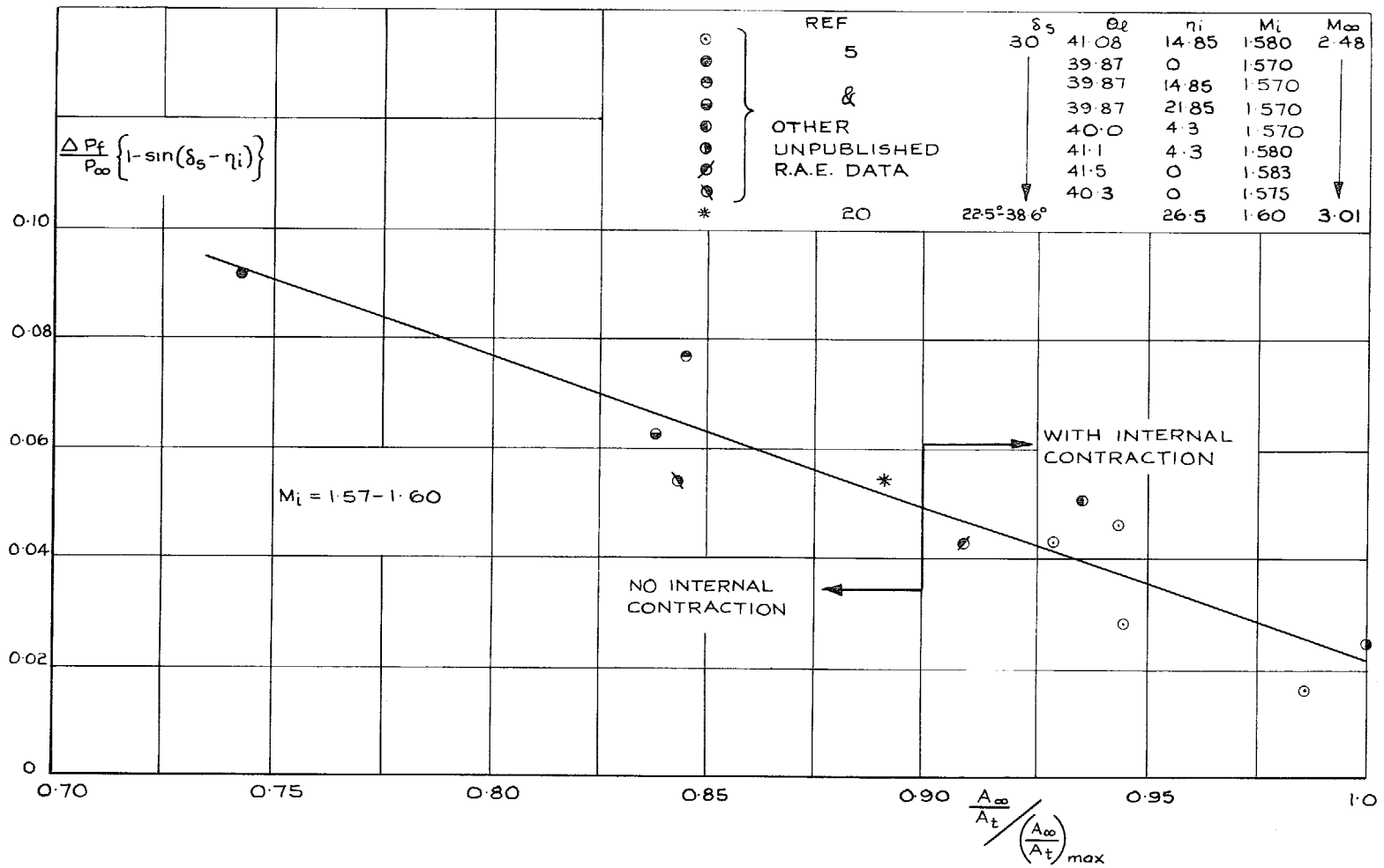

FIG. 48. Correlation of relative contraction ratio and residual loss.

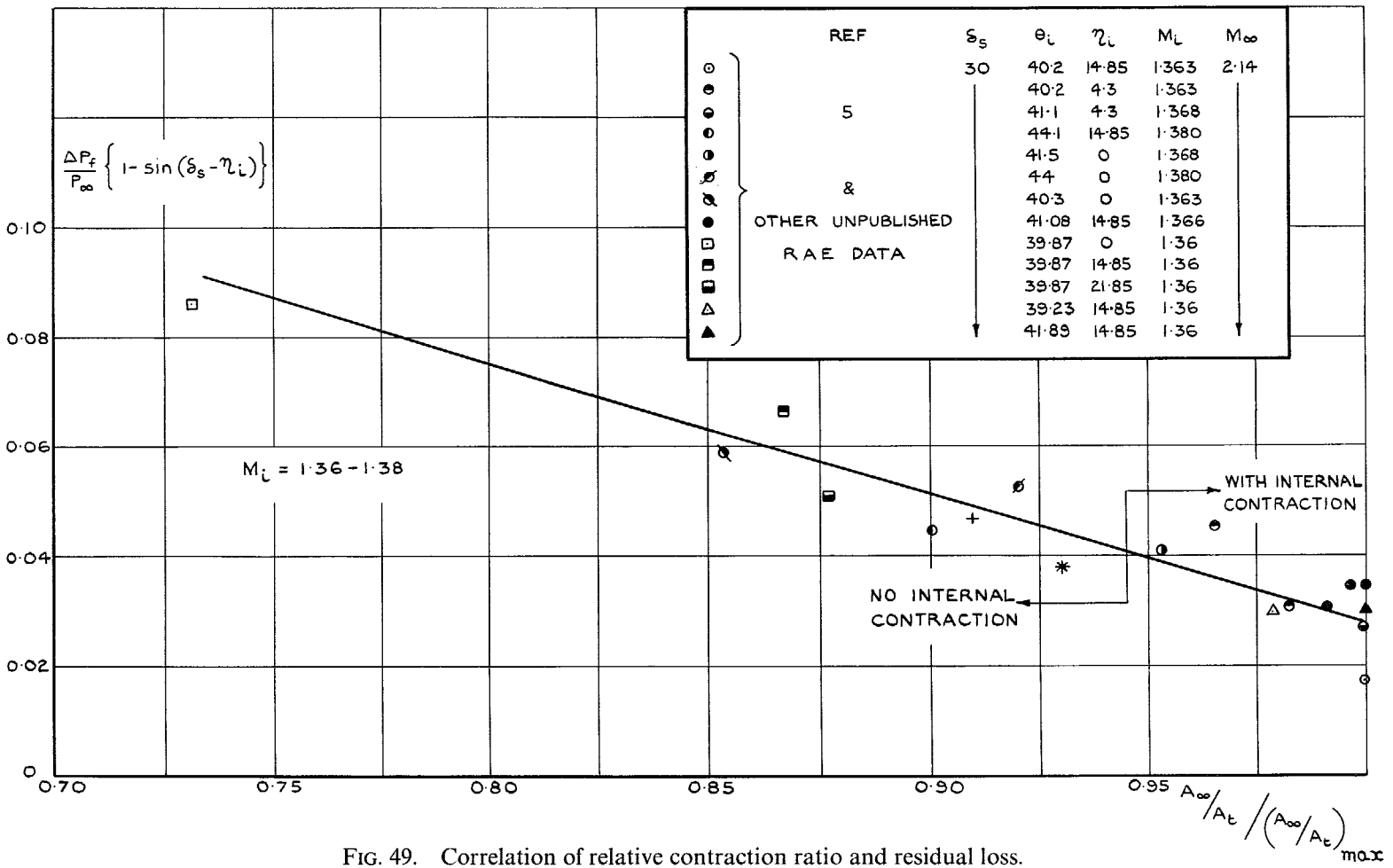

FIG. 49. Correlation of relative contraction ratio and residual loss.

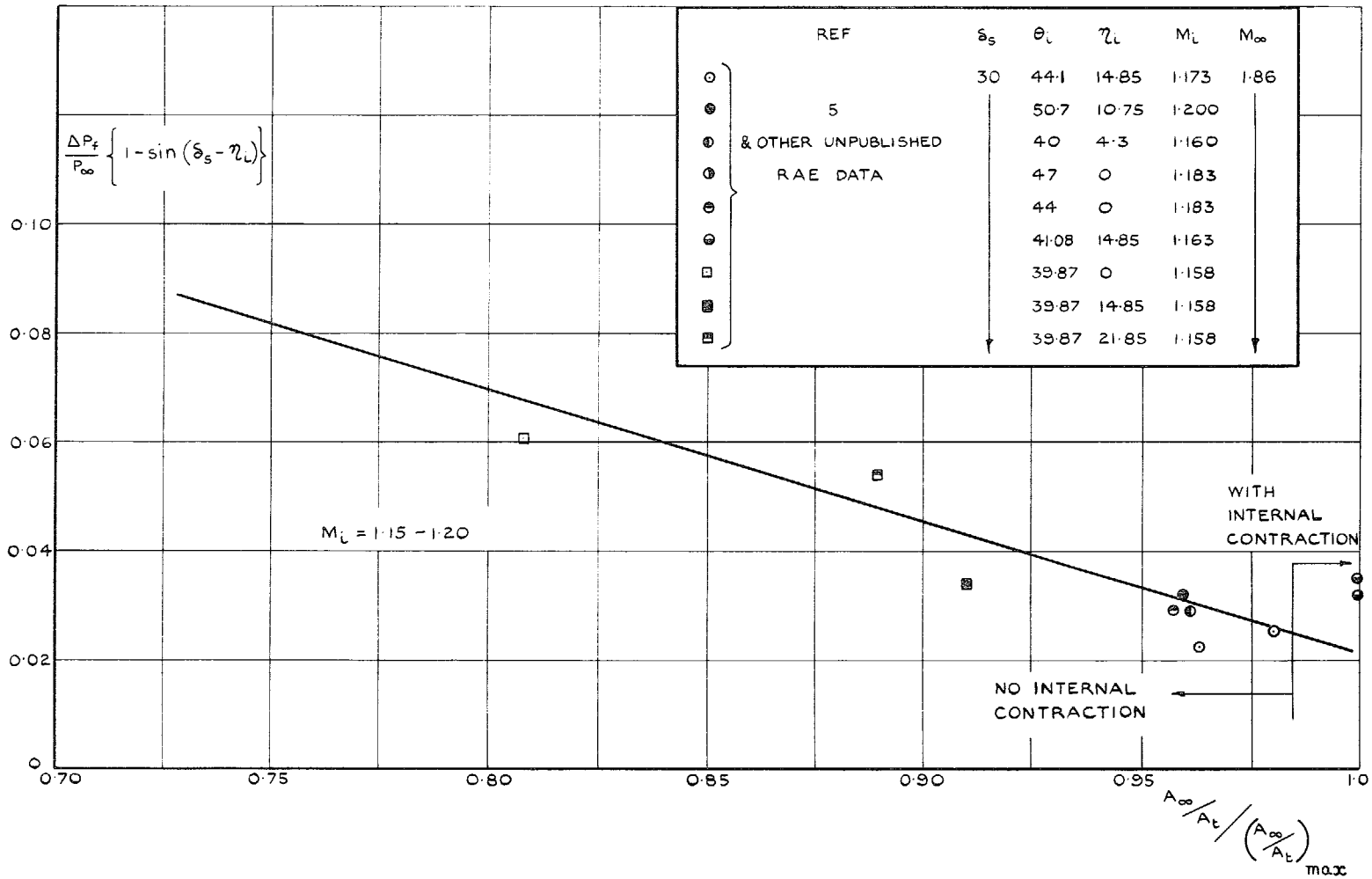

FIG. 50. Correlation of relative contraction ratio and residual loss.

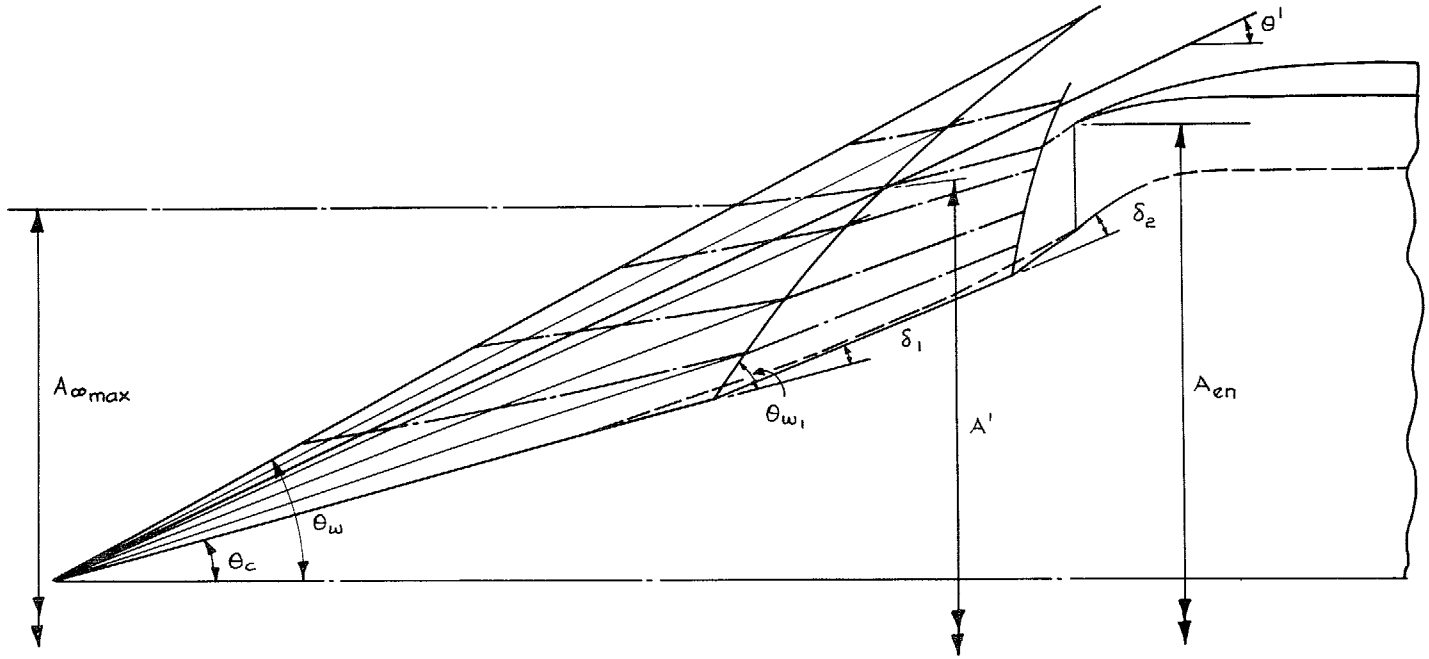

FIG. 51. Approximate construction for determination of $(A_\infty/A_{en})_{max}$.

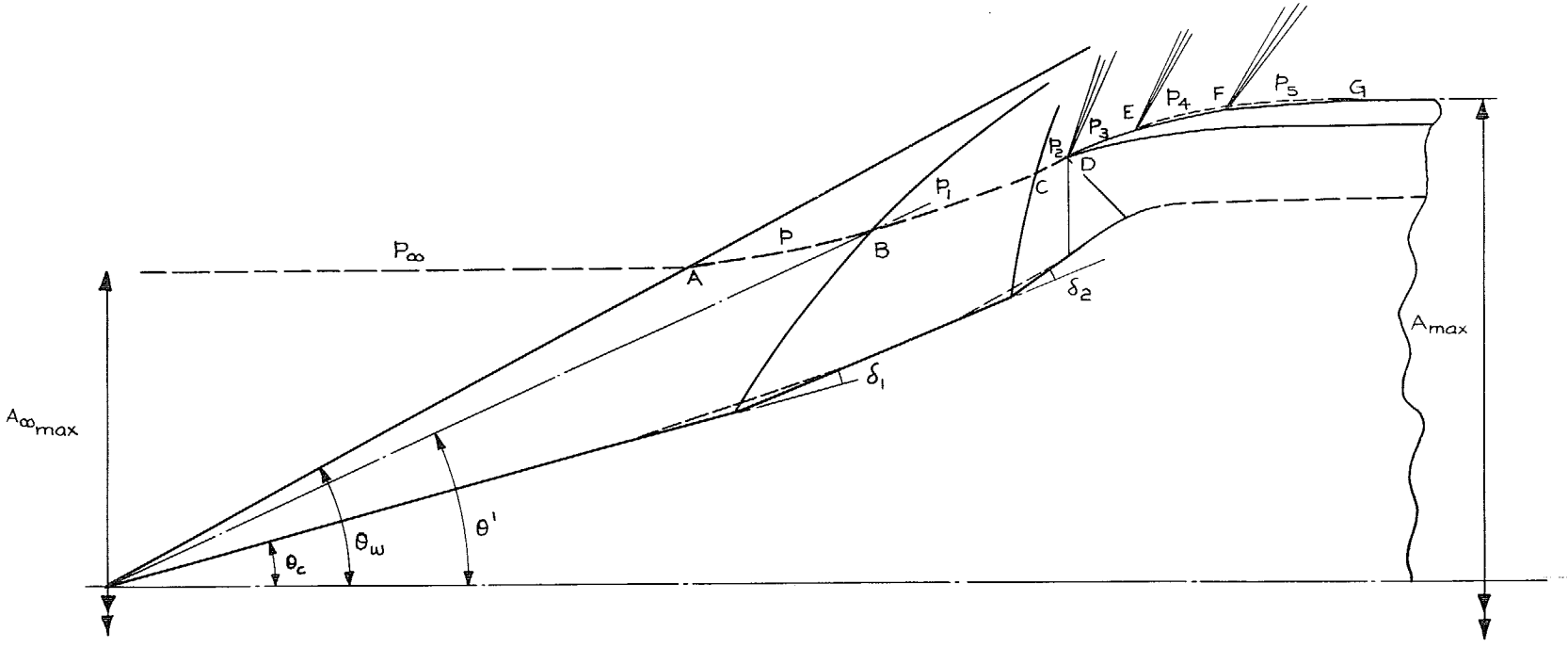

FIG. 52. Calculation $C_{D_{ext_0}}$ at below design Mach number (attached shock at cowl lip).

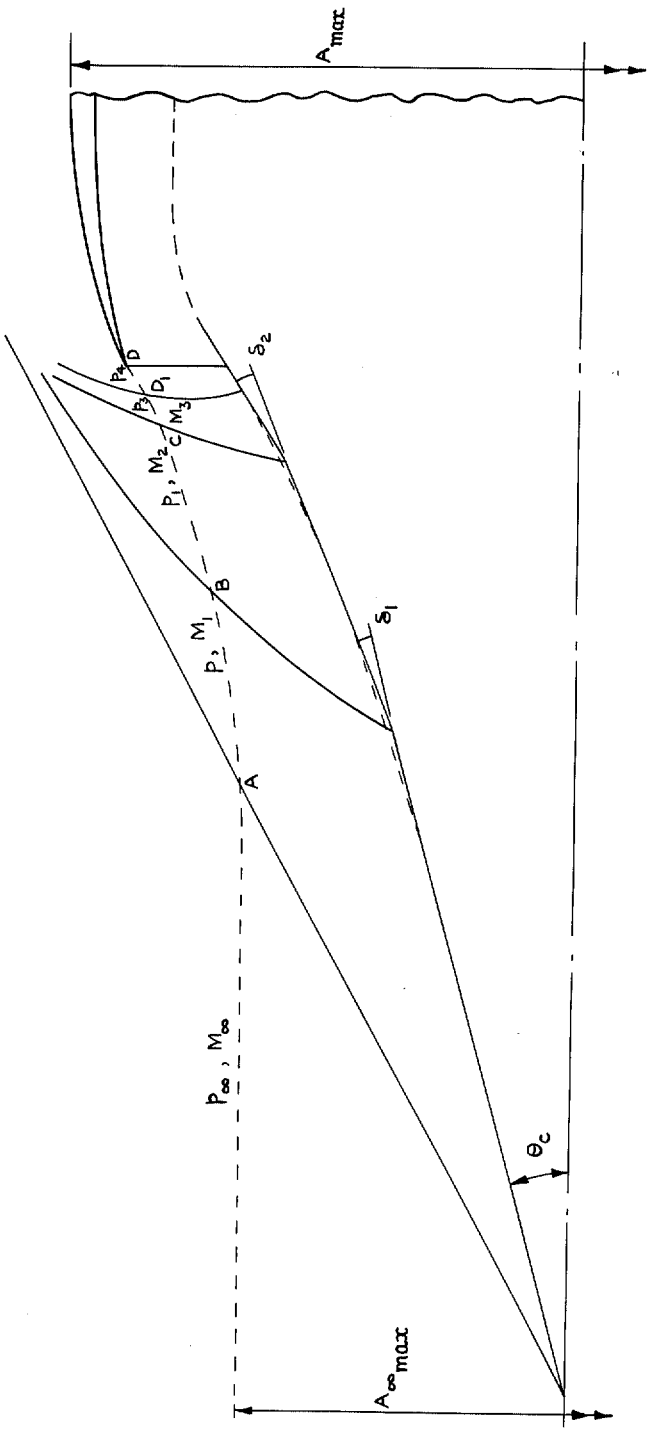

FIG. 53. Calculation of $C_{D_{ext_0}}$ at below design Mach number (detached shock at cowl lip).

Printed in England for Her Majesty's Stationery Office by J. W. Arrowsmith Ltd., Bristol 3

Dd. 135646 K.5

Published by
HER MAJESTY'S STATIONERY OFFICE

To be purchased from
49 High Holborn, London W.C.1
13A Castle Street, Edinburgh EH2 3AR
109 St. Mary Street, Cardiff CF1 1JW
Brazennose Street, Manchester M60 8AS
50 Fairfax Street, Bristol BS1 3DE
258 Broad Street, Birmingham 1
7 Linenhall Street, Belfast BT2 8AY
or through any bookseller

R. & M. No. 3585
SBN 11 470234 9